5-2016

Biophysical Studies of Cell Division Protein Localization Mechanisms in *Escherichia coli*

Matthew Wayne Bailey
University of Tennessee - Knoxville, mbaile25@vols.utk.edu

To the Graduate Council:

I am submitting herewith a dissertation written by Matthew Wayne Bailey entitled "Biophysical Studies of Cell Division Protein Localization Mechanisms in *Escherichia coli*." I have examined the final electronic copy of this dissertation for form and content and recommend that it be accepted in partial fulfillment of the requirements for the degree of Doctor of Philosophy, with a major in Physics.

Jaan Mannik, Major Professor

We have read this dissertation and recommend its acceptance:

Engin Serpersu, Soren Sorensen, Stuart Elston, Jaewook Joo

Accepted for the Council:
Dixie L. Thompson

Vice Provost and Dean of the Graduate School

(Original signatures are on file with official student records.)

Biophysical Studies of Cell Division Protein Localization Mechanisms in *Escherichia coli*

A Dissertation Presented for the

Doctor of Philosophy

Degree

The University of Tennessee, Knoxville

Matthew Wayne Bailey

May 2016

Dedication

It was freshman orientation at Berea College and all the academic departments were gathered to help incoming students identify their academic interests. While at the time my mathematical abilities were slim to none, ironically the first table I found myself standing next to was the Physics Department's. Behind that table stood an incredibly polite and welcoming professor, whom after talking to for only a short time had "encouraged" me to have a go at a degree in physics. That professor was Professor Amer Lahamer, and his table was the only table that I ended up visiting. My freshman year of physics didn't go so well. I worked with all my might, and still received a C in introductory physics. In time, Professor Lahamer showed me the underlying issue was that I didn't know how to learn. He always told his students to read the book no less than 3 times (cover to cover). He said to me, "Matthew, you should work to know your material so well that when you are tested on it, there is [to some extent] no thinking involved in solving the problem, just 'boom, boom, boom'". Now, for Dr. Lahamer's students, "No thinking" and "boom, boom, boom" are phrases we will never forget. What he meant was, you have to spend so much time with the material that you develop a sufficiently intimate understanding that upon seeing any question related to that material, the answer, in many respects, comes second nature. Professor Lahamer taught me that I didn't have to be a genius to learn and be successful in physics, I simply had to devote a great deal of time to practice it for many hours a day, every day. Subsequently, Professor Lahamer also taught me the critical life-lesson of how to make sacrifices. I gave up most of my extracurricular hobbies including the Bluegrass Band, and even most of my time with family and friends. The turning point for me happened about the time that Professor Lahamer, who seeing me near the point of total exhaustion, confided in me that he was man of faith. Professor Lahamer recognized the reason I was growing increasingly depressed originated from what seemed to me to be failure in school, which I had equated to meaning worthlessness in life. Though he deeply loved physics, I could tell the origins of his hope were

rooted in his faith. He encouraged me not to place my perceived value in how well I appeared to be doing in class, but rather to be rooted in my own faith, and always to maintain that vision. From then on, I saw Professor Lahamer in a different light. He had become much closer than a professor. Not only was he teaching me the necessary academic concepts, but more importantly, he was developing my growth and maturity as a person. It is because of Professor Lahamer that I have pursued my PhD. It goes without saying that my dissertation is dedicated to the amazing man who has had such a profound influence on my life. My story is only of one of a great many, though. I'd like to leave with something Professor Lahamer always told me, "The list of things you don't know when you are born is infinite, and the list of things you don't know when you die still will be infinite". The point is, live humbly and with thankfulness.

Acknowledgements

I would like to express my deepest gratitude to my PhD advisor Professor Jaan Mannik who has taken an invaluable portion of his time over the past four years to guide and train me to become an independent researcher. Moreover, I would like to thank Professor Mannik for teaching me to synthesize a large body of scientific literature into a coherent and cogent form, from which I can properly contextualize my research contributions.

I would like to thank my committee members: Dr. Engin Serpersu, Dr. Soren Sorensen, Dr. Stuart Elston, and Dr. Jaewook Joo for their instrumental criticisms and advice, which have increased not only my scientific expertise and communication but also have helped me to view my scientific questions and results from cross-disciplinary vantage points.

I would also like to thank the many colleagues and friends I've developed throughout my research for creating a supportive and encouraging working environment especially during times of elevated stress. Our relationship has enabled me to think more rationally, and has helped me to maintain a proper perspective of my life, and the proper place my work occupies. In particular, I'd like to thank one of my very best friends and brother Clayton Greer, another amazing man Will Deaderick, the always intriguing Boyd Warren, my Casual Pint comrade Ryan Hefti, the man of a million talents Da Yang, my dear friend and perspectives safeguard Anne Jennings, and yet another dear friend and comic relief advocate Bryant Walker.

I would like to thank my beautiful wife Madē McCormick who tolerated my late nights getting home, made sacrifices on her behalf to provide and take care of me, who listened to my daily frustrations with experiments gone awry, fears, and worries, and who has supported me emotionally and psychologically throughout.

Lastly, I would like to thank my parents from whom I have been separated for most of the past 10 years to pursue my education, and for whom I owe my character, my integrity, and my understanding of human caring and compassion for others. I have missed them.

Abstract

How nanometer-scale proteins position accurately within micron-scale bacteria has intrigued both biologists and physicists alike. A critical process requiring precise protein localization is cell division. In most bacteria, cell division starts with the self-assembly of the FtsZ proteins into filaments that form a ring-like structure encircling the cell at its middle, the Z-ring. The Z-ring is a scaffold for additional proteins that synthesize the lateral cell wall which separates the two daughter cells. If division planes are misplaced relative to bacterial chromosomes, also called nucleoids, daughter cells with incomplete genetic material can be produced. In *Escherichia coli*, research carried out over the past several decades has determined two independent molecular mechanisms that are involved in the midcell placement of the division plane, the Min system, and the SlmA proteins. By combining quantitative image analysis, fluorescence microscopy, and molecular biology techniques, this work provides evidence for two additional mechanisms that coordinate Z-ring positioning with chromosome segregation in *E. coli*. The first mechanism revealed itself in cells that had the Min system and the SlmA proteins removed. In these cells, the Z-ring invariably localized at the center of the nucleoid. Formation of Z-ring in this location depended on cell cycle dependent movement of the replication terminus region (Ter) to nucleoid middle, and on ZapA, ZapB, and MatP proteins. The second mechanism was revealed in cells where Z-rings were strongly misplaced relative to chromosomes. Interestingly, most of these cells were still viable. We determined that cells retained their viability because as much as 1/3 of the chromosome moved across the closing division plane in the late stages of cytokinesis. Chromosome repositioning appears to rely on septal cell wall synthesis rather than on DNA translocase activity. Altogether this work demonstrates that *E. coli* harbors several partially redundant molecular systems, in addition to those known previously, that collectively guarantee accurate and robust placement of both cell division proteins and chromosomes.

Table of Contents

List of Tables

List of Figures

List of Abbreviations

abcD	Refers to a hypothetical gene *abcD*
AbcD	Refers to the gene product (or protein)
Δ*abcD*	Indicates gene *abcD* has been deleted
Δ*abcD*::*efgH*	Gene *abcD* has been replaced with gene *efgH*
pAB01	Refers to a hypothetical plasmid AB01
aa	Amino acid
FFP	Fluorescent fusion protein
GFP	Green fluorescent protein
mCherry	A type of Red fluorescent protein
DAPI	4',6-diamidino-2-phenylindole
IPTG	Isopropyl β-D-1-thiogalactopyranoside
kan	Kanamycin (antibiotic)
amp	Ampicillin (antibiotic)
cm	Chloramphenicol (antibiotic)
LB	Lysogeny broth (nutrient rich bacterial growth medium)
M9	Salt blend for nutrient poor bacterial growth medium
Ter	Replication terminus region of the chromosome
NO	Nucleoid occlusion
VENO	Volume exclusion [based] nucleoid occlusion
QD	Quantum dot
PSF	Point spread function
CCD	Charge-coupled device (camera)

Introduction

In the history of the Earth, perhaps one of the most astounding events was the emergence of the first cellular life, which is likely to have most closely resembled modern bacteria. It is estimated that about 700 million years following the formation of the earth the first prokaryotic life appeared (Mojzsis, Arrhenius et al. 1997). From then on, bacteria have played diverse, vital roles in the evolution and proliferation of all subsequent forms of life, which can be demonstrated in four ways: (1) bacterial biodiversity, (2) biogeochemistry, (3) evolutionary history, and (4) bacterial symbiosis (O'Malley 2014).

Today, there are an estimated 5×10^{30} prokaryote cells on the planet (Whitman, Coleman et al. 1998). To put this number into perspective, there are approximately 10^{16} bacteria in a pick-up truck-load of soil, which is ten thousand times greater than the number of stars in the Milky Way galaxy (Curtis and Sloan 2005). Accordingly, the total biomass of bacteria is at least equal with the biomass of all plants (Singleton 2004). More important than their sheer number however, the global chemistry of life is based on and regulated by bacterial metabolisms interacting with the Earth's geochemistry (Falkowski, Fenchel et al. 2008). These biogeochemical cycles are themselves the products of evolution over the entire history of the Earth, in which microbes have not only themselves evolved but have had major evolutionary impacts on every other evolving lifeform. Not surprisingly, this impact is largely derived from the symbiosis between bacteria and other forms of life. As an example, it is estimated that there are 10 times more bacterial cells on and within our bodies than there are human cells. Some of these bacteria are critical for our survival (Berg 1996). Because bacteria play an integral role in the processes of life on Earth, it is crucial that we understand how they function, namely, how they grow and divide. Accordingly, in this work we investigate two primary questions, 1. what physical and molecular mechanisms do modern bacteria use to influence the positioning of the proteins required for cell division, and 2.

how is cell division coordinated with other events in the cell cycle such as DNA replication and segregation.

Cell division in early cells

In modern cells, growth and division require the proper proteins to be localized at the right place within the cell at the right time. Consequently, modern cells have evolved multiple molecular systems to regulate the spatial and temporal positioning of the proteins involved in cell division to prevent formation of DNA-less cells and cells with damaged DNA. Interestingly, even when these highly evolved division protein positioning systems are removed from modern bacteria, they remain viable (Bernhardt and de Boer 2005, Rodrigues and Harry 2012, Bailey, Bissichia et al. 2014). This finding could suggest that primordial division mechanisms remain operational even in modern cells. Unlike modern bacteria, early primitive cells (or *proto-cells*) likely were much less complex, consisting of only an amphiphilic membrane enclosure harboring self-replicating genetic material (Chen and Walde 2010, Schrum, Zhu et al. 2010). How these early proto-cells grew and divided remains unclear, though it is believed the process could be described predominantly by physical and chemical principles, such as the self-organizing properties of intracellular components and on interactions with their environment (Hanczyc and Szostak 2004). If so, perhaps the current biochemistry based description of cell division in modern bacteria should be expanded to include the underlying contributions of physics. In this work, we study a strain of the modern bacterium *E. coli* which was found to proliferate in the absence of all known molecular cell division protein regulation systems. We propose a positioning system that does not rely on an evolved molecular system but one that utilizes physical interactions between division proteins and DNA to not only regulate spatial positioning but also coordinate cell division with other critical events in the cell cycle, such as DNA replication and segregation.

In the remainder of Chapter 1, I describe the current understanding of cell division in modern, wild-type *E. coli* and thereafter present a physical model that can account for the

positioning of cell division proteins that the organism could have inherited from its ancient ancestors.

Cell division in the model bacterium *Escherichia coli*

Historically, biological research has focused on a small fraction of the Earth's biodiversity to understand the general principles governing life; accordingly, these select organism are referred to as "model organisms" (Hedges 2002). Much of the current understanding about genetics, proteomics, development, and evolution results from studies of one of the most studied bacterial model organisms, *Escherichia coli* (Lee and Lee 2003). Because of wealth of knowledge obtained already for *E. coli*, the relative ease with which E. coli can be cultured and genetically modified, and because bacteria are among the simplest living systems to study, we have chosen *E. coli* as a platform upon which we aim to build a more quantitative, physical understanding of cell division.

Many of the proteins required for cell division have been identified only in the past couple decades (Singleton 2004). In most bacteria, the main macromolecular structure that is responsible for coordinating cell division with other cellular processes, including replication and segregation of chromosomes, is the Z-ring (Bi and Lutkenhaus 1991, Margolin 2005, Adams and Errington 2009, de Boer 2010, Erickson, Anderson et al. 2010, Lutkenhaus, Pichoff et al. 2012). Z-ring formation is the first step in bacterial cytokinesis (cytokinesis, see Appendix Glossary) (Figure 1). The Z-ring is organized by linear FtsZ filaments that in *E. coli* are anchored to the cell plasma membrane by FtsA and ZipA linker proteins (Chen, Bjornson et al. 2005, Loose and Mitchison 2014). Once the Z-ring has formed from the bundling of these FtsZ filaments into a loose ring-like annulus around the middle of the cell, the Z-ring becomes a scaffold for over 30 subsequent proteins that forms a macromolecular complex called the divisome (Liu, Persons et al. 2015). The divisome carries out septal (septum, see Appendix Glossary) cell wall synthesis that leads to the pinching off of one daughter cell from the other (binary fission) (Figure 1).

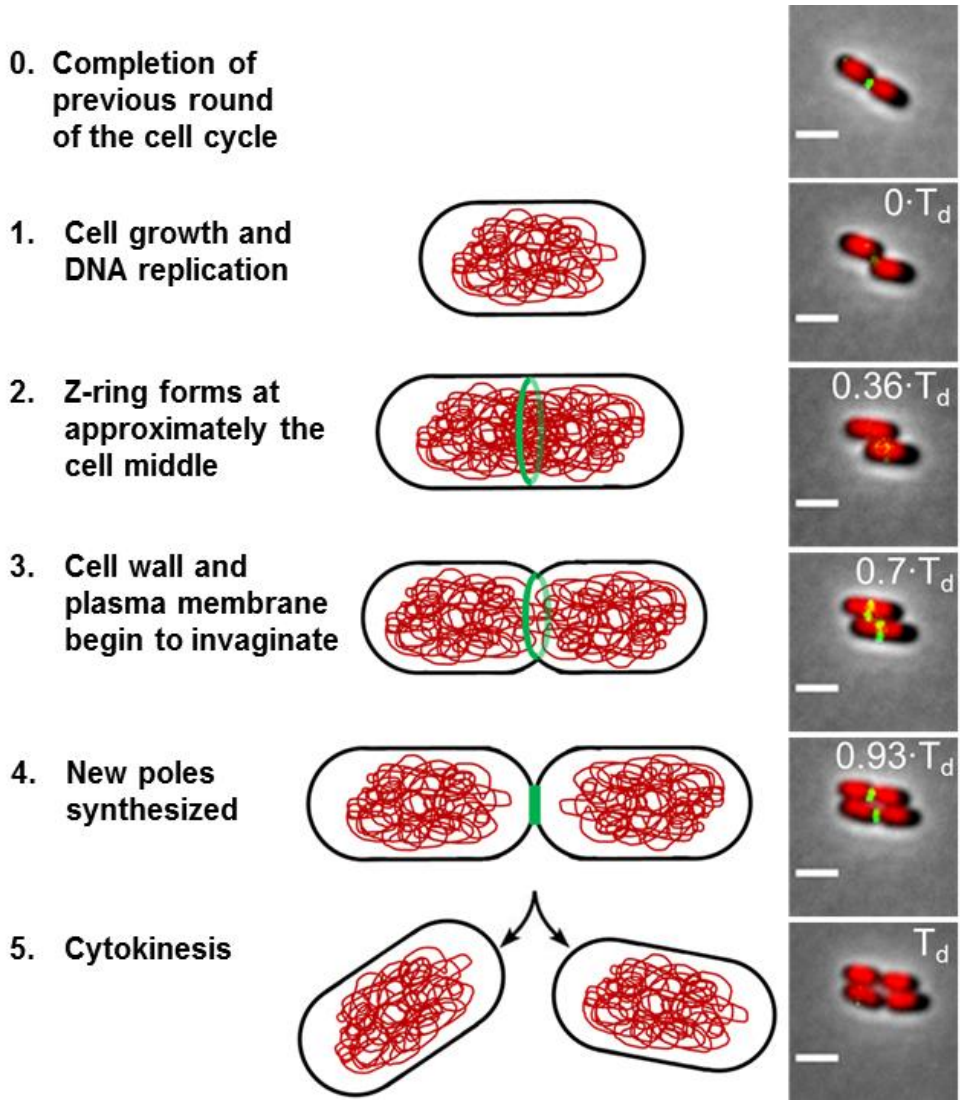

Figure 1. The *E. coli* cell cycle. Schematic (middle panel) and live cell images (right-most panel) showing the progression of bacterial cell growth from birth (0) until division (cytokinesis, 5). The live cell images are from timelapse microscopy of two wild-type *E. coli* cells during one complete cell cycle. Each frame is a composite of three individual images: a phase contrast image (grey) which defines the cell contour, a HupA-mCherry image (red) which shows the bacterial chromosome, and a ZipA-GFP image (green) which is a protein that helps secure the Z-ring to the cell membrane, and therefore represents the Z-ring and/or division plane. Note, T_d stands for doubling time, which for the cells shown here is approximately 120 minutes. All scale bars are 2μm. Generally, cells grow throughout the cell cycle, exclusively along their long axis. During elongation, the circular bacterial chromosome (shown in red in the schematic) replicates. Chromosome segregation occurs comcomitantly with replication. The Z-ring (shown in green in the schematic) is the main macromolecular structure that defines the future division plane. The Z-ring is composed of linear filaments of the protein FtsZ. The Z-ring serves as a scaffold for at least 30 additional proteins that collectively synthesize the lateral cell wall, which compartmentalizes and delineates future daughter cells.

Remarkably, in wild-type *E. coli* this pinching off occurs very accurately in the middle of the mother cell between two separated daughter nucleoids (Trueba 1982, Den Blaauwen, Buddelmeijer et al. 1999, Männik, Wu et al. 2012) (Figure 1, right-most panel). In mutant cells, the inaccurate placement of the Z-ring relative to nucleoids can lead to cells lacking chromosomal DNA completely, i.e. minicells (Adler, Fisher et al. 1967) or to cells that have an incomplete set of genetic material, i.e. have guillotined nucleoids (Niki, Jaffe et al. 1991, Cook and Rothfield 1999, Hendricks, Szerlong et al. 2000). More specifically, in this work we study how the mechanisms which influence Z-ring positioning realize such high spatial accuracy relative to the cell center. How do nanometer-sized FtsZ proteins recognize the center of a cell that is a few micrometers long while simultaneously providing faithful coordination between the divisome and the chromosome?

At the beginning of this work, two molecular systems referred to as 1. the Min system and 2. nucleoid occlusion were known to influence Z-ring positioning to achieve proper divisome – nucleoid coordination and were believed to be responsible for accurate cell division (Figure 1). In the following sections, the Min system and Nucleoid Occlusion are briefly described. The description has been adapted from our review article (Männik and Bailey 2015). However, complete understanding of the Min system and Nucleoid Occlusion are not necessary to follow the implications of the results presented in this work.

The Min system

The three Min proteins, MinC, MinD, and MinE, form a well-understood geometric positioning system for the Z-ring in *E. coli* that defines the cell's geometric middle and prevents polar septations (Lutkenhaus 2007, Shapiro, McAdams et al. 2009, Moseley and Nurse 2010, Lutkenhaus 2012). Fluorescent tagging of the Min proteins has shown that MinC, MinD, and MinE exhibit a remarkable oscillatory behavior in *E. coli* cells, moving back and forth between the two

poles with a typical oscillatory period from 30 seconds to 1 minute (Figure 2A) (Raskin and de Boer 1999). Note, in Figure 2A, only the MinD protein (MinD-GFP) is shown; the oscillatory pattern of MinC is very similar to MinD, whereas MinE primarily labels the membrane. Of these three proteins, only MinD and MinE are necessary to set up the oscillations while MinC, which follows and binds to MinD, is the sole inhibitor of Z-ring formation (Lutkenhaus 2007). MinC binding to membrane-attached MinD activates its inhibitory function (Lutkenhaus 2012). Due to the oscillations, the destabilizing effect of MinC on Z-ring formation is the strongest at the cell poles, where the time-averaged concentration of MinD-bound MinC is the highest (Figure 2B). Consequently, the time averaged concentration minimum of MinC is at the cell center. Ultimately, this negative regulation prevents minicelling at the poles. However, the Min system appears also to play a role in the precise localization of the Z-ring at midcell (Guberman, Fay et al. 2008).

Extensive modelling has been carried out to capture the oscillatory behavior of the Min system based on continuum models and stochastic simulations (Meinhardt and de Boer 2001, Kruse 2002, Huang, Meir et al. 2003, Fange and Elf 2006, Kerr, Levine et al. 2006, Halatek and Frey 2012, Bonny, Fischer-Friedrich et al. 2013). Although different models introduce slight variations in reactions occurring between MinD and MinE, they all can be categorized in mathematical terms as reaction-diffusion systems that exhibit Turing instability (Turing 1952). Interestingly to physicists, the Min system in *E. coli* is the best studied example where the Turning instability mechanism leads to the formation of a dynamic pattern in a living organism.

The Min system functions autonomously from the nucleoid as shown convincingly in *in vitro* reconstituted assays (*in vitro*, see Appendix Glossary) (Loose, Fischer-Friedrich et al. 2008, Ivanov and Mizuuchi 2010, Schweizer, Loose et al. 2011). The same conclusion also can be drawn based on experiments with cells that lack nucleoids but have a functioning Min system. Remarkably, in these cells the Z-ring also can be placed relatively accurately in the middle of the cell (Sun and Margolin 1998, Yu and Margolin 1999, Pazos, Casanova et al. 2014). Taking that

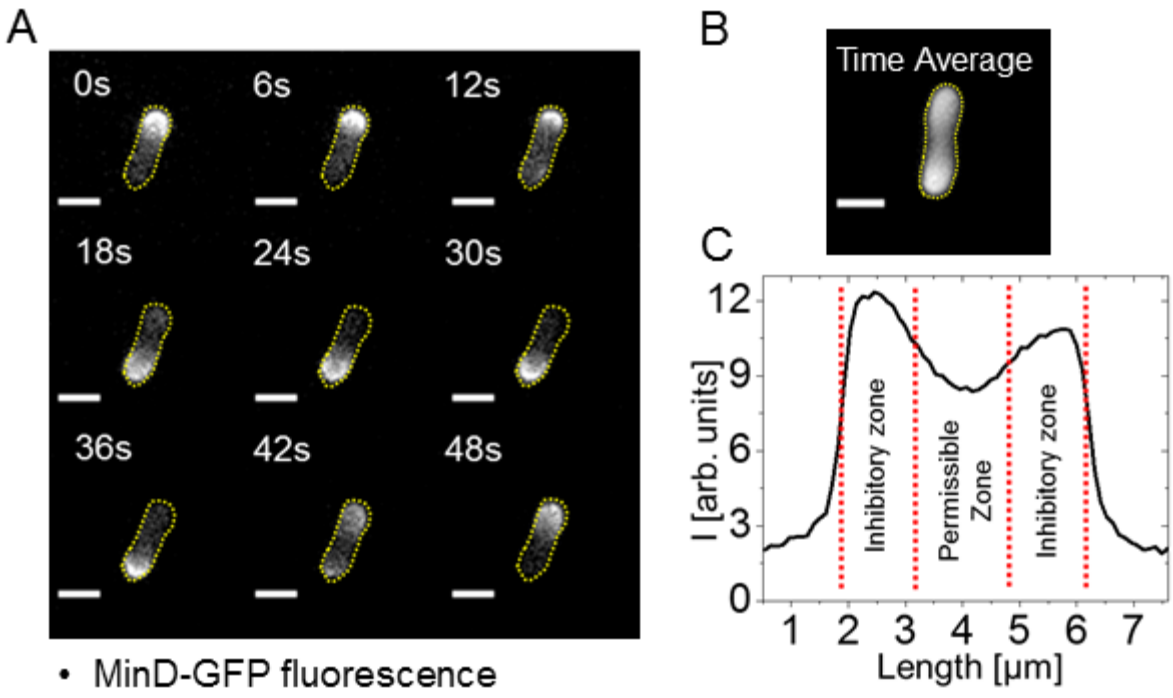

Figure 2. The Min system prevents Z-ring formation at cell poles. The Min system is composed of three proteins MinC, MinD, and MinE that collectively exhibit a remarkable pole-to-pole oscillatory behavior in *E. coli*. (A) Timelapse montage of MinD-GFP fluorescence (strain JMBW2). Each frame is taken at 6 second intervals; the oscillation period for the cell shown here is about 40s. MinC, which is the component of the Min system that inhibits Z-ring formation, oscillates in essentially the same manner as MinD. The yellow dotted lines are an approximate cell contour. (B) Time-averaged MinD concentration from the cell shown in (A). The concentration maximums at the cell poles defines inhibitory zones for Z-ring formation. Scale bars in (A) and (B) are 2 μm. (C) Line profile of the time averaged MinD-GFP fluorescence through the cell's long axis (from panel B). Shown are approximate regions of the cell where the Z-ring is inhibited (cell poles), and a central region where the Z-ring can form.

the two daughter chromosomes separate from each other approximately at mid-cell in normal growth conditions, the Min system alone is perhaps sufficient to coordinate chromosomes and cell division proteins in *E. coli*.

While the Min system is not directly involved in coordinating the Z-ring and chromosomes, an indirect involvement is possible. In fact, several authors have pointed out that deletion of the Min system leads to a small defect in chromosome segregation and in the separation of daughter nucleoids in *E. coli* (Mulder, Elbouhali et al. 1990, Akerlund, Gullbrand et al. 2002, Di Ventura, Knecht et al. 2013, Jia, Keilberg et al. 2014). Di Ventura et al. have proposed that MinD, which is a homolog of the chromosome partitioning protein ParA in the bacterium *C. crescentus*, binds to DNA. These authors propose that MinD oscillation and DNA binding provides a Brownian-ratchet mechanism for DNA segregation and separation (Di Ventura, Knecht et al. 2013). Further experimental support to this interesting idea is still warranted.

SlmA-mediated nucleoid occlusion

The early discussion of coordination between cell division and chromosome replication/segregation centered on the idea of nucleoid occlusion (NO) (Hussain, Begg et al. 1987, Mulder and Woldringh 1989, Woldringh, Mulder et al. 1990, Wu and Errington 2011). The idea of NO is based on observations that constrictions in dividing cells were excluded from the regions occupied by the nucleoids. A major development in the understanding of NO came with the discovery of the Z-ring inhibiting, SlmA protein (Bernhardt and de Boer 2005). Cells that lacked both *slmA* and *minCDE* were not able to divide in rich medium and gave rise to filamentous cells, indicating a defect in cytokinesis. The same authors also observed that some Z-rings could localize over unsegregated nucleoids in Δ*slmA* Δ*minCDE* cells suggesting SlmA played a role in Z-ring positioning.

Further work revealed that SlmA is a DNA-binding protein that inhbits Z-ring formation only when bound to specific repeating patterns of DNA bases, called SlmA binding sites (SBSs).

Two possible molecular mechanisms by which SlmA inhibits the formation of the Z-ring have been proposed. One model posits that SlmA causes depolymerization of FtsZ filaments (Figure 3A) (Cho, McManus et al. 2011, Tonthat, Arold et al. 2011, Cho and Bernhardt 2013, Du and Lutkenhaus 2014). In an alternative model, it was proposed that DNA-bound SlmA does not depolymerize protofilaments but instead captures them and renders them incapable of Z-ring formation (Figure 3B) (Tonthat, Arold et al. 2011, Tonthat, Milam et al. 2013).

One of the more interesting aspects of SlmA-mediated nucleoid occlusion is the distribution of locations where SlmA binds the chromosome. SBSs are distributed throughout the chromosome except for a region around the replication terminus, which is the last region of the chromosome to replicate (Figure 3C) (Cho, McManus et al. 2011, Tonthat, Arold et al. 2011). Consequently, Z-rings are inhibited from forming until the chromosome is nearing the end of replication, which helps ensure that by the time the septal cell wall forms, and the mother cell undergoes cyctokinesis, each daughter cell inherits a complete chromosome. Furthermore, at later stages of the cell cycle, the replication terminus region is positioned approximately at midcell, in the vicinity of the membrane region where the Z-ring typically assembles. In this way, SlmA influences both the spatial and temporal placement of the Z-ring.

While characterization of SlmA at the molecular level has been extensive, understanding its role and function at the cellular level is still limited. How could SlmA that is bound to chromosomal DNA inhibit Z-ring formation at the cell membrane? Models described in (Du and Lutkenhaus 2014) and (Tonthat, Milam et al. 2013), although different in their interaction mechanism between SlmA and FtsZ, both assume that DNA-bound SlmA comes into proximity of the cell membrane to influence the localization of the Z-ring. However, DNA-bound SlmA within the nucleoid makes only limited contacts with the membrane and therefore would interact

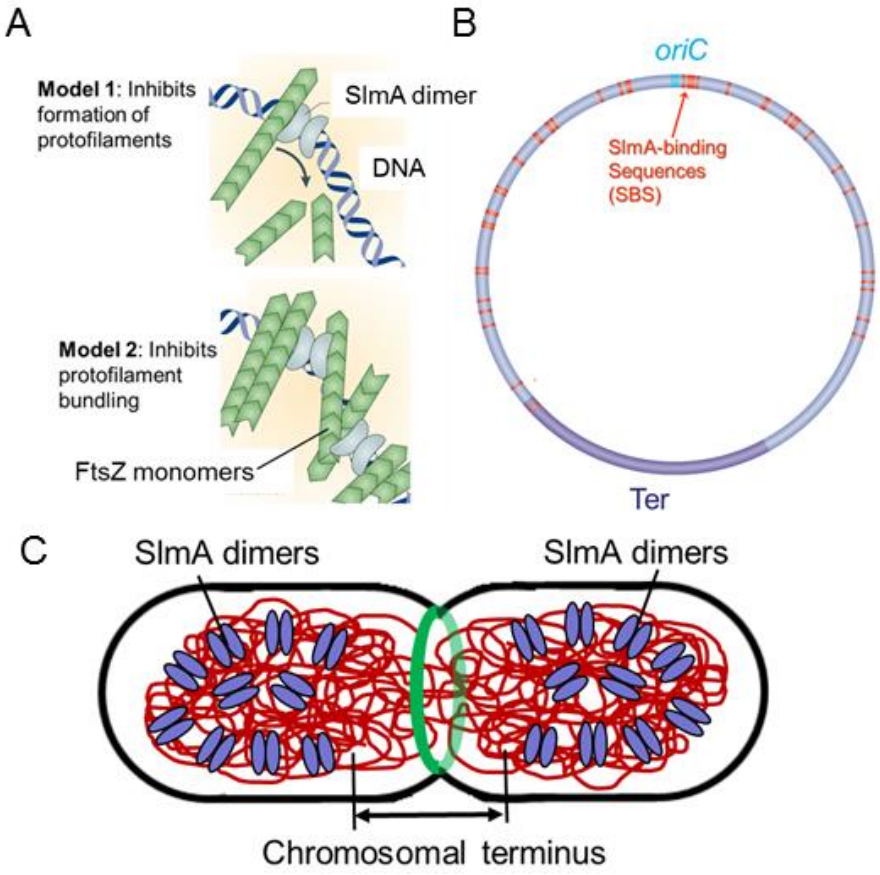

Figure 3. SlmA-mediated nucleoid occlusion. SlmA is a DNA-binding protein that inhbits Z-rings from forming over nucleoids. When bound to specific sequences of DNA, called SlmA binding sites (SBSs), SlmA is thought to inhibit Z-ring formation via one of two mechanisms. (A) Model 1 suggests that SlmA causes depolymerization of FtsZ filaments (Cho, McManus et al. 2011, Tonthat, Arold et al. 2011, Cho and Bernhardt 2013, Du and Lutkenhaus 2014). In Model 2, it was proposed that DNA-bound SlmA does not depolymerize protofilaments but instead captures them and renders them incapable of Z-ring formation (Tonthat, Arold et al. 2011, Tonthat, Milam et al. 2013). (B) SBSs are distributed throughout the chromosome except for the replication terminus region (Cho, McManus et al. 2011, Tonthat, Arold et al. 2011). Binding sites on the circular chromosome are shown by orange lines. Panels (A) and (B) are adapted from (Wu and Errington 2011). (C) As shown in the schematic, the chromosomal terminus region is located near the cell center before cytokinesis starts. Here, SlmA is shown in pairs of purple ovals (SlmA dimers). The distribution of DNA-bound SlmA inhibits Z-rings from forming until the chromosome is nearing the end of replication.

infrequently with membrane-bound FtsZ. Transertional linkages (transertion, see Appendix Glossary) may help to facilitate these contacts (Tonthat, Milam et al. 2013) but the existing microscopy data indicates that SlmA is localized within the nucleoid rather than in the vicinity of the cell surface (Bernhardt and de Boer 2005). Additionally, how effectively SlmA inhibits Z-ring formation in various growth conditions remains yet to be characterized. Nevertheless, in cases where cell shape becomes aberrant (Männik, Wu et al. 2012) the Min system and NO can define different locations for the cell division plane. In conflicting cases, it appears that the NO mechanism dominates over the Min system (Männik, Wu et al. 2012).

Although SlmA mediated NO has received the most attention recently, there is strong evidence that additional mechanisms beyond SlmA can lead to a NO effect in *E. coli*. It was observed that cell division proteins are positioned in accordance with NO in cells lacking SlmA. The NO effect was distinctly present even when the shapes and sizes of these cells were strongly perturbed (Männik, Wu et al. 2012). It was also observed that a replication-inhibited and unsegregated nucleoid at mid-cell blocks Z-ring formation independent of the SlmA and SOS response (Cambridge, Blinkova et al. 2014). How these inhibitory effects of nucleoids are mediated at a molecular level is currently not known, but from these data it is clear that the SlmA-related mechanism is not the only one that realizes NO in *E. coli* cells. The combined influences of the Min system and SlmA-mediate nucleoid occlusion is illustrated in Figure 4.

Z-ring localization in the absence of Min and SlmA

During the discovery of the *slmA* gene, Bernhardt & de Boer made a very interesting observation that under certain conditions cells could still divide even in the absence of both of functional SlmA and Min (Bernhardt and de Boer 2005). Strangely, *E. coli* grown in a nutrient poor medium versus a nutrient rich medium were viable, and even in a nutrient rich environment when FtsZ levels were artificially upregulated (Bernhardt and de Boer 2005). If Min and SlmA are the only two active mechanisms regulating Z-ring placement, then by what mechanism do these

Δ*slmA* Δ*min* cells slowly growing in a minimal medium position their divisome? Furthermore, an evolutionarily divergent gram-positive bacteria, *Bacillus subtilis*, was discovered to be able to grow and divide in the absence of both Min and NO (Rodrigues and Harry 2012) also. While the Min system doesn't operate in the same fashion as in *E. coli* (the inhibitory MinC protein gradient remains statically concentrated at the cell poles in *B. subtilis*, as opposed to oscillating as in *E. coli*), and though the mediator of NO is the "Noc" protein as opposed to SlmA, (Wu and Errington 2004) the function of the two systems remains essentially the same. This discovery suggests that the ability for a cell to divide in the absence of both Min and NO is not a peculiar oddity of *E. coli*, indicating that the mechanism, whatever it is, may be conserved across the evolutionary divide. These findings warrant revisiting the canonical model that the Min system and SlmA/Noc mediated nucleoid occlusion together are the sole factors coordinating the localization of cell division proteins in bacteria.

An excluded volume based hypothesis to explain viability in Δ*slmA* Δ*min E. coli*

If all molecular Z-ring positioning system were in fact removed, we hypothesized that perhaps the physical interactions between the bacteria's chromosomal DNA and FtsZ, in particular between polymerized FtsZ filaments and DNA, could allow the chromosome to serve as a spatial template for Z-ring formation. More specifically, FtsZ forms linear polymers, which are thought to have an average length of about 100 nm long (Chen, Bjornson et al. 2005). If these FtsZ filaments have sufficiently strong excluded volume interactions with DNA, the presence of the bacterial chromosome will define a subcellular volume that is inaccessible to FtsZ filaments (Figure 5). One location for the FtsZ filaments to pool is the space between partially or fully segregated chromosomes (Figure 5). In this way, the bacterial chromosome could influence both the spatial and temporal localization of the Z-ring. Since the Z-ring defines the location of the division plane, a Z-ring placed in between two fully segregated chromosomes would produce two

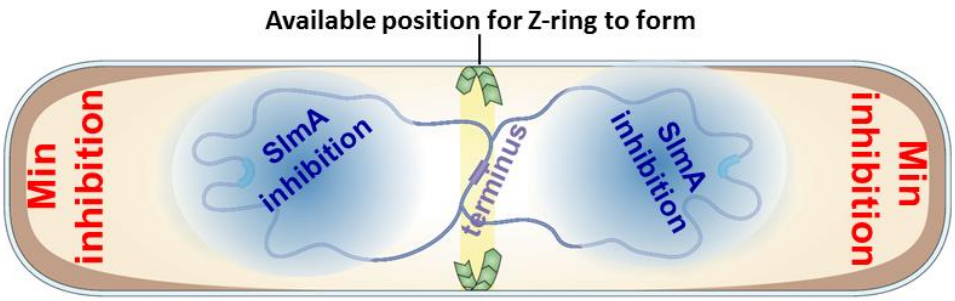

Figure 4. Combined influence on Z-ring positioning from the Min system and SlmA-mediated nucleoid occlusion. The Min system inhibits Z-rings from forming at cell poles. Z-rings at cell poles which lead to the creation of a daughter cell with no chromosome (an anucleate cell), which is inviable. SlmA prevents Z-rings from forming over all regions of the bacterial chromosome except for the replication terminus region. As shown in the schematic, the terminus region is located near the cell center at later stages of the cell cycle before cytokinesis starts. Figure adapted from (Wu and Errington 2011).

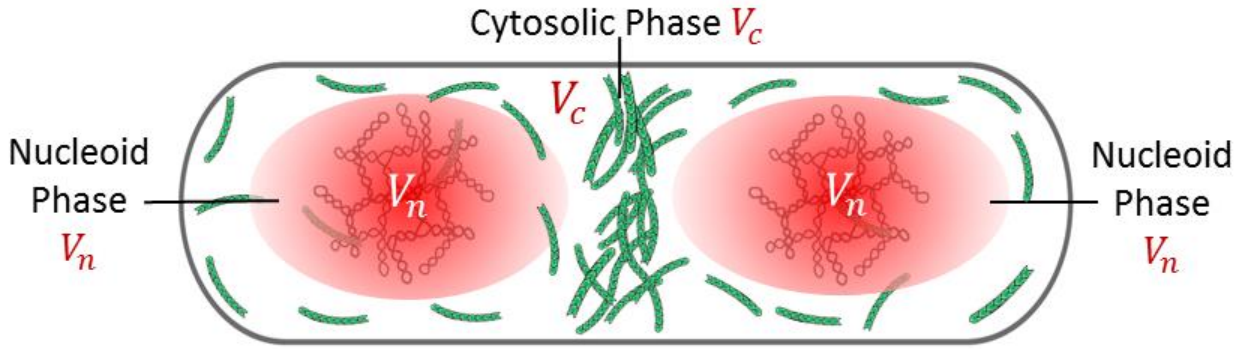

Figure 5. A physical mechanism to explain division plane placement in Δ*slmA* Δ*min E. coli*. We hypothesize that excluded volume interactions between FtsZ filaments and the bacterial, chromosomal DNA will define a subcellular volume (the nucleoid) that is inaccessible to FtsZ filaments (in essence, creating nucleoid and cytosolic phases). Consequently, FtsZ filaments would be concentrated at one of two places, either at the cell poles, or the space between partially or fully segregated chromosomes. In these locations where FtsZ filaments are concentrated, filaments can condense to form Z-rings.

daughter cells which inherited complete DNA copies, and therefore could explain the observed cell viability. We refer to this mechanism as *volume exclusion nucleoid occlusion* (VENO). Using equilibrium statistical mechanics, how effectively the bacterial chromosome expels FtsZ filaments can be estimated. Through this estimation, the reasonableness of VENO as a cell division protein localization mechanism can be evaluated. The remainder of the introduction develops this estimation.

Origins of the FtsZ filament – DNA excluded volume interactions

Excluded volume interactions between FtsZ filaments and the bacterial chromosome originates from two sources, the physical volume of the DNA (in other words, its "hard-sphere," or perhaps more accurately its "hard-cylinder" volume), and its screened electrostatic charge which influences other charged species within the cell. Electrostatic screening arises from the salty, and therefore ionic cytosol which shields other charged species such as proteins, lipids, and DNA. In the model developed here, we completely neglect the effects of electrostratic screening, and consider excluded volume to arise exclusively from an objects physical volume. Accordingly, it should be stressed that our model is nothing more than an order of magnitude estimation, and should be interpreted within that context. Nevertheless, the physical structure and organization of the bacterial DNA must be accounted for.

Physical organization of the bacterial chromosome

Though the average *E. coli* cell length is only a few micrometers (Cullum and Vicente 1978), the circular bacterial chromosome, if stretched out, would measure about 1.6mm long, a little over the thickness of a dime (de Vries 2010). Instead of coiling randomly inside the cell, the 1.6mm chromosome is organized into a network of supercoiled branches or segments, known as plectonemes (see Figure 46 in the Appendix), each of which has a characteristic length of about 160nm, L_{Branch} (Cunha, Woldringh et al. 2001). This length is determined by the inherent stiffness

of the DNA polymer. The diameter of the supercoiled branches is approximately $D_{Branch} = 10$nm (Cunha, Woldringh et al. 2001). Supercoiling in bacteria arises from the induced stress from opening the DNA double-helix during DNA replication and gene transcription (Woldringh 2002). The effect can be easily demonstrated by cutting and stretching a rubber band (about 3-4 times the rest length is good), fixing one end, and twisting the other (e.g., 20-30 times). While maintaining the twist, allow the length of the stretched rubber band to relax until the band begins to coil back over itself. The result is the formation of a supercoil. Bacterial DNA is composed of approximately $N_{Branch} = 4{,}000$ of these supercoiled branches (Woldringh 2002). Interestingly, even though bacteria lack a nuclear envelope to contain the chromosome within, the plectonemic chromosome does not fill the interior volume of the cell, which for *E. coli* growing in nutrient poor conditions is about 0.6 – 0.7 μm^3 (Kubitschek 1990). Rather, the chromosome is compacted into a much smaller region, which depending upon the strain and the growth conditions can range from 0.08 μm^3 (Odijk 1998) to 0.2 μm^3 (Wang, Li et al. 2011); in this state, the chromosome is referred to as a nucleoid. DNA supercoiling alone reportedly compacts the chromosome by a factor of about 10 when compared to a chromosome having no superhelicity (de Vries 2010).

The theoretical work of Theo Odijk suggests that an even more significant contributor to the spatial organization of the nucleoid may originate from osmotic compaction. Compaction of supercoiled, negatively charged DNA is caused by negatively charged, cytosolic proteins through essentially the same mechanism as we hypothesize excludes a large fraction of the FtsZ filaments from within the nucleoid. By balancing both the chemical potential and osmotic pressure between proteins located in the interior of the nucleoid and those proteins located in the cytosol, Odijk showed a phase separation between the cytosol (with a higher concentration of proteins) and the nucleoid (with a lower concentration of proteins) should exist (Figure 6A) (Odijk 1998). Odijk's work predicted a theoretical nucleoid volume of 0.068 μm^3, along with protein volume fractions

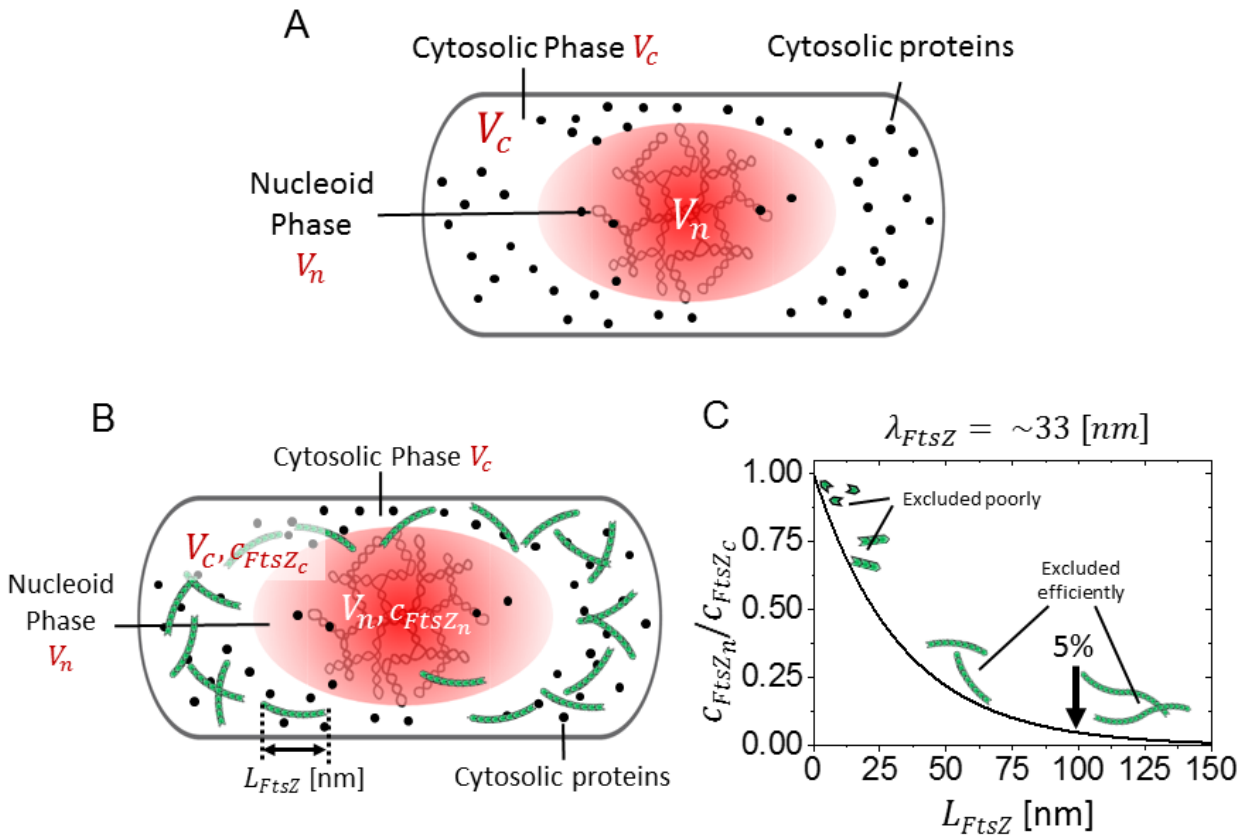

Figure 6. Estimation of the excluded volume effect on the concentration of FtsZ filaments within the nucleoid and cytosolic phases. (A) The bacterial chromosome is organized as a network of supercoiled branches that are compacted into the nucleoid, which occupies about 30% of the cytosolic volume. Odijk's theoretical work predicted that a large component of chromosomal compaction arises from osmotic compaction by the many cytosolic inside the cell (Odijk 1998). (B) Building on Odijk's model, we analyze the distribution of FtsZ filaments of certain lengths within the nucleoid and cytosolic phases. We assume the FtsZ filaments are in chemical equilibrium between nucleoid and cytosolic phases. (C) In our order of magnitude approximation, we find the ratio c_{FtsZ_n}/c_{FtsZ_c} exponentially decreases with incrasing FtsZ filament length. In the approximation presented here, FtsZ monomers and short FtsZ filaments are poorly excluded, however 95% of filaments 100nm or longer are excluded from the nucleoid. *In vitro* results suggest FtsZ filaments *in vivo* are approximately 100nm in length (Chen, Bjornson et al. 2005).

within the nucleoid region, and in the surrounding cytosolic region of 0.06 and 0.166, respectively. Interestingly, these values agree well with that measured from bacterial cells (Odijk 1998).

Adding FtsZ filaments to Odijk's existing model

To estimate how well the bacterial chromosome excludes FtsZ filaments, an extension to Odijk's model was made to accommodate FtsZ filaments. More specifically, the estimate's objective is to express the equilibrium concentrations of FtsZ filaments inside the nucleoid relative to the concentration outside the nucleoid as a function of filament length. We consider our system to be composed of a simplified bacterium of volume V, inside of which is a nucleoid of volume V_n possessing a corresponding cytosolic volume V_c (which surrounds but does not contain the nucleoid volume) such that $V = V_n + V_c$. In addition to the nucleoid, we consider only two different types of proteins, evenly dispersed globular (spherical) proteins having nucleoid and cytosolic concentrations c_{p_n} and c_{p_c}, respectively, and FtsZ filaments (cylinders) which have nucleoid and cytosolic concentrations c_{FtsZ_n} and c_{FtsZ_c} (Figure 6B). It should be mentioned that cytosolic proteins come in a variety of shapes, sizes, and net electric charge. In this approximation, we assume all proteins are spherical, and have the same size. Moreover, as previously mentioned, we completely neglect the effect of electric charge, assuming the ionic cytosol completely screens all electric charge. Moreover, we assume all FtsZ cylinders have the same length L_{FtsZ}.

The ratio of concentrations c_{FtsZ_n}/c_{FtsZ_c}as a function of FtsZ filament length can be determinied by equating chemical potentials of the FtsZ filaments within the nucleoid and cytosolic volumes ($\mu_{FtsZ_{nucleoid}} = \mu_{FtsZ_{cytosol}}$). We express the total FtsZ filament chemical potential as:

$$\mu_{FtsZ_{Total}} = \mu_{FtsZ_{solute}} + \mu_{FtsZ-protein} + \mu_{FtsZ-DNA}$$

Here, we consider only leading order contributions to the chemical potential, therefore we neglect the FtsZ-FtsZ self-interaction term (see Appendix). We consider FtsZ filaments as a dilute solute,

therefore the corresponding chemical potential, arising from the filament's mixing entropy, can be expressed as:

$$\mu_{FtsZ_{solute}} = \mu_{\mathrm{ref}} + k_B T \cdot \ln(c_{FtsZ})$$

where μ_{ref} represents a convenient reference potential, and includes the solvation energy of the solvent. In chemistry, the reference potential is usually defined when all molecular components are at a 1M concentration (Phillips, Kondev et al. 2012).

The terms $\mu_{FtsZ-protein}$ and $\mu_{FtsZ-DNA}$ represent the excluded volume interaction contributions to the chemical potential. Excluded volumes can be expressed using the second virial coefficients B_{i-j}, where the subscripts i and j indicate the excluded volume is to be evaluated for the interaction of species i with species j. In this form, the interaction chemical potentials take the form:

$$\mu_{FtsZ-protein} = k_B T \cdot \frac{N_p}{V} \cdot B_{FtsZ-protein}$$

$$\mu_{FtsZ-DNA} = k_B T \cdot \frac{N_{Branch}}{V} \cdot B_{FtsZ-Branch}$$

Note that in the interaction between FtsZ and DNA, the quantities N and B have subscripts containing the reference for "branch". In this context, branch refers to the supercoiled DNA branches that compose the bacterial chromosome. For the excluded volume between spherical cytosolic proteins and cylindrical FtsZ filaments, we use (see Figure 46 in the Appendix):

$$B_{FtsZ-protein} = \pi \cdot E_{exc}^2 \cdot L_{FtsZ}$$

In other words, we assume the excluded volume is cylindrical, with length equal to the length of an FtsZ filament, and exlusion radius E_{exc} approximately equal to the sum of the FtsZ cylinder's radius and spherical cytosolic protein's radius (Odijk 1998). Following Odijk's model, we also treat supercoiled DNA branches as cylinders. The approximate excluded volume between two cylinders oriented at an angle θ relative to their long axes goes as (see Figure 46 in the Appendix):

$$B_{i-j} = \frac{\pi}{4} \cdot (D_i + D_j) \cdot L_i \cdot L_j$$

Where D and L represent the diameters and widths of cylinders i and j (see Appendix).

With expressions for each B_{i-j}, equating the total chemical potential between nucleoid and cytosolic volumes and solving for c_{FtsZ_n}/c_{FtsZ_c} as a function of L_{FtsZ} will reveal the equilibrium distribution of FtsZ filaments. In leading order of L_{FtsZ}, the results of the approximation (explained in detail in the Appendix) reveals c_{FtsZ_n}/c_{FtsZ_c} depends exponentially on the filament length.

$$\frac{c_{FtsZ_n}}{c_{FtsZ_c}} = e^{-\frac{L_{FtsZ}}{\mathcal{L}_{FtsZ}}}$$

The constant $\mathcal{L}_{FtsZ}$ describes the length of the filaments required to decrease the ratio c_{FtsZ_n}/c_{FtsZ_c} by a factor of $1/e$ and provides a metric for how well supercoiled DNA can exclude filaments. We estimate $\mathcal{L}_{FtsZ}$ to be 33nm, which at an average FtsZ filament length of ~100nm, suggests less than 5% of the filaments are expected to reside within the volume occupied by the nucleoid (Figure 6C). Consequently, it does seem plausible that the bacterial nucleoid could serve as a spatial template for the positioning of the FtsZ filaments that compose the Z-ring (Figure 5).

The remaining chapters describe both the methodology and the results of experiments designed to test the VENO hypothesis. Specifically, Chapter 1 describes the experimental methods and techniques used to generate the results presented in Chapters 2 and 3. The results from Chapter 2 have been published in PLOS Genetics (Bailey, Bissichia et al. 2014), and the results presented in Chapter 3 have been submitted. Chapter 4 presents outstanding questions raised as a consequence of the findings presented in Chapters 2 and 3. Chapter 4 also presents preliminary results from experiments performed in attempts to address some of these questions. Following the conclusions, more technical information, such as details to the VENO derivation, a list of all strains used etc., is contained in the Appendix, along with a glossary of commonly used terms.

Chapter 1: Materials and Methods

To study cell division in *E. coli*, we often desire to understand the functional role of a particular protein in the division process, or perhaps identify if a given protein has any consequences upon cell division at all. The typical experimental methodology involves monitoring the protein(s) of interest in living cells by a technique known as fluorescent protein labeling. In all experiments in this work, we label proteins of interest by fusing them with exogenous fluorescent proteins (originally from non-bacterial organisms). Occasionally, in addition to constructing the protein fusion(s), other potentially-related genes are deleted from the chromosome. We visualize fluorescent proteins as cells grow and divide using a fluorescence microscope, providing information about proteins' spatial distribution or localization, dynamics, and association with other intercellular components such as DNA, the cell membrane, and/or other proteins. Fluorescent imaging of fusion proteins, often in the presence of other gene deletions, followed by digital image analysis enables us to quantitatively characterize the effects of a variety of proteins on the overall growth and division of the cells. In this way, we reconstruct the mechanistic details of cell division. Accordingly, the experimental workflow can be broken down into the following broad categories: 1. bacterial strain construction, 2. bacterial growth, 3. imaging, and 4. digital image analysis. The transition from a qualitative to a quantitative description of cell biology is made possible in part by the creation of digital image analysis software. Though in the experimental pipeline digital image analysis is the last process, I shall discuss it first due to its pivotal role in the scientific results presented in this work. Our lab also fabricates microfluidic devices to manipulate bacteria physically and to dynamically control their growth environment (for nutrient and drug delivery purposes) during imaging. I will describe briefly the production process of some of our first microfluidic chips and provide an illustration of how cells grow within the device.

Quantitative image analysis

While the past couple of decades has witnessed the rapid development of fluorescence microscopy, digital image analysis has played a fundamental role in this development (Kenneth R, Wu et al. 2008). The primary challenge to quantitatively analyzing microscope images is the identification of the objects of interest (foreground) from everything else (the background). This task is called image segmentation (segmenting the foreground from the background), and before outlining the general concepts, it is important to understand the difference between the microscope image and its digitized representation. The image created by the microscope (optical image) can be thought of as a continuous 2D function of two real space variables, $I(x,y)$, where I represents light intensity. To generate a digital representation, the continuous optical image is sampled on a rectangular grid (commonly, as in our case, using a CCD camera) with grid elements (pixels) located at discrete positions (m,n). In addition to discretizing space, the camera also discretizes intensity values. The result is the digital image, that is, a 2D matrix of integer intensity values as a function of discretized space $I(m,n)$. Image segmentation and all other image manipulations are therefore numerically realized by applying one or more matrix operations to the digital image $I(m,n)$.

There are two common strategies for segmenting an image, thresholding and edge-finding (Young, Gerbrands et al. 1998). Thresholding is conceptually and computationally simple and decomposes the image into the foreground and background according to whether or not the intensity of each pixel is above or below a predefined intensity threshold $I_{\text{Threshold}}$.

$$I(m,n) = \begin{cases} F, & \text{if } I(m,n) \geq I_{\text{Threshold}} \\ B, & \text{if } I(m,n) < I_{\text{Threshold}} \end{cases}$$

The result is the identification of the foreground objects (F) and the objects belonging to the background (B). Thresholding is particularly useful for images containing objects of interest that have near uniform intensities against a background with a near uniform but differing intensity. (Kenneth R, Wu et al. 2008). For bacteria imaged using a common technique called phase

contrast microscopy (described in more detail in the Imaging section below), bacteria appear as dark regions upon a light background, and thresholding can often successfully determine regions fully inside and fully outside a cell. A common limitation of thresholding, however, is the failure to generate smooth cell contours, which can be important for determining the relative location of objects, like proteins, within the bacterium. To circumvent this limitation, some researchers have employed boundary-pixel interpolation strategies to better predict the smooth cell contour (Guberman, Fay et al. 2008).

Alternatively, segmentation can be performed by attempting to determine the cell contour, or in general object boundaries, directly. Generally, these segmentation methods are referred to as "edge-finding", and are more applicable when bacteria may not appear uniform in intensity against a contrasting background, or when several bacteria are in contact with one another in microscope images. In an image, object edges correspond to those points where the intensity values abruptly change (Kenneth R, Wu et al. 2008). Consequently, object edges can be approximated by computing the derivatives of the digital image intensity with respect to pixel location. Several forms of derivative based edge detection algorithms exist that utilize first and/or second derivatives. Instead of using the first derivative, our image analysis software uses a combination of two second derivatives, namely, the sum of the Laplacian of the image, and the second derivative in the gradient direction. Defining $I(m,n)''$ as this second derivative image:

$$I'' = \nabla^2 I + \frac{I_{mm}I_m^2 + 2I_{mn}I_mI_n + I_{nn}I_n^2}{I_m^2 + I_n^2}$$

where,

$$I_m = \frac{\partial I}{\partial m}, I_n = \frac{\partial I}{\partial n}, I_{mm} = \frac{\partial^2 I}{\partial m^2}, I_{nn} = \frac{\partial^2 I}{\partial n^2}, I_{mn} = I_{nm} = \frac{\partial^2 I}{\partial m \partial n}$$

In this case, the zero crossings of the sum of both second derivatives approximates the edges of objects of interest an order of magnitude more accurately than if either second derivative were used alone (Kempen, Ginkel et al. 2014).

For our implementation of cell segmentation, a combination of thresholding and edge-finding routines are used to create a binary image mask that outlines the cell of interest. The product of the image mask with the original image is an image the same size as the original with all pixel values equal to zero except for the region defined by the mask, which assume the same intensity values as the original image. The algorithm proceeds as follows:

1. Compute the second derivative of the original fluorescence image (Figure 7A) in the gradient direction and the Laplacian of the image, and construct a new image from the sum of both derivatives (Figure 7B). Specifically, we use the *laplace_plus_dgg* function from the DipImage library (Kempen, Ginkel et al. 2014).
2. Construct a binary image where values less than zero in the derivative image are foreground (1) and values greater than zero are background (0) (Figure 7C). Pixels belonging to the boundary between foreground and background pixels represent the edges of the objects of interest.
3. Identify groups of pixels sharing the property of being foreground objects using the restriction that groups have a predefined size or pixel connectivity (Figure 7D). This process is referred to as image "labeling". In the case of bacterial imaging, labeled images usually are sufficient to approximate what objects are cells and what objects are not.
4. Select the particular group of pixels belonging to the object of interest from the labeled image and construct a new image where the selected pixel group becomes the sole foreground object (1) and everything else becomes the background (0) (Figure 7E).
5. Usually, successive morphological image processing operations called dilations and erosions are applied to the resulting binary image, which will become an image mask, to smooth the foreground-background boundary from extraneous pixels so that the binary image foreground edge is geometrically more similar to the smooth contour of rod-shaped *E. coli*.

6. The smoothed binary image delineating the cell of interest, the mask, is then multiplied with the original image producing the final segmented image containing only the cell of interest (Figure 7F). At this point, biologically relevant information can be extracted or measured from the segmented image.

From the segmented image alone, many useful quantities can easily be determined. If a cytosolic protein is being used, as in Figure 7A, from the total fluorescence from the cell, which is the sum of all intensities in image Figure 7F, one can approximate the cell volume (an analysis comparing daughter cell volumes, for example, is pertinent to results described in Chapter 2). Similarly, the apparent 2D cell area, or size of the nucleoid at various stages in the cell cycle, can be approximated by the number of pixels contained in the cell nucleoid mask when multiplied by the pixel area. Moreover, the cell or nucleoid length can be approximated from the construction of a bounding rectangular box around the cell or nucleoid mask.

For some digital image analyses, sufficient information about subcellular organization and dynamics can be obtained without the need of complete cell segmentation. In this case, the fluorescence intensity of the objects of interest (such as fluorescent proteins) exclusively along the long axis of rod-shaped *E. coli* can be extracted and measured relative only to the long-axis cell edges (Figure 7G, H). We employ one of two methods to extract intensity line profiles depending on whether cells in images are well isolated, typically in static images (a single time point), or whether cells are not isolated (closely neighboring or in physical contact with other neighboring cells), which is more common in timelapse imaging.

In the case of well isolated cells, cell centers are measured from phase-contrast images (described in the Imaging section below) using the Cload function of the PSICIC software package, mentioned above (Guberman, Fay et al. 2008). Cload is an implementation of a thresholding algorithm that separates foreground objects according to a user-defined cell edge or contour level. Subsequently, Cload performs an interpolation procedure to smooth the resulting cell edge, to determine approximate cell contours and midlines of each cell.

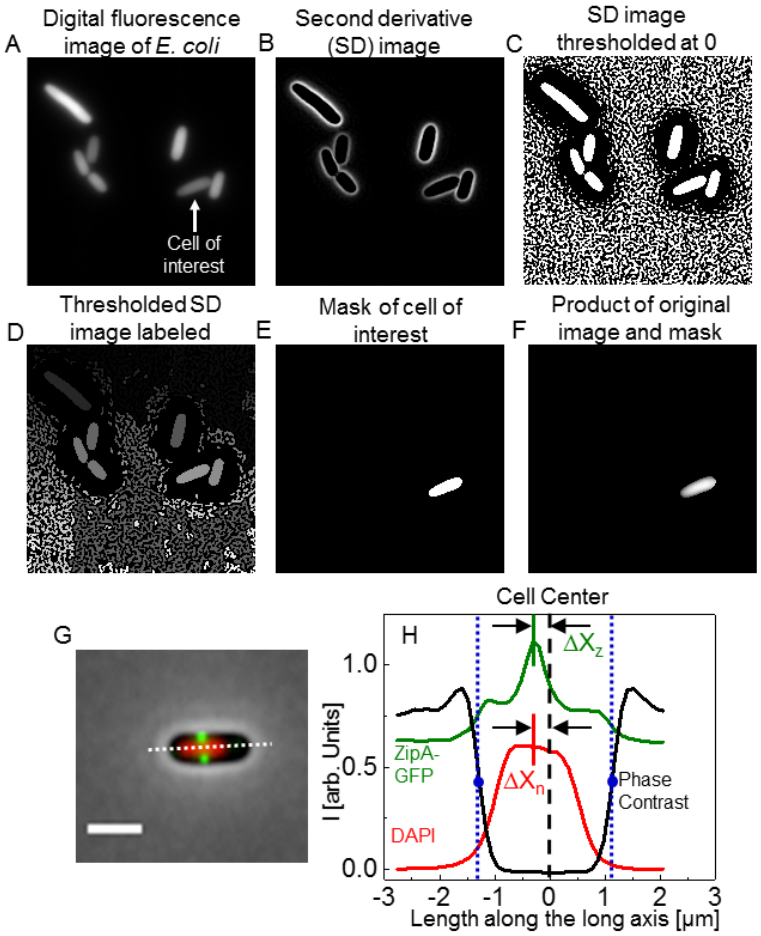

Figure 7. Quantitative image analysis. Cell segmentation (A) – (F). (A) Image of E. coli expressing a cytosolic green fluorescent protein. The arrow indicates a cell of interest which will be segmented from the remainder of the image. Notice that the cell of interest is touching a neighboring cell. (B) Image constructed from the sum of the Laplacian and the second derivative in the gradient direction of image (A). (C) Binary image produced from image (B) by marking pixels with intensity less than to zero as foreground (1), and pixels with intensity greater than or equal to zero as background (0). The boundary between foreground and background pixels defines potential cell edges. (D) Image composed of pixels regions from (C) grouped by pixel connectivity and the number of pixels in the group – a "labeled" image. Groups with a reasonable number of pixels likely represents a cell. (E) A binary image is constructed from the labeled image containing the group of pixels pertaining to the cell of interest. This group becomes the only foreground object and all else becomes the background. This image is the image mask. (F) The result of multiplying the image mask (G) by the original image (A). **Intensity line profiles (G) – (H).** (G) Composite image of ZipA-GFP (green), DAPI stained nucleoid (red) and phase contrast images (grey) of a Δ*slmA* Δ*min E. coli* cell with a distinctly off-center placed nucleoid. The white dashed line represents an approximate manual cell midline. The scale bar is 2 μm. (H) The intensity line profiles of each image plane (phase contrast, GFP, and DAPI) along the long axis of the cell for the cell shown in panel (G). The cell edges are defined as the zero crossings of the second derivative of the phase-contrast image plane (intersection of vertical blue small-dashed lines and phase-contrast profile [blue marker]). The same procedure is used to find the edges of the nucleoid (not highlighted).

Technically, Cload does perform segmentation, but it utilizes the cell boundary to construct a more reproducible, and therefore systematic, cell midline. As part of this work, an addition to the PSICIC software was made to automatically determine the contour level thresholds for each cell. We define the contour level threshold as the averaged intensity value of all inflection points that surround the cell. The inflection points are calculated from the same *laplace_plus_dgg* function from the DipImage library that we use in our implementation of cell segmentation. Midline coordinates are used to determine the geometrical center of the cell (the midpoint of the midline), relative to which we determined the positions of the fluorescent proteins of interest, and fluorescently labeled chromosome. The midline is used also to calculate the length of the cell.

For non-isolated cells, Cload often fails to correctly segment cells which corresponds to inaccurate midlines. Consequently, we approximate the midline by manually drawing either a straight or segmented line along the long axis of the cell from which fluorescence intensity information is extracted. Manually drawn line profiles are less systematically reproducible than fully automated profiles, however. To increase the reproducibility, all midlines (both Cload and manually generated) are broadened by constructing two additional parallel curves on each side of the midline. The resulting broadened midline spans a total width of about 0.54μm. Along each of the five "midlines," the fluorescence intensities are interpolated (using cubic spline). The fluorescence intensities from each curve is averaged in the perpendicular direction to the midline to define an effective intensity line profile along the long axis of the cell. Averaging midlines in this way helps account for slight irregularities, particularly in manually drawn line profiles.

Similarly to Cload, the location of fluorescent proteins of interest from manually drawn intensity line profiles, are measured relative to the cell center (measured from phase contrast images). The coordinates of the manually drawn line profile are mapped to the same coordinates of the second derivative image (*laplace_plus_dgg*) from which the inflection points (defining the edges of the cell) are determined. The particular coordinate of the inflection point is specified by interpolating linearly between the two coordinates in which the second derivative changes sign.

This procedure yields the coordinates of the outermost edges of the nucleoid with sub-pixel resolution (blue dots in Figure 7H). The midpoint between both inflection points approximates the cell center. To determine the location of fluorescent proteins, for example the ZipA-GFP labeled Z-ring, the intensity distribution along the entire broadened midline is plotted (Figure 7H). From this extended profile, a region containing an intensity maximum, which corresponds to a Z-ring in this example, is manually selected. The selected region is then fit to a Gaussian. The distance between the center of the Gaussian and the cell center determines the distance ΔX_Z. The geometrical center of the nucleoid is found in essentially the same way as the cell center, however more care must be taken in this case since more inflection points may exist in the intensity distribution, especially when the nucleoid has started to segregate. Intensity line profiles from either the automated Cload program or those that are manually drawn appear as that shown in (Figure 7H).

All image analysis code is written in Matlab with the Image Analysis Toolbox and the publicly available DipImage Toolbox (http://www.diplib.org/). For some intensity line profile analyses, the software package PSICIC is used, another publically available Matlab extension (Guberman, Fay et al. 2008). In addition to Matlab, simpler image processing such as contrast and brightness adjustments were done using ImageJ software.

Imaging

Following successful strain construction containing the fluorescent fusion proteins of interest and or gene deletions (described below), cells are imaged on our Nikon Ti-E inverted fluorescence microscope (Figure 8A). We utilize two primary modes of imaging, one to ascertain the cell contour (transmitted light mode), and another to track the fluorescent proteins inside the cell relative to the cell contour (fluorescent light mode). There are a number of transmitted light techniques, however we use the phase contrast technique which converts small changes in phase between light diffracted as it passes through the bacteria and light which does not pass through

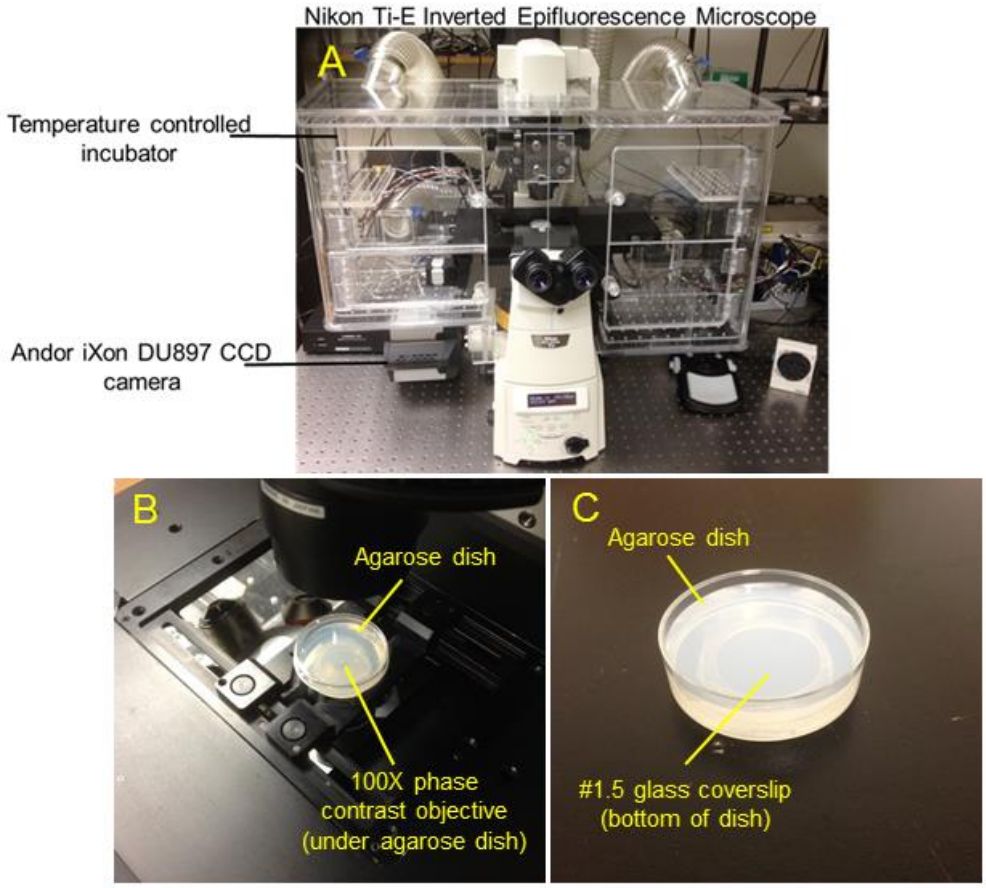

Figure 8. Imaging system. (A) All imaging experiments presented here were performed on a computer controlled, Nikon Ti-E inverted fluorescence microscope. Cells are imaged within a temperature controlled environment (*In Vivo* Scientic incubation chamber). Phase contrast and fluorescence images are captured with an Andor iXon DU897 CCD camera. (B) Close up of the microscope stage. For timelapse images, cells are imaged on an agarose dish. Also shown (under the agarose dish) is the 100X, oil immersion phase contrast objective. (C) Close up of the agarose dish. To load bacteria, the agarose slab is first removed from the dish. 1µL of the cell culture is pipetted directly onto the coverslip and the agarose slab replaced, which spreads the cell culture uniformly across the surface of the coverslip.

the bacteria but around it into corresponding changes in amplitude. In our system, bacteria appear dark against a lighter, gray background (cf. Figure 7G). We use a 100X, oil immersion phase contrast objective which has a 1.40 numerical aperture (Figure 8B).

In fluorescence mode, the microscope irradiates the bacteria with specific wavelengths of visible light, which are absorbed by fluorescent proteins, and subsequently separates the proteins' emitted light. Ideally, only the emitted light reaches the detector (eyepiece or CCD camera) leaving the fluorescent structures against a dark background (cf. Figure 7A, G). A 200W Mercury lamp (an incoherent light source), attenuated by either ND4 or ND8 neutral density filters, is used to excite the fluorophores. The excitation filter, dichromatic mirror (beam splitter), and emission filter are contained in a single optical block called a filter cube. Each fluorescent protein imaged requires a specific filter cube. Specifically, we use Chroma 41004, 41001, and 31000v2 filter cubes to record mCherry (a red fluorescent protein), GFP, and DAPI images, respectively.

Often, only a few tens of certain fluorescently-labeled proteins of interest are present within the cell, leaving the emitted light levels very low. The most straightforward approach to improve the signal is to collect more light by taking longer exposures or by increasing excitation light intensity. Unfortunately, either approach can increase phototoxicity, and kill cells. Alternatively, we capture images using an Andor iXon DU897, an electron multiplying CCD camera, which incorporates an on-chip multiplication gain register that permits single photon sensitivity with 96% quantum efficiency (Figure 8A). Effectively, applying gain adjusts the number of photoelectrons that determine each gray level, which is particularly useful in low light (nearing single photon) acquisition conditions. Furthermore, the camera is thermoelectrically cooled to reduce dark current (thermal electrons).

In a typical timelapse measurement, between 10 and 20 locations (of size 55μm x 55μm) containing between 5-15 bacteria are chosen. Phase contrast and fluorescence images are taken at each location in 8 minute intervals for 12-16 hours. Images are recorded using Nikon's NIS-Elements software. Throughout timelapse measurements, cells are maintained at a fixed

temperature. We use an *In Vivo* Scientic incubation chamber which surrounds the microscope stage (Figure 8A).

Another important characteristic of an imaging system is the point spread function (PSF). The PSF describes the response of an imaging system to a point source of light, which appears as an Airy diffraction pattern in the focal plane. Knowing the PSF is useful in understanding the smallest object the microscope can resolve, and in our application is particularly useful when needing to deconvolute images. Due to diffraction, images of bacteria tend to have blurred edges. The effect is far more exaggerated when imaging individual fluorescent proteins which are much smaller in size than the width of the microscope's PSF. Having a good approximation of the PSF of the microscope allows for much of the blurring to be removed following deconvolution. We estimate the PSF of our microscope by measuring the widths of 4nm quantum dots (QDs), an approximate point emitter of light, (gift from Professor Alexei Sokolov). Widths are determined from fitting fluorescent images of QDs with a two-dimensional, circular Gaussian and then extracting the width σ (Figure 9A). Numerically, the microscope's PSF is realized as a Gaussian whose σ matches that measured from QDs (Figure 9B) since the Gaussian is a good approximation of the central peak of the Airy function (which is a first order Bessel function of the first kind). For our microscope, we measure the fitted widths of 4nm QDs, having a 620nm emission wavelength, to be 1.06 pixels on average (each pixel is 107nm x 107nm). Results of subsequent image deconvolution are shown in (Figure 9C, D).

Microfluidic chips

Traditionally, bacteria are imaged on a microscope slide, or small dish (Figure 8C), covered or filled with a nutrient rich medium made solid by the addition of a plant-based hydrogel named agar or agarose. Imaging bacteria on agarose pads or dishes for extended periods of time leads to micro-colony formation. The cell density continues to increase until the entire field of view is filled with cells oriented side-by-side or in some cases even on top of each

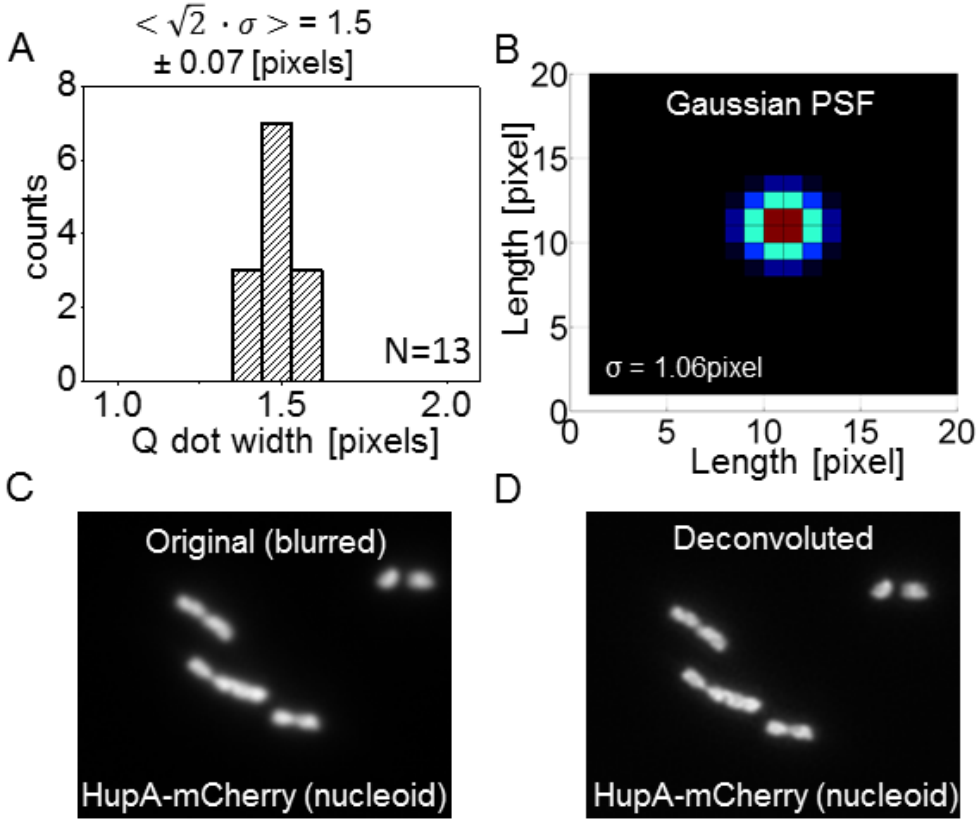

Figure 9. Approximate PSF and image deconvolution. (A) Histogram of 2D Gaussian-fitted widths of Quantum Dots imaged with our microscopy system (N=13, σ=1.06 pixels). (B) 2D heat map representation of Gaussian point spread function (PSF). Red color represents higher fluorescence intensity, and blue colors represent lower fluorescence intensity. (C) Example blurred image of *E. coli* nucleoids labeled with fluorescent HupA-mCherry. (D) Same image as (C) following deconvolution with the PSF shown in (B) generated with Matlab's deconvblind function.

other. Consequently, image analysis becomes almost impossible. Furthermore, with agarose slides or dishes there is no way to change the bacteria's growth environment, such as the addition of a particular nutrient, or the addition of a drug. To circumvent these limitations, we develop microfluidic devices based on the soft-lithography polydimethylsiloxane (PDMS), a transparent, bio-compatible silicone rubber (Figure 10A).

The basic design of the first generation of chips follows (Wang, Robert et al. 2010). The microfluidic circuit consists of a central channel through which the bacterial culture flows (Figure 10A, B). This flow channel is approximately 6mm long x 200μm wide x 1.2 μm deep. Perpendicular to the central flow channel and on each side are about 300 dead end channels separated by 20μm. These dead end side-channels are much smaller, and vary in lengths and widths (15μm – 20μm long x 0.5μm – 1.0μm wide x 1.2μm deep). When bacteria are introduced into the flow channel at sufficiently high concentrations, bacteria migrate into the side pockets. The flow channel then can be flushed, eliminating all bacteria in the flow channel, leaving only those within the side-pockets for imaging. Fresh media is flowed continuously through flow channel (about 5uL/hr) and nutrients diffuse into the bacteria-filled side pockets allowing cells grow and divide in a single file line for days. As the cells within the pockets grow, they push on their neighbor cell. In time, the only cell that isn't expelled from the side pockets into the flow channel (and eventually exit the chip) is the mother cell at the very end of the dead end pocket. Accordingly, we refer to this chip design as the "mother machine".

The PDMS is patterned using a silicon master, which is fabricated at Oak Ridge National Laboratory's Center for Nanophase Materials Science (CNMS) complex (Figure 10C). The silicon chip is constructed in two steps. First, the smaller bacterial pockets are constructed by electron-beam lithography (JEOL JBX-9300FS). An e-beam resist (ZEP520A), is spin-coated and baked. Upon e-beam exposure, the resist is broken down and later removed in a developing solution producing an e-beam mask. Reactive ion etching (Oxford Plasmalab 100) is used to transfer the

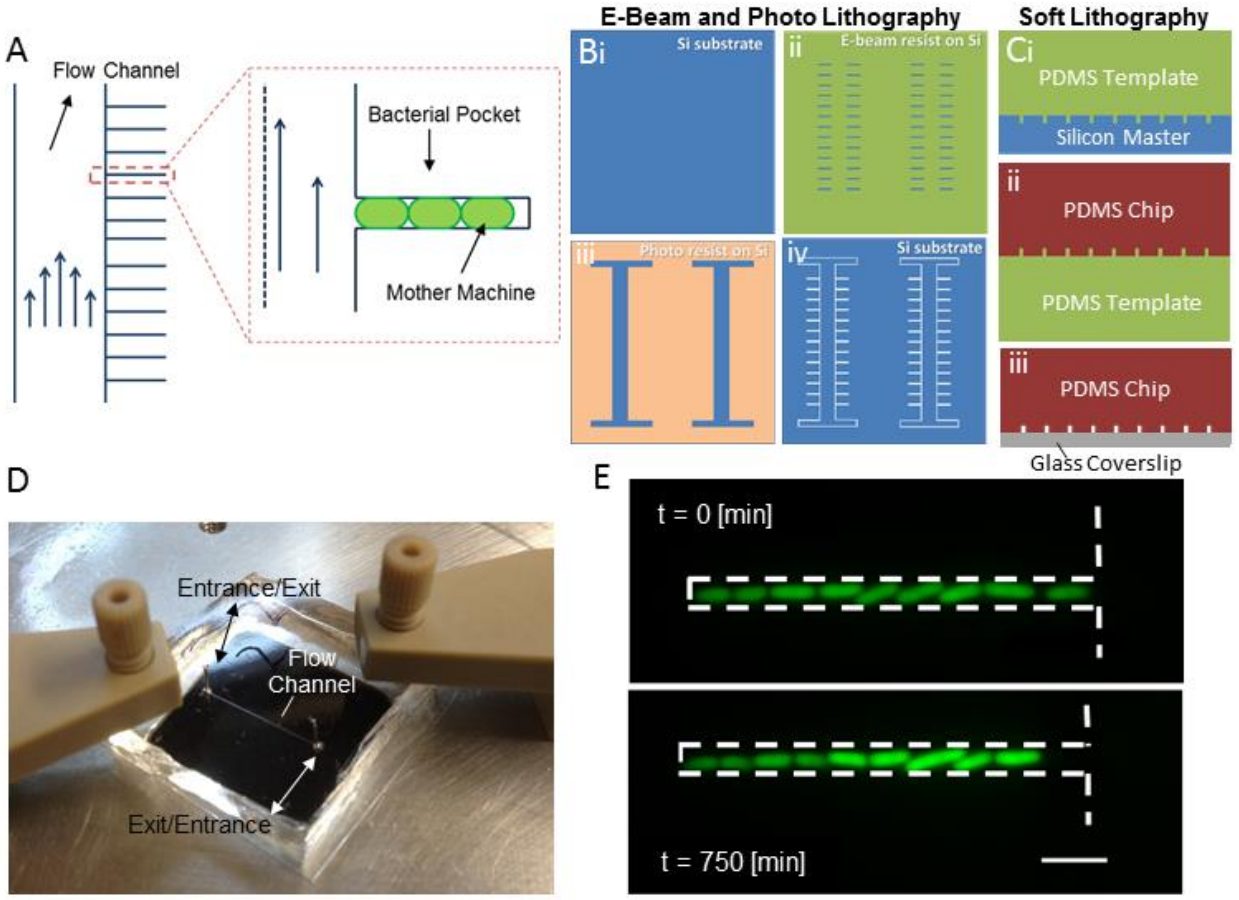

Figure 10. Microfluidic chip fabrication. (A) Schematic of the mother machine design showing the dead end bacterial pockets. (B) Silicon master fabrication. (B, i) Silicon substrate. (B, ii) First the bacterial side-pockets are defined using e-beam lithography. (B, iii) The flow channel is defined next using photolithography. (B, iv) The final silicon mold. Three-step PDMS chip construction. (C, i) A positive-relief PDMS template is molded from the silicon master. (C, ii) The PDMS template is used to emboss the PDMS chip. (C, iii) The PDMS chip is bonded to a microscope coverslip to complete the device. (D) Image of the PDMS "mother-machine" microfluidic chip with entrance/exit and flow channel labeled. Note the chip is bonded to a glass coverslip. Tubing is inserted into the entrance and exit holes to bring and remove culture media. (E) Example of the mother-machine design with cells growing in single file within the side-pockets. The dashed white lines shows the side-pockets edges. When fresh culture media is flowed through the flow channel, the device can keep cells alive for days. Scale bar is 5μm. I acknowledge the work of a former lab member Clayton Greer for the contribution of schematics.

pattern defined by the e-beam mask to the silicon (Figure 10C, ii). The larger flow channels are constructed by photolithography as opposed to e-beam lithography followed by a similar reactive ion etching process (Figure 10C, iii). Following the removal of the photo-resist (SU8), the silicon chip is ready to pattern PDMS (Figure 10C, iv). A positive-relief PDMS template is patterned from the silicon master (Figure 10D, i). The positive-relief PDMS template is then used to emboss the negative-relief PDMS chip (Figure 10D, ii). Lastly, the negative-relief PDMS chip is bonded to microscope coverslip, which serves as the floor (or base) of the PDMS chip (Figure 10D, iii). An example of the finished product, the PDMS chip with cells in it is shown in (Figure 10E).

A detailed understand of the remaining sections of chapter 1 is not necessary to follow the results presented in chapters 2, 3, and 4, or the implications of these results. Nevertheless, strain construction is an integral component of this work. Ideally, this information will convey an accurate but general understanding of how we construct bacterial strains.

Bacterial strain construction

Once a protein of interest has been identified, bacterial strain construction usually involves the fusion of that protein to a fluorescent protein (FFP). Fusion proteins, also known as chimeric proteins, are constructed by removing the upstream gene's stop codon and splicing it together with the downstream gene. Translation of the connected genes produces a continuous polypeptide chain that allows each constituent protein to fold and function independently. Unstructured linker peptides are introduced between the protein of interest and the fluorescent protein to increase the likelihood that each protein will fold independently, and therefore retain their native functions. Moreover, antibiotic resistance genes are included near the fluorescent protein but are not a component of the FFP. The antibiotic resistance gene codes for a protein capable of allowing the bacteria to survive in the presence of a specific antibiotic. Only bacteria that have successfully incorporated the antibiotic resistance gene can survive the antibiotic

treatment. Accordingly, antibiotic resistance confers selectivity to cells that have incorporated the FFP gene.

λ Red Recombination

In all organisms, the fundamental principle behind most genetic manipulation techniques is homologous recombination (homologous recombination, see Appendix Glossary). A specific strategy commonly used to achieve these genetic manipulations in *E. coli* follows the Datsenko and Wanner method (Datsenko and Wanner 2000), which incorporates linear segments of DNA into the bacterial chromosome using proteins from the λ Red bacterial virus.

First, Polymerase Chain Reaction (PCR, see Appendix Glossary) is used to join a short segment of synthesized DNA (called primers), to each end of the exogenous DNA containing the FFP and antibiotic resistance genes (Figure 11A). Primers are designed to share approximately 30 nucleotides of homology with the chromosomal DNA in the bacterium located at either end of the target gene, and that gene's neighboring DNA (the location where the exogenous construct is to be inserted in the chromosome). The combined FFP and antibiotic resistance genes with homology extensions would be degraded quickly by exonucleases if released into the bacterial cytoplasm instead of recombining with the bacterial DNA as desired. Incorporation of the FFP and antibiotic resistance genes into the bacterial chromosome (recombination) is accomplished by the bacteriophage (a bacterial virus) λ Red recombinase proteins that block the bacteria's natural degradation of linear DNA. The λ Red recombination system is contained in a specially designed plasmid (plasmid, see Appendix Glossary), pKD46, that allows the λ Red recombinase proteins to be synthesized only in the presence of the sugar arabinose. The fusion protein can be engineered to include the full sequence of both original proteins, or only a portion of the protein of interest. Often, as in the case of strains MB13 and MB17 (See Appendix List of strains), we fuse a fluorescent protein with a mutated version of the protein of interest to observe the effects of the mutation, or to test the particular functionality of the protein of interest.

Frequently, bacterial strain construction requires the deletion of one or more genes from the chromosome. Only one gene can be deleted at a time, however. Typically, a gene of interest (e.g. gene B in Figure 11B) is replaced with antibiotic resistance gene. The same strategy used to construct a FFP can be used to delete a gene (Datsenko and Wanner 2000). As with the FFP insertion, the replacement of the gene of interest with the antibiotic resistance gene is verified first by the strain's ability to grow in the presence of the antibiotic, but secondly by colony PCR followed by gel electrophoresis (gel electrophoresis, see Appendix Glossary) (Figure 12).

If another genetic modification requiring selection by an antibiotic marker is needed, either an antibiotic resistance gene for a different antibiotic must be used, or the existing resistance gene must be removed. To remove the resistance gene, sequences called FRT (for FLP recognition target) are inserted on both sides of the antibiotic resistance gene (Figure 11A). An additional plasmid encoding an FLP recombinase protein acts on both FRT sequence repeats and removes the genetic material between FRT sites, as well as one of the FRT sequences. Left behind is one FRT sequence in the place where previously antibiotic resistance was located. This method can be used to remove any gene, or DNA region between FRT sites (Cherepanov and Wackernagel 1995).

P1 transduction

In a typical experiment, tens of strains may need to be constructed. Instead of recreating the genetic fusions or gene replacements each time, constructs already integrated into chromosomal DNA in one strain can be moved conveniently to another *E. coli* strain through a process called P1 transduction. P1 is another bacteriophage which upon infection of a bacterium can package, in addition to its own genome, pieces of foreign, bacterial DNA into its capsid. If this phage is used to infect another bacterium, referred to as the recipient or recipient strain, the phage can incorporate DNA pieces from the original chromosome, which can homologously recombine with the recipient bacterium's chromosome (Thomason, Costantino et al. 2001). As

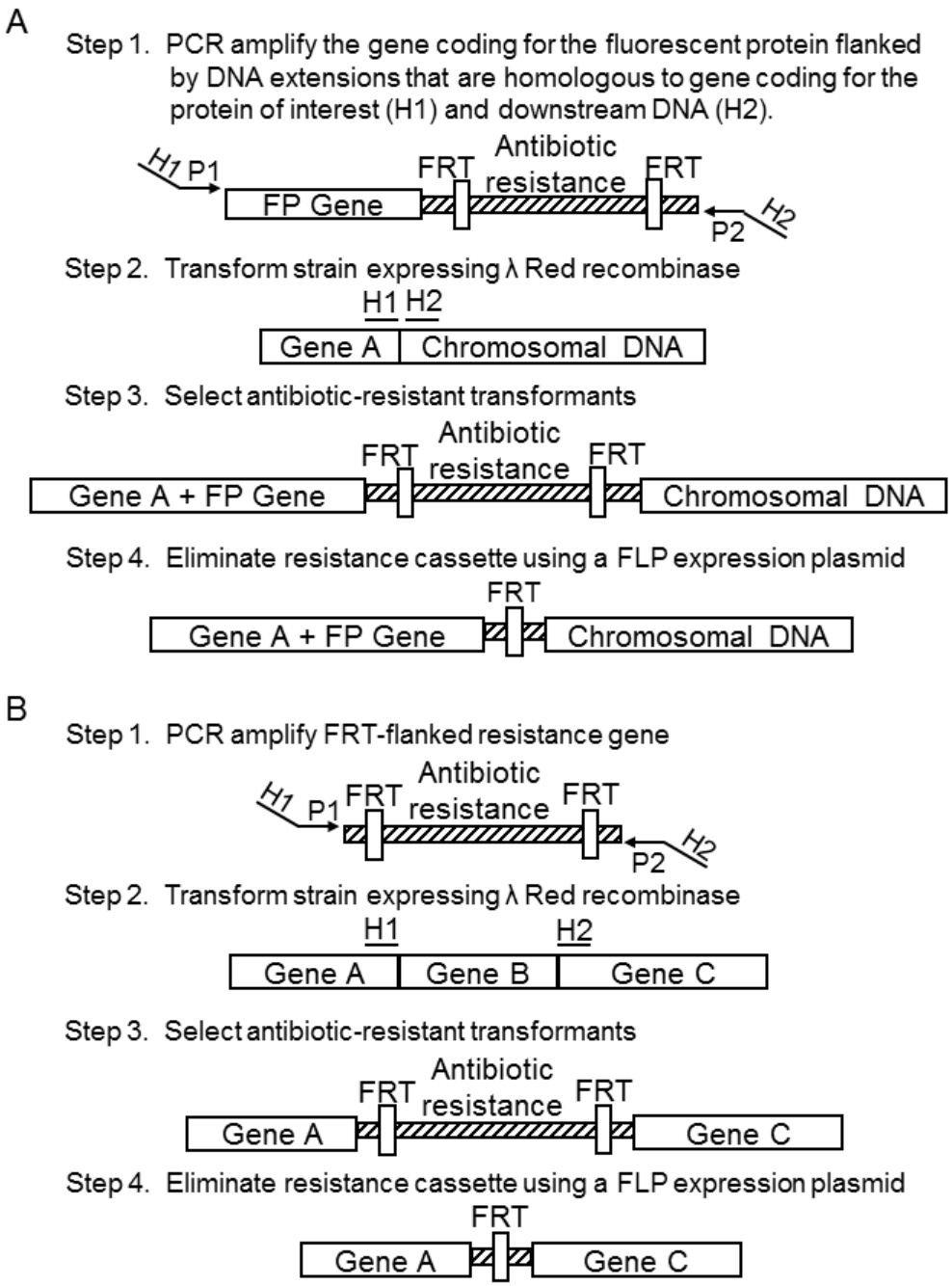

Figure 11. Genetic manipulation strategy. (A) Strategy for constructing a fluorescent fusion protein (FFP) between a fluorescent protein and a protein of interest, using antibiotic resistance for selectivity. H1 and H2 refer to the homology extensions or regions. P1 and P2 refer to priming sites. (B) Datsenko and Wanner's strategy for performing a gene deletion, or replacement of a gene of interest with an antibiotic resistance gene, which serves as a selectivity marker (Datsenko and Wanner 2000).

might be anticipated, the transduction of any gene from a donor to a host bacteria occurs infrequently. Consequently, selection is required. Luckily, the P1 phage is capable of transferring fragments as large as 100kb from one bacterium to another. The 100kb size limit is more than enough to permit the phage to transduce the FFP + antibiotic resistance gene. Selection of the bacterium that integrated the gene of interest, or gene replacement, from the donor to the recipient strain is performed by growing the transduced bacteria on a medium containing the particular antibiotic specified by the resistance gene. The majority of the bacterial strains in this work were produced using P1 transduction. Strains containing FFPs, gene replacements with antibiotic resistance, and other modifications of interest were first acquired from other researchers, or from the Yale Stock Center (http://cgsc.biology.yale.edu/). Subsequently, the P1 phage was used to infect those bacteria to make a solution containing phage particles capable of infecting a recipient strain, and transferring the gene of interest. This phage solution is called a P1 lysate.

When multiple genes are deleted from *E. coli*, growth can be severely limited, even when those genes, individually, are non-essential. Consequently, the standard P1 transduction procedure required modification when our molecular biology collaborators encountered difficulty transducing fluorescent proteins into the Δ*slmA* Δ*min* background. Part of the contribution of this work was the modification of the standard P1 transduction protocol (a procedure from the mid-1950s) (Thomason, Costantino et al. 2001) to include cells that were not capable of dividing in nutrient rich media. The P1 transduction protocol, and the modification made as part of this work, are given in the Appendix.

Verifying genetic modifications and checking for any negative effects of FFPs

Most fluorescent proteins are composed of approximately a couple hundred amino acids (aa), whereas the protein of interest may be less than 100aa. Whether or not the protein of interest is larger or smaller than the fluorescent protein, producing a FFP is no small modification

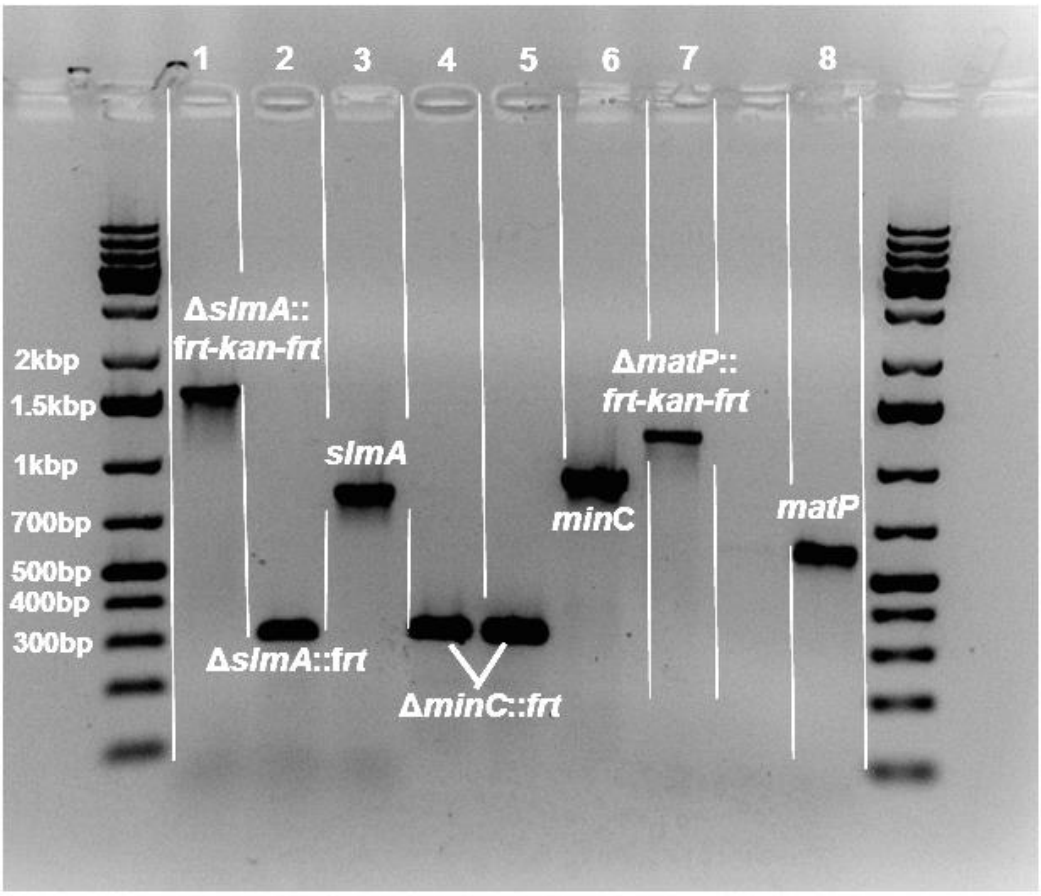

Figure 12. Verifying gene incorporation and gene deletion. Following PCR of a gene of interest (Polymerase Chain Reaction, see Appendix Glossary), and gel electrophoresis (gel electrophoresis, see Appendix Glossary), the gel is imaged under UV exposure. The dark bands are DNA sequences of differing length. The length of the DNA can be measure relative to a DNA "ladder," or a series of DNA pieces of known length. The DNA ladder is shown in the lane just to the left lane 1, and just to the right of lane 8. The lengths of relevant pieces are written beside the ladder band. As an example, the first lane contains DNA from a cell in which the *slmA* gene was replaced with the *frt-kan-frt* sequence. The length of both *frt-kan-frt* and the *slmA* gene (shown in lane 3) are known. Accordingly, the lengths as determined from the gel, can be compared to the known lengths to determine if the genetic modification resulted a genetic fragment of the desired length. The method cannot be used to determine the actual gene sequences, however, only the number of base pairs of the gene of interest. In lane 2, both the antibiotic resistance gene (*kan*) and *slmA* have been removed. The result is a small, ~300bp sequence (a single frt sequence) of leftover or "scar" DNA. Lanes 4 and 5 contain this same *frt* scar sequence following removal of the *minC* gene, shown in lane 6. Similarly, lane 7 shows the result of replacing the *matP* protein with the *frt-kan-frt* kanamycin resistance gene, and lane 8 shows the length of the native *matP* gene. In this example, all the genetic modification are as expected.

to the original protein. Consequently, it must be checked that the fluorescent modification doesn't significantly influence the protein of interest's native function. Equally as important are the biological consequences of the overexpression of the FFP. For all strains constructed which include a FFP, first the correct DNA sequence is verified. This can be realized in several ways, however we typically use colony PCR to amplify the gene fusion followed by gel electrophoresis (Figure 12). If the sequence length is correct, the strain is fluorescently imaged. If the FFP is fluorescent, the localization of the protein is observed, and compared against either the protein's known localization, or against its anticipated localization. While the expression level of a protein can be approximated by Western Blotting, in all strains constructed here, no Western Blotting was performed. Instead, fluorescent images of cells were scrutinized for inclusion bodies (FFP protein aggregates), which would indicate elevated levels of protein expression among other issues related to the proper folding of the FFP. Often elevated expression of FFPs leads to an overall increase in cell lengths, or to slower doubling times relative to wild-type *E. coli*. In most of the strains we use, the FFP protein replaces the native gene coding for the protein of interest, allowing the FFP to be produced at the native expression levels. Additionally, overall morphological peculiarities reflect either non-biological expression levels, or the compromised function of the native protein.

Bacterial growth

All strains used in this study were derivatives of E. coli K-12 (Bachmann 1972), into which the genetic modifications were made. Descriptions of all strains and plasmids are given in Table 5 (Appendix). The most used antibiotic resistance genes confer resistance to the antibiotics kanamycin (kan), ampicillin (amp), and chloramphenicol (cm). Antibiotic resistance can be incorporated either into the chromosomal DNA, or into plasmid DNA. Unlike chromosomal DNA, if the antibiotic resistance is incorporated into a plasmid, cells must be grown in the presence of

the antibiotic or else bacteria lose the plasmid. During bacterial growth, one or more of these antibiotics are added directly to the growth media.

All bacteria used in this work were grown in either nutrient rich media, or in one of two types of nutrient poor media. Lysogeny broth (LB) (Bertani 2004) provides a nutrient rich environment supporting optimal bacterial growth. The two nutrient poor media used, which result in slower cell growth, are made from supplementing M9 salts with magnesium sulfate and either 0.5% glucose or 0.3% glycerol. Both LB and M9 media are commercially available from Fisher Science and Sigma-Aldrich. All bacteria were grown and imaged at 28°C.

Often, it is desirable to grow long cells that contain multiple nucleoid. To achieve this, we incubate the strain with 20μg/mL cephalexin for approximately 2 hours. Cephalexin is another antibiotic that inhibits the divisome protein FtsI, which is responsible for lateral cell wall synthesis and therefore cell constrictions (Pogliano, Pogliano et al. 1997). For cells which lack a DNA label, 4',6-diamidino-2-phenylindole (DAPI), a fluorescent compound which diffuses through the cell membrane and binds strongly to DNA, is used to fluorescently stain the nucleoid. DAPI was added directly to liquid cultures at a concentration of 0.2μg/mL for 20-30 minutes prior to imaging. To control the expression of some FFPs, often FFP genes are placed under the control of the lac operator (a segment of DNA which regulates expression of the downstream gene(s)). In the case of the lac operator, the presence of lactose initiates transcription of a group of genes which code for proteins that allow the cell to metabolize the sugar lactose. Instead of controlling the expression of the lactose-metabolizing genes, the lac promoter can be hijacked to control the expression FFPs instead. A common lactose mimic is the compound isopropyl β-D-1-thiogalactopyranoside (IPTG), which in our case triggers transcription expression of ZipA-GFP, used to label the Z-ring. IPTG is used in place of lactose because IPTG is non-hydrolyzable, meaning its concentration remains constant throughout the experiment. For most strains, 40-100μM IPTG was added directly to the liquid culture approximately 2 hours prior to imaging.

Cells were imaged on M9 agarose pads for still imaging. For time lapse imaging, home-made glass bottom dishes were used (cf. Figure 8C). Cells were pipetted onto number 1.5 glass coverslips on the bottom of the dish and covered with about a 1 cm thick slab of M9 agarose. No antibiotics were used in M9 agarose during imaging. Agar was supplemented with IPTG (10-40 µM) for strains with ZipA-GFP constructs.

Chapter 2: The Z-ring colocalizes with the Ter macrodomain through a linkage involving MatP, ZapB, and ZapA proteins – Evidence for a new division protein positioning system

Cell division in Δ*slmA* Δ*min E. coli* had not been characterized before this work began. We hypothesized that if SlmA-mediated nucleoid occlusion and the Min system were the only two positioning systems in *E. coli* then the division planes in these double mutant cells should be randomly localized. On the other hand, if the VENO mechanism played a prevalent role in positioning the division proteins in these cells, one would expect division planes to form near midcell in the inter-nucleoid space between separated nucleoids or near the cell poles. If the Z-ring formed in the space between two segregating nucleoids, cell division should lead to two daughter cells that inherited complete genomes, and are therefore viable.

When we considered the placement of Z-rings relative to nucleoids Δ*slmA* Δ*min E. coli* in fast-growing LB medium, which produces cells which grow long (~50μm or longer) but fail to divide, we found many Z-rings that localized at regions where the corresponding nucleoid density was low (in the middle of two nucleoids or at the center of segregating nucleoids), or at the poles. This observation supported the VENO hypothesis. However, against our expectations, when the same Δ*slmA* Δ*min E. coli* were grown in a nutrient poor environment, which support cell division and therefore viability, Z-rings preferentially formed over the centers of nucleoids even if those nucleoid displayed no apparent segregation. In longer cells containing multiple nucleoids, Z-rings preferentially formed over nucleoids instead of at the space between nucleoids. Further experiments revealed that the nucleoid-centric Z-ring localization arose because of a protein-mediated linkage to the replication terminus region of the chromosome. We identify three known proteins in this linkage, ZapA, ZapB, and MatP (though it is possible more are involved). When either protein is removed, the Z-ring no longer colocalizes with the nucleoid-centric replication

terminus domain. Interestingly, to our knowledge, this linkage is the only known mechanism to promote Z-ring positioning in *E. coli*.

Z-rings localize at all nucleoid free areas in fast growth conditions as expected by VENO positioning

To test the VENO hypothesis, we determined the placement of the Z-ring relative to the nucleoid and cell centers using the Δ*slmA* Δ*min* double mutant *E. coli* containing a fluorescently labeled ZipA-GFP (TB86 λCH151) and FtsZ-GFP (TB86 λDR120) (Bernhardt and de Boer 2005). In these measurements, the nucleoid was stained with DAPI, which binds strongly to DNA and is fluorescent under UV exposure. As a reference, the wild-type strain with the same labeling was also imaged. We found Δ*slmA* Δ*min* cells to have a large number of rings, arcs, and patch-like accumulations of ZipA-GFP on their plasma membranes, some of which appeared as if overlapping nucleoids (Figure 13A, C). However, when we plotted fluorescence intensity line profiles from ZipA-GFP and DAPI (Figure 13B, D), we observed that essentially all accumulations of ZipA-GFP corresponded to local minima of the chromosomal distribution, in agreement with the phenomenological description of nucleoid occlusion predicted by the VENO mechanism (Figure 5). In addition to the minima of the chromosomal distribution, ZipA-GFP also accumulated abundantly at cell poles. Unfortunately, because Δ*slmA* Δ*min* cells grown in LB cannot divide, we could not test how accurately cells divide with respect to the cell center, or more generally gauge cell viability as a result of this Z-ring positioning system.

Δ*slmA* Δ*min* cells divide at well-defined locations relative to cell poles

To quantify the accuracy of division plane placement in Δ*slmA* Δ*min* E. coli, cells were grown in nutrient poor M9 medium. We determined the relative volume fractions of two daughter cells that still adhered together by their poles after division following a method introduced by (Männik, Wu et al. 2012), and compiled these ratios into a histogram for a population of cells

(Figure 14). The digital image analysis procedure closely follows the cell segmentation procedure described in the Quantitative Image Analysis Section of Chapter 2. To find this volume ratio, or equivalently the cell division ratio, we followed individual bacteria expressing a cytosolic GFP protein in time lapse movies until the cell-segmentation algorithm was able to separate one newly emerging daughter cell from the other. For the two new cells, the summed pixel intensities inside the contours $I^{\Sigma}_{daughter\,1}$ and $I^{\Sigma}_{daughter\,2}$ were calculated, followed by subtraction of the background. We define the division ratio as:

$$\text{Division ratio} \equiv I^{\Sigma}_{daughter\,1}/(I^{\Sigma}_{daughter\,1} + I^{\Sigma}_{daughter\,2})$$

Considering that the density of the cytosolic GFP is the same in both daughter cells right after division, it follows that the division ratio of the intensities equals the division ratio for the volumes.

In this experiment, equal daughter cell volumes implies the mother cell positioned its division proteins accurately. As a reference for cell division accuracy, we determined the volume fraction distributions for the wild-type *E. coli* (strain BW25113) (Figure 14A). To compare the division ratios of Δ*slmA* Δ*min* to cells which are known to divide at locations other than midcell, we also performed the same analysis on strain JW1165 which contains a *minC* deletion (Figure 14B). Cells with a deletion of any of the Min proteins often produce very small anucleate (anucleate, see Appendix Glossary) mini cells due to cell division at a pole. As expected, the distribution of volume fractions for the wild-type strain consisted of a pronounced single peak at a value of 1/2, showing that upon division, the volume of each daughter cell is approximately equal. Note that all histograms are symmetric relative to 1/2 because both daughter cells are counted in these histograms. Also as expected, the distribution of volume fractions for the Δ*minC* strain showed in addition to the main peak at 1/2, distinct peaks at 1/4, 1/3, 2/3 and 3/4 values as well as broad peaks on the tails of the volume fraction histogram which indicated polar, minicelling divisions. Remarkably, the 1/4, 1/3, 2/3, 3/4 peaks arose because of underlying nucleoid structure. Peaks at 1/4 and 3/4 values correspond to divisions where a mother cell distributes one of its

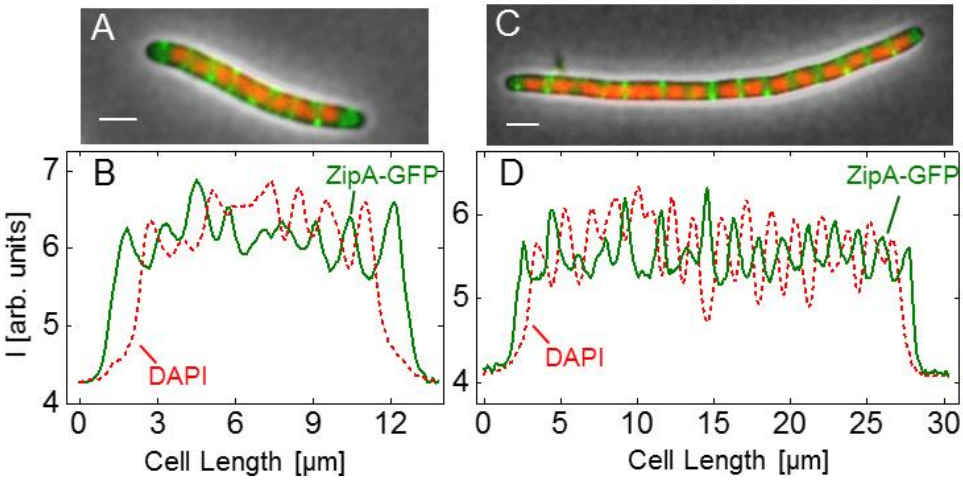

Figure 13. Positioning of Z-rings relative to nucleoids in Δ*slmA* Δ*minC* *E. coli* grown in nutrient rich LB medium. (A) A composite of ZipA-GFP (green), DAPI stained nucleoid (red) and phase contrast images (grey) of a Δ*slmA* Δ*min* cell grown in LB. (B) The intensity line profiles of each image plane along the long axis of the cell for the cell shown in panel A. (C), (D) The same composite image and line profiles for a longer LB-grown Δ*slmA* Δ*min* cell. Scale bars are 2μm.

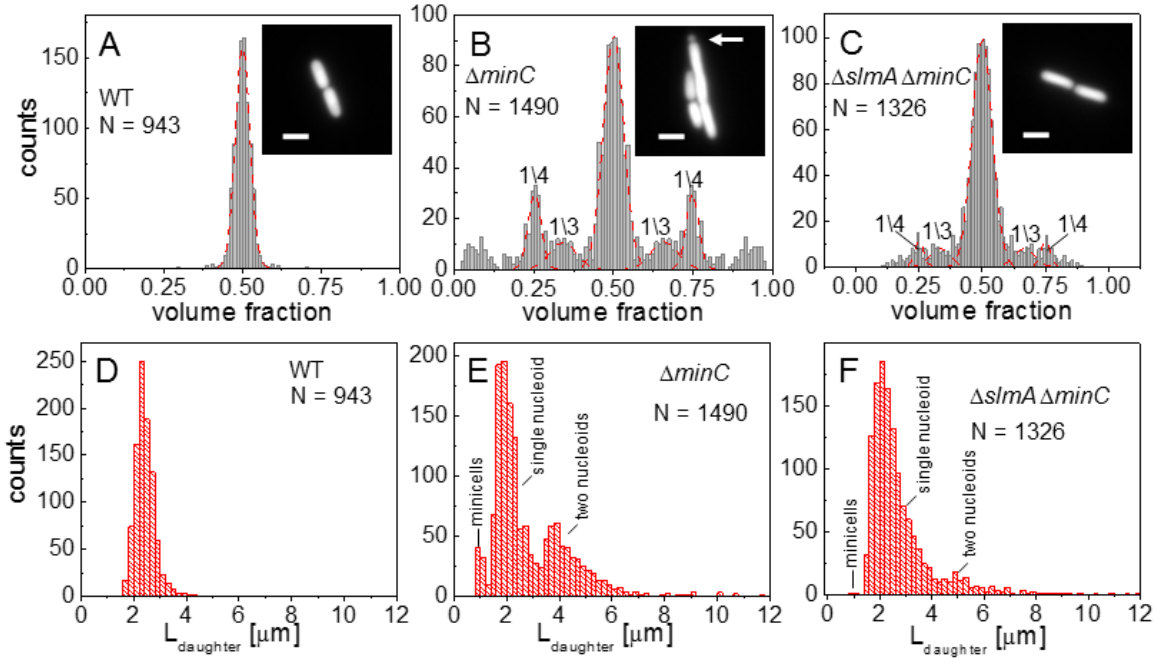

Figure 14. Relative volume fractions and length distribution of daughter cells after division. (A) Wild type (BW25113), (B) Δ*minC* (JW1165), (C) Δ*slmA* Δ*minC* (PB194) strains. Volume fractions are calculated as the ratio of one daughter cell's volume to the sum of both daughters' volumes. Red dashed lines in the histogram show fittings of different peaks with a Gaussian function. The centers of fitting lines are fixed to 1/4, 1/3, 1/2, 2/3 and 3/4 values. The insets in the histograms show fluorescent images of cells from the respective strains. The arrow in the inset of panel (B) points to a minicelling division. (D) – (F) Length distributions for corresponding cells shown in (A) – (C). All scale bars correspond to 2 μm.

nucleoids to one daughter cell and three to the other. Smaller peaks at 1/3 and 2/3 values correspond to division of cells with three nucleoids.

The volume fraction distribution for the Δ*slmA* Δ*minC* strain (PB194) showed, qualitatively similar to the ∆*minC* strain, distinct peaks at 1/2, 1/4 and 3/4 positions with discernible peaks also at 1/3 and 2/3 values (Figure 14C). Gaussian fits to the peaks in the histogram showed that the majority of Δ*slmA* Δ*minC* cells divide at about midcell (75%) while 6.5% divided approximately at the quarter position, and 14% between the quarter and half-cell length from one of the poles. Interestingly, the frequency of central divisions for the Δ*slmA* Δ*minC* strain was higher than for the strain having only a *minC* deletion (50%) while the frequency of Δ*minC* cells dividing at a quarter (20%) and a third of the cell length from the poles (16%) was higher compared to the Δ*slmA* Δ*minC* strain. Additionally, the double mutant strain produced essentially no minicells (0.2% of total divisions), although they were noticeably present in the *minC* deletion strain (7% of total divisions).

The presence of peaks at the 1/2, 1/4, and 3/4 positions indicates that, despite a lack of nucleoid occlusion factor SlmA in the double mutant strain, there remains a high level of coordination between nucleoids and the Z-rings in *E. coli* cells, which would be expected if VENO influenced Z-ring positioning. Comparison between Δ*minC* Δ*slmA* double mutants and Δ*minC* single mutant strains demonstrates that removal of SlmA suppresses minicell production and biases cell division towards the cell center. While VENO would predict central cell divisions, VENO does not explain why there were so few minicell divisions in the Δ*slmA* Δ*minC* cells.

The cell division plane shifts from midcell to quarter-cell with increasing cell length

We hypothesized that because these 1/3 and 1/4 divisions contained more nucleoids than wild-type cells, these quarter and third divisions should occur in cells that are longer than wild-type cells. If true, perhaps an unknown event diverted cell division from the central division site

and cells continued to grow until division could later occur. Characterizing the division ratio as a function of cell length could then help us identify the origins of the event.

As expected, the length of the double mutant cells immediately following division, 2.83±1.54 μm, was 18% longer than that of the BW25113 wild-type strain, 2.41±0.36 μm (Figure 14D-F). The main factor contributing to the length difference was long cells making up about 10% of the Δ*slmA* Δ*minC* population, whose lengths were about twice that of the majority of the population. Interestingly, these longer double mutant cells divided with higher prevalence at 1/4 and 3/4 positions compared to shorter cells. To quantify this tendency, we plotted the frequency of central divisions and the frequency of divisions at the quarter cell length from the poles as a function of mother cell length (Figure 15). In this analysis, central divisions were considered to be all divisions in which volume fractions were within 0.50±0.10. The divisions at quarter cell positions were considered when the corresponding volume fraction ratios were within 0.25±0.05. For the Δ*slmA* Δ*minC* cells, the frequency of cell divisions at the quarter cell length from the poles increased considerably as the cells reached a length of about 6 μm (Figure 15A). About 50% of cells longer than 6 μm preferentially divided at the quarter-cell length from the poles, while a smaller fraction, about 25% of cells, divided at the cell center. The data for the Δ*minC* cells showed a very similar sharp transition of the cell division plane from the center to the quarter locations as the cell length reached about 5.2 μm (Figure 15B). A marked increase in the frequency of 1/4 divisions indicates that some positional signal guides the cell division plane from midcell to its quarter positions as the cells reach a relatively well-defined length.

Z-rings localize to nucleoid centers in slow growth conditions which contradicts Z-ring positioning by VENO

To probe the origins of the signal that directs Z-rings to quarter and third cell locations in Δ*slmA* Δ*min E. coli*, we observed the localization of the ZipA-GFP labeled Z-ring with the DAPI-

stained nucleoid. While in Δ*slmA* Δ*min* cells in fast growth conditions the Z-rings accumulate in essentially all nucleoid-free areas, a very different localization pattern was observed when cells were grown in the nutrient poor M9 medium. Representative cell images are shown in Figure 16.

In a few cells, we noticed that the nucleoids were displaced noticeably from the cell center. Though one would expect VENO would tend to position the Z-ring on the side of cell opposite to the direction in which the nucleoid was displaced (where there was more nucleoid-free space), the Z-rings instead followed the centers of the nucleoids. To quantify the tendency of the Z-ring to localize over the nucleoid center, we measured the distance between the Z-ring and cell center, ΔX_z, as a function of the distance between the nucleoid center and the cell center, ΔX_n, for all cells in a population of isolated cells having a single nucleoid (Figure 17A) using line profiles generated from Cload. To quantify the extent of co-localization between the nucleoid center and the Z-ring, we determined the standard deviations of distances between the Z-rings and nucleoid centers, $\sigma_{X_Z - X_n}$, and between the Z-rings and cell centers $\sigma_{\Delta X_z}$. We separated the data into two distinct groups – polar Z-rings and centrally located ones. The precision of central Z-ring placement relative to nucleoid centers $\sigma_{X_Z - X_n}$ = 66nm (Figure 17B) was more than two times higher than the positioning of Z-rings relative to cell centers $\sigma_{\Delta X_z}$= 177nm in Δ*slmA* Δ*min* cells with ZipA-GFP label (Figure 18A). We found very similar co-localization characteristics for central Z-rings ($\sigma_{X_Z - X_n}$= 76nm, $\sigma_{\Delta X_z}$= 196nm) in FtsZ-GFP labeled Δ*slmA* Δ*min* cells (Figure 17H, 18B), confirming that the co-localization effect is not related to a specific Z-ring label. The collection of distribution statistics for all measured strains can be found in Table 1. Interestingly, for wild type cells (Figure 17D-F) co-localization between Z-rings and nucleoid centers ($\sigma_{X_Z - X_n}$= 81nm) was somewhat lower than in Δ*slmA* Δ*min* cells (Ansari-Bradley test p=0.35; F-test p = 0.017), while the precision of Z-ring placement in the vicinity of the cell centers ($\sigma_{\Delta X_z}$= 118nm) was significantly higher when compared to Δ*slmA* Δ*min* cells (Ansari-Bradley test $p=6\cdot10^{-5}$; F-test $p = 10^{-7}$). Similar

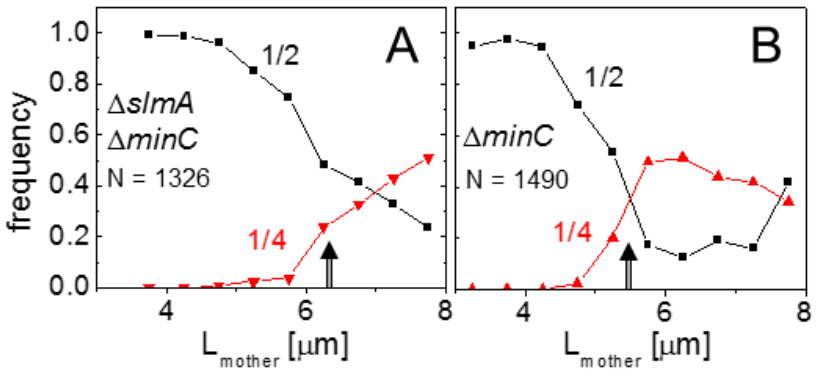

Figure 15. Division frequency at the 1/4 and 1/2 cell positions with respect to mother cell length. (A) Data for the Δ*slmA* Δ*minC* double mutant strain (PB194); (B) Δ*minC* strain (JW1165). Cell lengths are binned at 0.25μm intervals. Arrows point to transition regions from centrally occurring divisions to divisions at cell quarters. The lengths of the mother cells are measured just before cell division. Note that only a few cells from both strains are longer than 8μm, limiting analysis for longer cells.

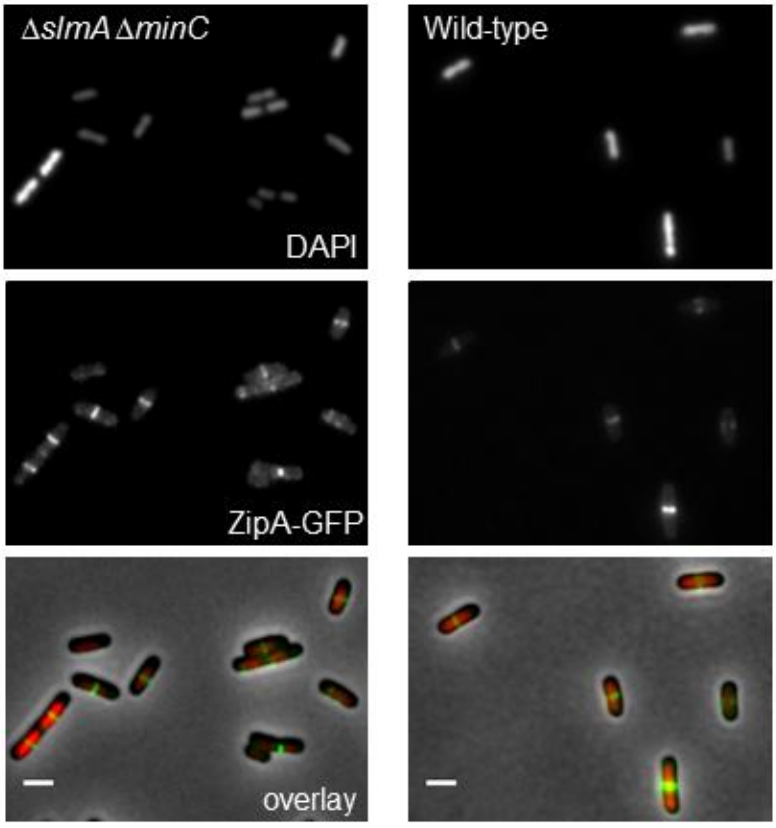

Figure 16. Fluorescent images of Δ*slmA* Δ*minC* *E. coli* grown in nutrient poor M9 media. Images of DAPI stained nucleoid and ZipA-GFP labelled Z-ring for *ΔslmA ΔminC* double mutant strain TB86 (left column) and wild-type strain JMBW5 (right column). In the bottom row, the two fluorescent images are overlaid with phase contrast image. The scale bars are 2μm.

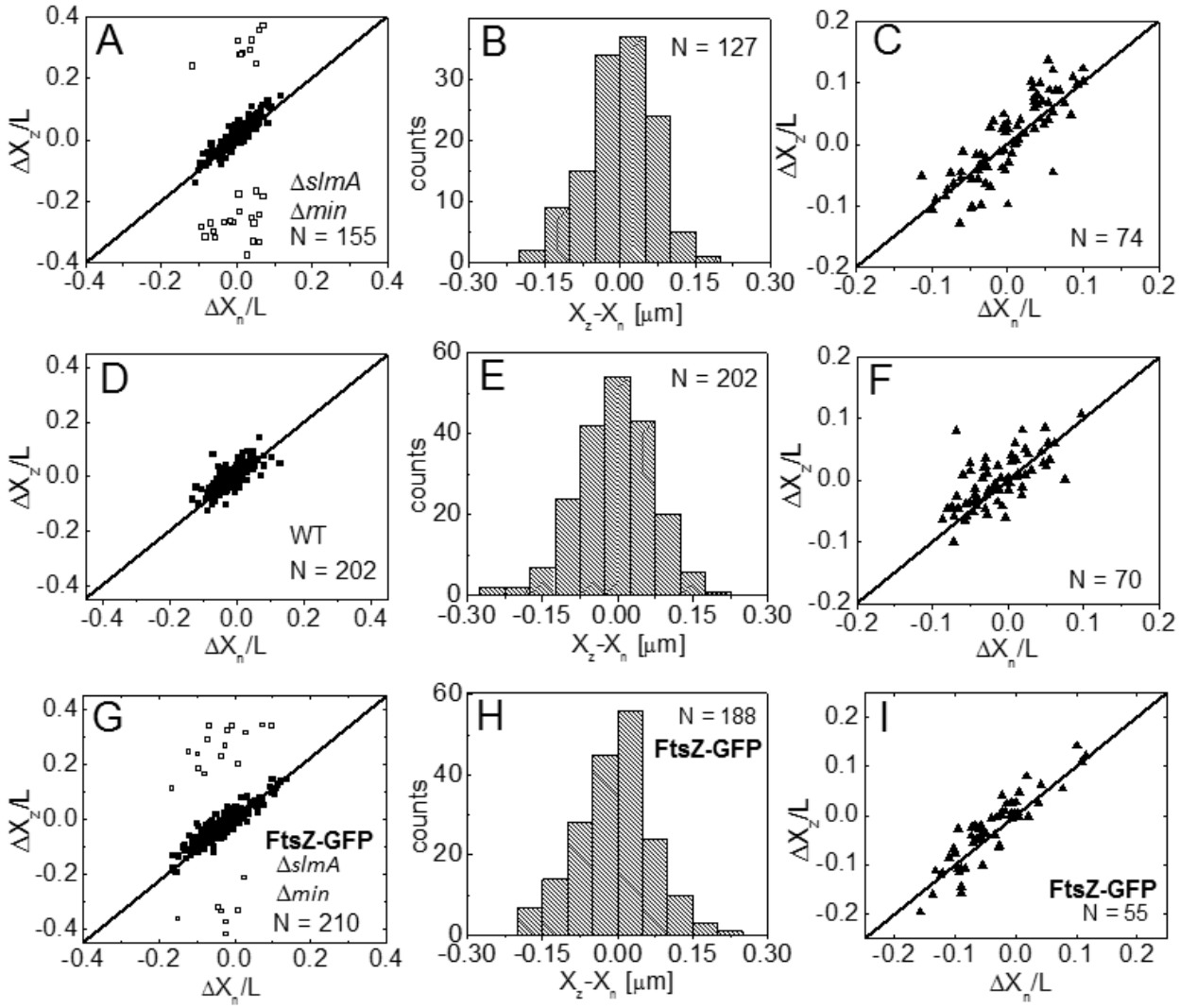

Figure 17. Localization of ZipA-GFP labeled Z-rings relative to cell center and the center of nucleoids. The displacement of the nucleoid relative to the cell center is ΔX_n, and the displacement of the ZipA-GFP labeled Z-ring is ΔX_z. (A) ΔX_z vs. ΔX_n for Δ*slmA* Δ*min* cells (strain TB86) scaled by cell length L. Solid rectangles mark central and open rectangles mark polar Z-rings. The solid line corresponds to $\Delta X_z=\Delta X_n$. (B) Corresponding distribution of distances between the Z-ring center and nucleoid center for the Δ*slmA* Δ*min* strain (data for central Z-rings are shown). (C) ΔX_z vs. ΔX_n for the same Δ*slmA* Δ*min* cells that show a Z-ring over a compact nucleoid. (D) – (F) Corresponding plots to (A) – (C) for wild-type *E. coli*. (G) – (I) Corresponding plots to (A) – (C) but for Δ*slmA* Δ*min E. coli* that have an FtsZ-GFP label instead of a ZipA-GFP label to observe the Z-ring (strain TB86 λDR120).

values of $\sigma_{X_Z - X_n}$ and $\sigma_{\Delta X_z}$ as in wild-type cells were found also for Δ*min* and Δ*slmA* single deletion strains (Figure 19; Table 1).

Co-localization of the Z-ring to nucleoid centers was present already in the early stages of chromosomal replication before a distinct bi-lobed morphology (characteristic of visible chromosome segregation which occurs later in the cell cycle) appeared in nucleoid images (Figure 17C, F, and I). To distinguish bi-lobed nucleoids from compact nucleoids, we inspected intensity line profiles taken over DAPI stained nucleoids. We considered a nucleoid to be compact if its DAPI intensity line profile near the nucleoid center lacked any discernable dips (e.g. DAPI profile in Figure 7G, H). In Δ*slmA* Δ*min* cells with a compact nucleoid, the level of co-localization between the nucleoid and the Z-ring, $\sigma_{X_Z - X_n}$= 74nm, was comparable to the value characterizing the whole cell population, $\sigma_{X_Z - X_n}$= 76nm (F-test, p=0.42; Ansari Bradley test p=0.83). Similar conclusion can be drawn also for the wild type cells where$\sigma_{X_Z - X_n}$= 88nm (F-test, p=0.36; Ansari Bradley test p=0.91) and for Δ*min* and Δ*slmA* single deletion strains (Figure 19E, F; Table 1). These comparisons indicate that nucleoid centers and Z-rings can co-localize in early stages of replication when the nucleoid morphology is compact both in wild type cells and in cells where one or both of the known Z-ring positioning systems have been removed. Importantly, whereas Z-ring formation over nucleoids containing significant nucleoid gaps would be consistent with positioning by VENO, Z-ring formation over compact nucleoids is not. This observation suggests that even *if* VENO is present within these cells, another localization mechanism provides a more dominant influence on Z-ring placement. Intriguingly, the preferred Z-ring position occurs *over* nucleoid centers and not away from nucleoids.

The bias in localization of the Z-rings to the centers of nucleoids was even more visually striking in longer Δ*slmA* Δ*min* cells that had two or more well-separated nucleoids (Figure 20A). We found a strong preference for the Z-ring to position over the centers of nucleoids as compared to regions between fully segregated nucleoids (Figure 20B). We refer to the former as

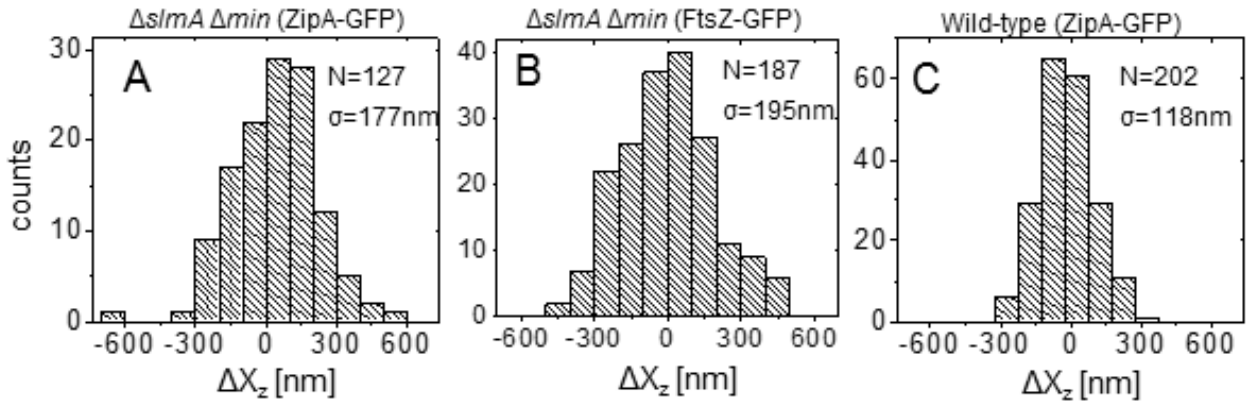

Figure 18. Displacements of Z-rings relative to the cell center, ΔX_z. (A) for Δ*slmA* Δ*min* (strain TB86 with ZipA-GFP labeled Z-ring), (B) Δ*slmA* Δ*min* (strain TB86Dr120 with FtsZ-GFP labeled Z-ring), and (C) parental strain (strain JMBW5 ZipA-GFP labeled Z-ring). Data are shown only for cells with a single nucleoid.

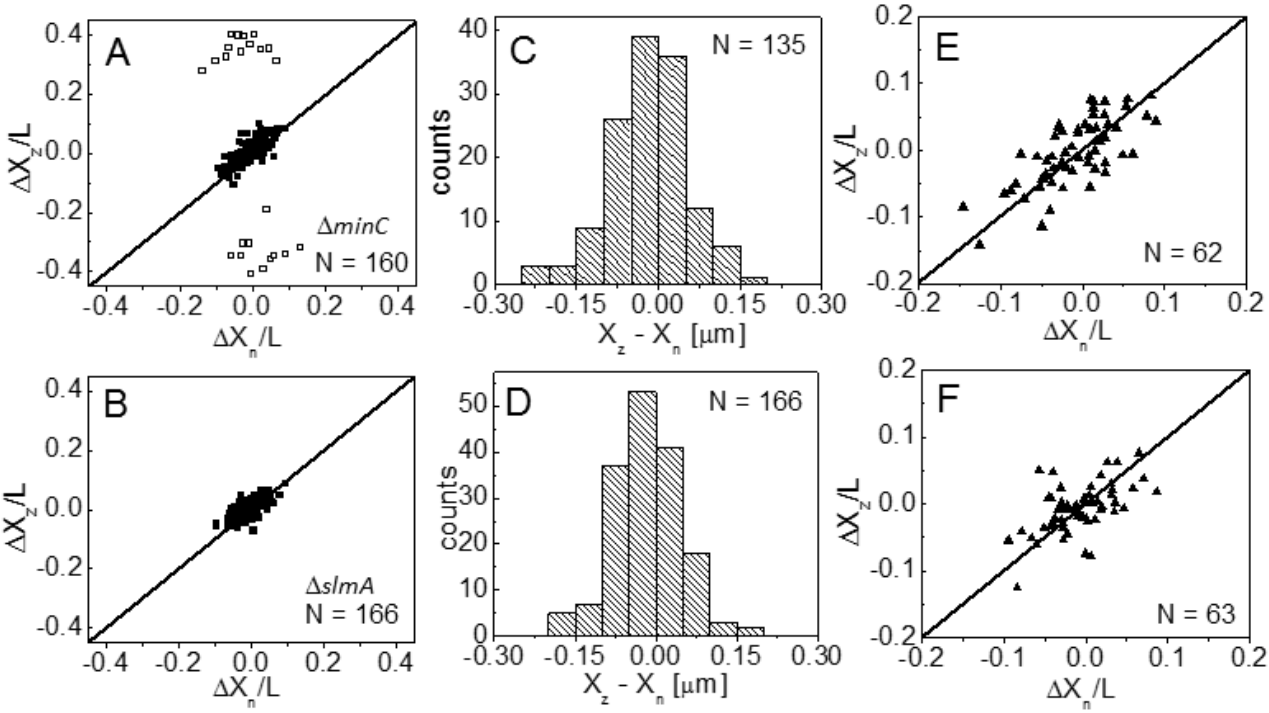

Figure 19. Localization of ZipA-GFP labeled Z-rings relative to cell center and the center of nucleoids for Δ*minC* (top row) and Δ*slmA* (bottom row) single deletion strains. (A), (B) ΔX_z vs. ΔX_n scaled by cell length L. Solid rectangles mark central and open rectangles mark polar Z-rings. The solid line corresponds to $\Delta X_z=\Delta X_n$. Data are shown only for cells with a single nucleoid. (C), (D) Distribution of distances between the Z-ring center and nucleoid center. Only data for central Z-rings are shown. (E), (F) ΔX_z vs. ΔX_n for cells that show a Z-ring over a compact nucleoid.

Table 1. Statistics describing co-localization of the Z-ring and the nucleoid center in different strains.

Strain Name	Genotype	N	$\sigma_{X_Z} - \sigma_{X_n}$ (nm)	$\sigma_{\Delta X_Z}$ (nm)	R^2
JMBW5 all	Wild type	202	81	118	0.51
JMBW5 compact nucleoid	Wild type	70	88	108	0.34
MB21 all	Δ*slmA*	166	63	78	0.54
MB21 compact nucleoid	Δ*slmA*	63	73	78	0.31
MB22 all	Δ*minC*	135	72	110	0.74
MB22 compact nucleoid	Δ*minC*	62	87	119	0.67
TB86 ZipA all	Δ*slmA* Δ*min*	127	66	177	0.84
TB86 ZipA compact nucleoid	Δ*slmA* Δ*min*	31	74	180	0.81
TB86 ZipA compact nucleoid	Δ*slmA* Δ*min*	74	95	178	0.84
TB86 FtsZ all	Δ*slmA* Δ*min*	188	76	196	0.84
TB86 FtsZ compact nucleoid	Δ*slmA* Δ*min*	55	81	195	0.82
MB10 all	Δ*slmA*Δ*min*Δ*matP*	123	151	200	0.40
MB10 compact nucleoid	Δ*slmA*Δ*min*Δ*matP*	50	230	230	0.04
MB4 all	Δ*slmA*Δ*min*Δ*zapB*	218	222	262	0.27
MB4 compact nucleoid	Δ*slmA*Δ*min*Δ*zapB*	51	344	352	0.11
MB11 all	Δ*slmA*Δ*min*Δ*zapA*	145	203	211	0.07
MB11 compact nucleoid	Δ*slmA*Δ*min*Δ*zapA*	50	280	275	0.01

R^2 is a dimensionless goodness of fit parameter for a model $\Delta X_n = \Delta X_z$. Note that for perfect co-localization of nucleoid and the Z-ring centers, R^2 approaches a value of one. R^2 can also be negative; for $R^2<0$ there is no meaningful evidence of co-localization in the data.

the new division sites (N) and the latter as the old division sites (O). The probability of finding a Z-ring over the center of nucleoids (N sites) was 98±1%, while the probability of finding a Z-ring in the inter-nucleoid space between fully segregated nucleoids (O sites) decreased to 59±8% (Figure 20C). Note that Z-rings can be present in both division sites at the same time. The tendency of the Z-rings to preferentially localize at 1/4 positions from the cell pole in longer cells, i.e. in new sites, is consistent with our earlier observation that in longer Δ*slmA* Δ*min* cells divisions occur preferentially at 1/4 positions from the cell pole (Figure 15). Taken together, the analysis of the placement of the Z-rings and nucleoid centers in multi-nucleoid Δ*slmA* Δ*min* cells further supports the hypothesis that a positional signal guides the Z-rings to the nucleoid centers, and not away from nucleoids as VENO predicts.

To determine if wild type cells would display the same behavior as multi-nucleoid Δ*slmA* Δ*min* cells we induced an elongated, multi-nucleoid cell morphology by treating cells with the antibiotic cephalexin. Cephalexin does not inhibit Z-ring assembly but prevents Z-ring constriction by inhibiting the downstream protein FtsI (PBP3). Interestingly, in elongated wild type cells the Z-rings appeared essentially only at midcell even when new sites were present (Figure 20D-F). Z-rings in cephalexin treated Δ*slmA* Δ*minC* cells still showed a preference to the new division sites as did their untreated counterparts (Figure 21A-C). We also analyzed Δ*slmA* and Δ*minC* single deletion cells after cephalexin treatment. Δ*slmA* cells behaved as wild type cells (Figure 21D-F) while Z-rings in the Δ*minC* cells showed a preference to the new division sites as in Δ*slmA* Δ*min* cells (Figure 21G-I). These comparisons show that the putative positioning signal only manifests itself when it is not conflicting the regulation due to the Min system. It is important to note that such conflict does not occur in wild type cells in normal growth conditions because in this case the nucleoid center and the concentration minimum for MinC coincide. As Figure 17D-F shows, the localization signal emanating from the nucleoid center is important in Z-ring localization in wild type cells under normal growth conditions, and apparently *ruling out* the VENO mechanism as

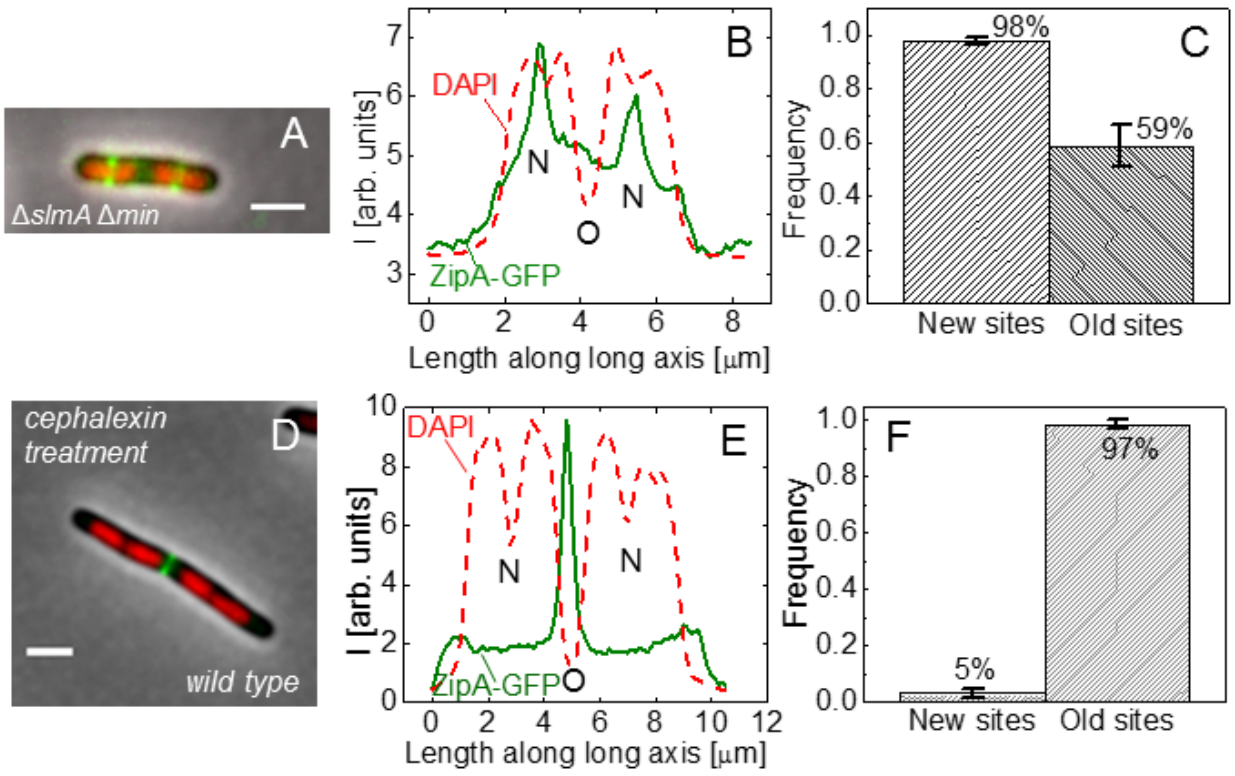

Figure 20. Positioning of Z-rings relative to nucleoids in multi-nucleoid cells. (A) A composite image of longer Δ*slmA* Δ*min* cell. ZipA-GFP (green), DAPI stained nucleoid (red), and phase contrast images (grey) have been overlaid. Scale bar is 2 μm. (B) Nucleoid and ZipA-GFP density distributions along the long axis of the cell for the cell shown in panel (A). The positions marked by "N" correspond to the new division sites at the centers of the nucleoids and the position marked by "O" to old division site between fully segregated nucleoids. (C) Frequency of Z-rings in the double mutant cells at the new and old replication sites. Only cells that have two or more distinct nucleoids have been analyzed. Error bars represent standard deviations over three independent measurements each involving about 50 cells. (D) – (F) the same for wild type cells that have been treated for 2 hours with 20 μg/ml cephalexin.

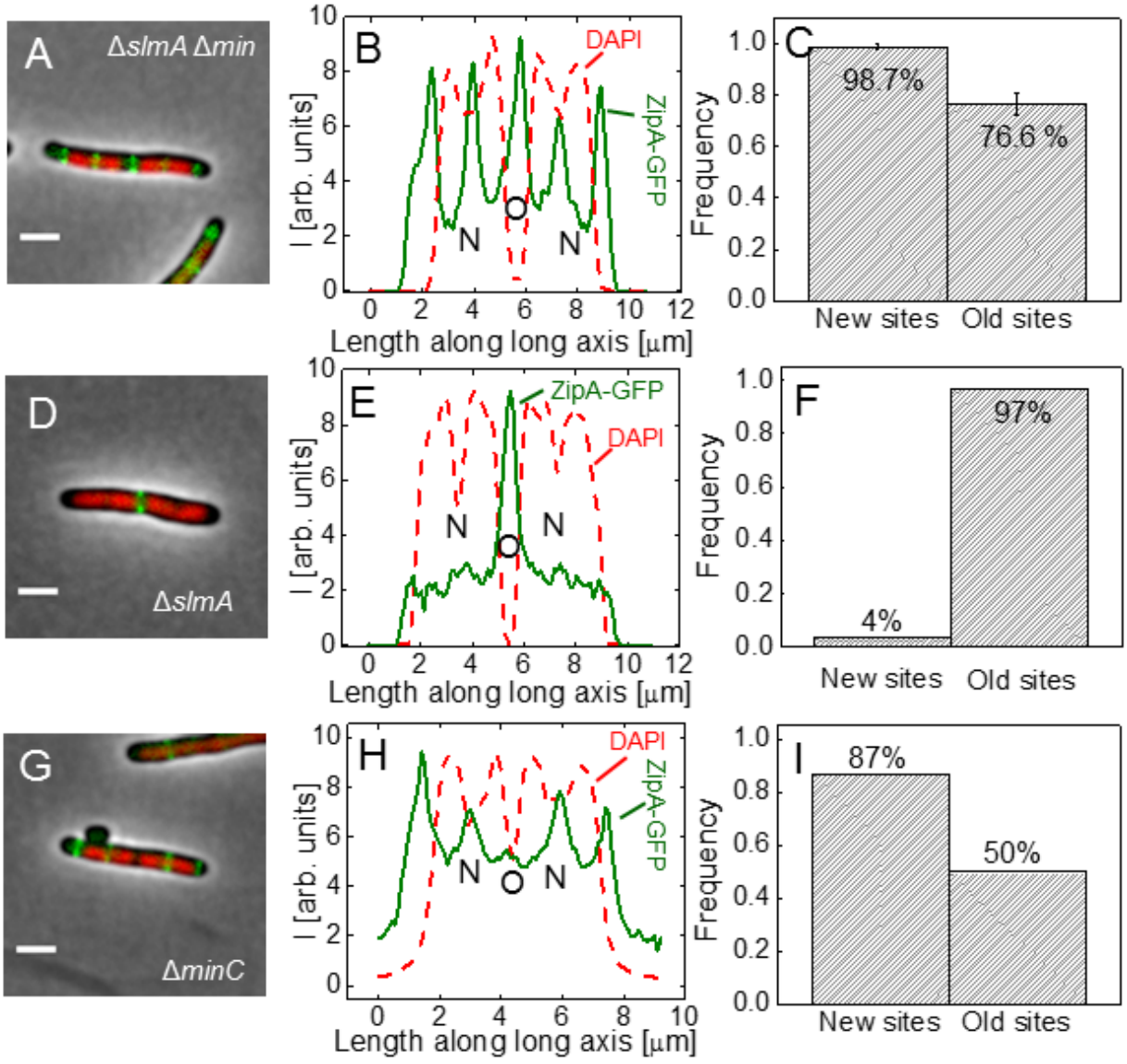

Figure 21. Positioning of Z-rings relative to nucleoids in Δ*slmA* Δ*min*, Δ*slmA*, and Δ*minC* single deletion strains following cephalexin treatment. (A), (D), (G) Composite images of cells after cephalexin treatment. ZipA-GFP (green), DAPI stained nucleoid (red), and phase contrast images (grey) have been overlaid. Scale bar is 2 μm. (B), (E), (H) Nucleoid and ZipA-GFP density distributions along the long axis of the cell for the cell shown in the adjacent left panel. The positions marked by "N" correspond to the new division sites at the centers of the nucleoids and the position marked by "O" to old division site between fully segregated nucleoids. (C), (F), (I) Frequency of Z-rings in the double mutant cells at the new and old replication sites. Only cells that have two or more distinct nucleoids have been analyzed.

the dominant Z-ring positioning mechanism in these cells.

Co-localization between the Ter macrodomain and the Z-ring

If the positional signal is not VENO then what is its underlying molecular basis? Clues to the origin of the signal responsible for colocalization of Z-rings with nucleoid centers came from how the nucleoid is organized. It has been argued that the *E. coli* chromosome is composed of six distinguishable regions. Four of the six regions are thought to be structured, and are referred to as macro-domains (Ori, Left, Right, and Ter) along two additional non-structured (NS) regions (NS-left and NS-right) (Valens, Penaud et al. 2004). Organization of the chromosome into these macrodomains is believed to impose restrictions on the permitted rearrangements to the linear-order sequence of the chromosome (Dorman 2013). Approximately at the time of Z-ring formation, the center of the nucleoid is known to be occupied by the Ter region of the chromosome (Wang, Possoz et al. 2005, Fisher, Bourniquel et al. 2013), which forms a well-defined unit – the Ter macrodomain (Niki, Yamaichi et al. 2000, Mercier, Petit et al. 2008). In *E. coli,* MatP is a dispensable protein that defines the Ter macrodomain by connecting 23 specific sites in a chromosomal region that spans about 800 kb (Mercier, Petit et al. 2008). Based on previous works (Wang, Possoz et al. 2005, Fisher, Bourniquel et al. 2013), it appeared plausible that the Z-rings might position over the Ter macrodomain. To investigate if this hypothesis was correct, we labeled the Ter region of the chromosome with a MatP-mCherry construct that was expressed from its endogenous *matP* locus and labeled the Z-ring with ZipA-GFP (Figure 22A–D). The measurements revealed a very strong correlation in the placement of the MatP-labeled Ter macrodomain and the Z-ring in Δ*slmA* Δ*min* cells (Figure 22E). Notably, the Z-ring co-localized with the MatP focus in all cases, even when the MatP focus was located at the nucleoid periphery close to the cell pole. In wild-type cells, correlations were also strongly present although in a few cases (4 out of 166) the Z-ring could be observed to localize at the center of the cell when the

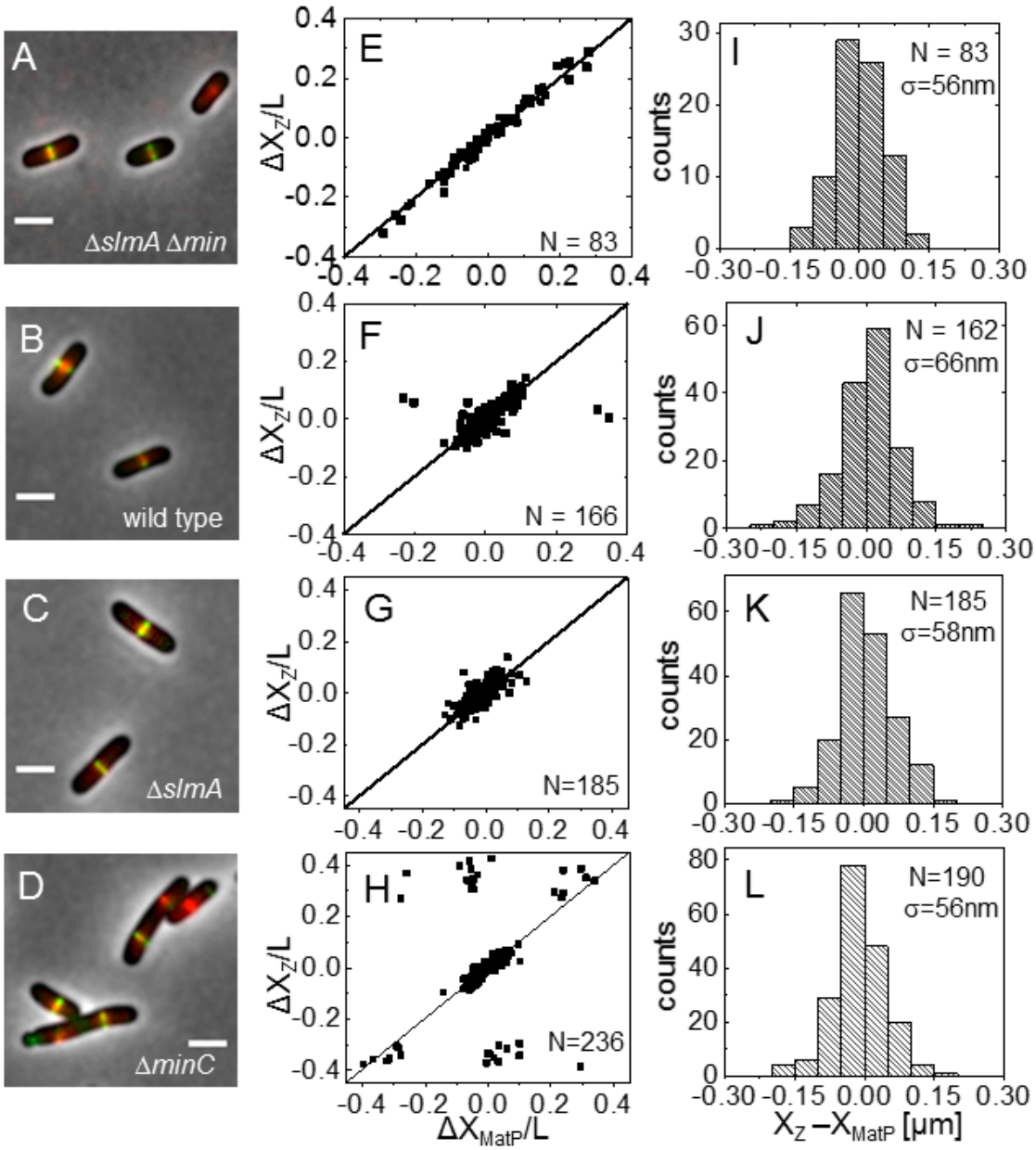

Figure 22. Positioning of the Z-ring relative to the MatP-labeled Ter macrodomain. (A) A composite of ZipA-GFP (green), MatP-mCherry (red), and phase contrast image (grey) of Δ*slmA* Δ*min* cells (strain WD1). Scale bar is 2 μm. (B) The same for wild type strain (strain WD2), (C) Δ*slmA*, and (D) Δ*minC* strains. (E) Location of ZipA-GFP labeled Z-ring (ΔX_z) vs location MatP-mCherry focus (ΔX_{MatP}) in Δ*slmA* Δ*min* cells scaled by the cell length L. Both locations are referenced relative to the cell center. Solid symbols correspond to locations near the center of the nucleoid and open squares to locations near the poles. The straight line corresponds to $\Delta X_z=\Delta X_{MatP}$. Only cells with a single MatP focus are analyzed. (F) ΔX_z vs ΔX_{MatP} for wild type cells, (G) Δ*slmA*, and (H) Δ*minC* cells. (I) Distribution of distances between the Z-ring and the MatP focus along the long axes of the cell for Δ*slmA* Δ*min* cells, (J) wild-type cells (note, in wild type cells the outliers beyond ±0.3 μm have been left out), (K) Δ*slmA*, and (L) Δ*minC E. coli*.

MatP locus was close to the cell pole (Figure 22F). These events were also present in the Δ*slmA* single deletion strain but were absent from the Δ*minC* strain (Figure 22G, H) indicating that the Min system reduces correlations between the Z-ring and the Ter macrodomain. The measured co-localization precision between the MatP-labeled Ter foci and Z-ring centers was $\sigma_{Xz\text{-}XMatP}$ = 56 nm for Δ*slmA* Δ*min* (Figure 22I) and $\sigma_{Xz\text{-}XMatP}$ = 66 nm for wild type cells (Figure 22J). Similar values for $\sigma_{Xz\text{-}XMatP}$ also were found for Δ*slmA* and Δ*min* single deletion strains (Figure 22K, L). All the measurements of co-localization precision $\sigma_{Xz\text{-}XMatP}$ were close to our resolution limit and thus consistent with the hypothesis that the Ter macrodomain and Z-ring co-localize in *E. coli* unless prevented by the Min system. Furthermore, these results demonstrate that the tendency for the Z-ring to associate with nucleoid centers is a result of the association between the Z-ring and Ter region of the chromosome.

The Ter region arrives at the cell center before Z-ring formation

Thus far, colocalization between the Z-ring and nucleoid centers appeared to arise because the chromosomal terminus somehow serves as a signal for Z-ring positioning. However, from static images we were unable to discern whether the Z-ring formed first at midcell and subsequently localized and stabilized the Ter, or if the Ter moved first to midcell and subsequently localized and stabilized the Z-ring. Previously, it was argued that the Z-ring anchored the Ter macrodomain to the cell center through a MatP-mediated link in which the divisome related proteins ZapA and ZapB participate (Espeli, Borne et al. 2012). The co-localization data (Figure 22) clearly supports the presence of this link, which we refer to for shorthand as the “Ter linkage”. The data also raise the possibility that the Ter macrodomain may be important in positioning and stabilizing the location of the divisome. If the Ter positioned and stabilized the Z-ring, there should be some time delay between the arrival of the Ter macrodomain at the cell center and the successive formation of the Z-ring. To test this hypothesis we followed the movement of

the Ter macrodomain and the Z-ring in Δ*slmA* Δ*min* and wild type cells using MatP-mCherry and ZipA-GFP labels. Similar to an earlier report on wild type cells (Mercier, Petit et al. 2008, Espeli, Borne et al. 2012), in Δ*slmA* Δ*min* cells under slow growth conditions the Ter macrodomain moved from the cell pole to the center of the cell at the beginning of the cell cycle (Figure 23A, B). During this movement, the Ter macrodomain either split into two distinct foci or displaced through the cell as a somewhat diffuse unit. The Ter region of the chromosome remained in the center of the nucleoid for the majority of the cell cycle before splitting into two foci during the late stage of cytokinesis. The Z-ring co-localized with the Ter macrodomain early in the cell cycle when the Ter region was positioned at the cell poles and during the majority of the cell cycle when the Ter region was localized as a single unit at midcell (Figure 23A, B). However, our measurements showed that during the period in which the Ter macrodomain dislocated from the new pole to the cell center, the ZipA-GFP focus lagged behind the MatP-labeled Ter macrodomain. We measured the lag period to be $(0.12\pm0.07)\cdot T_d$ for Δ*slmA* Δ*min* cells (Figure 23C). The doubling time, T_d, was about 120 min in these growth conditions. In addition to the lag period, the accumulation of the Z-ring proteins and the Ter macrodomain in the center of the cell showed a different time-dependent behavior (Figure 23D). Following the beginning of the cell cycle, the MatP-mCherry labeled Ter macrodomain arrived at the cell center not only with a shorter delay but also accumulated in the center of the cell *on average* more rapidly than the ZipA-GFP marker for the Z-ring (Figure 23D). We observed similar behavior for wild type cells (Figure 24) although the delay appeared smaller, $(0.02\pm0.10)\cdot T_d$ (Figure 24E).

Time lapse measurements of the Ter macrodomain and the Z-ring in longer (L > 6 μm) Δ*slmA* Δ*min* cells indicate why these cells prefer divisions at the ¼ positions from the cell poles (cf. Figure 14A) and preferentially show Z-rings at the new division sites (cf. Figure 20). The measurements showed that a shift from the cell center to 1/4-positions occurred when the Ter region moved from the center of the cell to 1/4 positions from the cell poles (Figure 23E, F). This

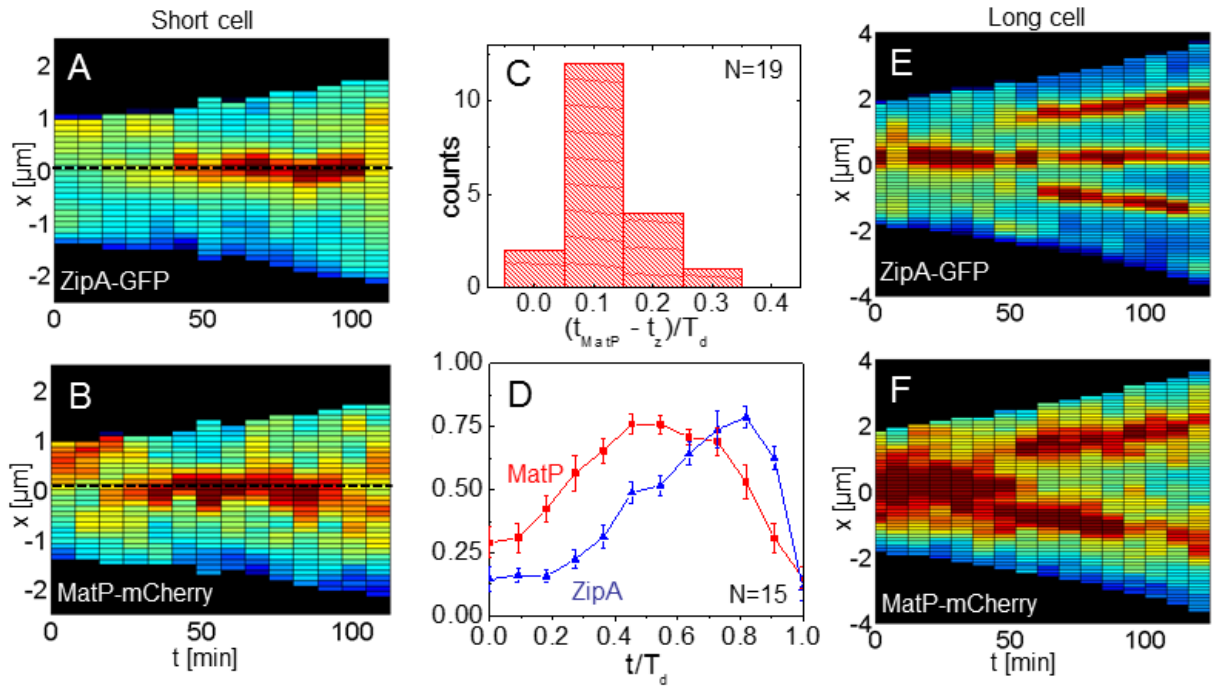

Figure 23. Arrival of the MatP foci and the Z-ring to midcell in Δ*slmA* Δ*min E. coli*. (A) Kymograph (Kymograph, see Appendix, Glossary) of ZipA-GFP along the cell length as a function of time for a short Δ*slmA* Δ*min* cell (strain WD1). (B) Kymograph of MatP-mCherry labeled Ter region for the same cell. In the kymograph, blue corresponds to low and red to high intensity. The dashed black line approximately marks midcell. (C) Histogram of time differences between the arrival of MatP (t_{MatP}) and ZipA (t_z) to midcell. The times are expressed in doubling times. N=19. (D) Accumulation of ZipA-GFP (blue triangles) and MatP-mCherry (red rectangles) at midcell as a function of time. Each curve represents the average from measurements of 15 cells. Error bars represent standard errors. (E) Kymographs of ZipA-GFP and (F) MatP-mCherry in a long Δ*slmA* Δ*min* cell.

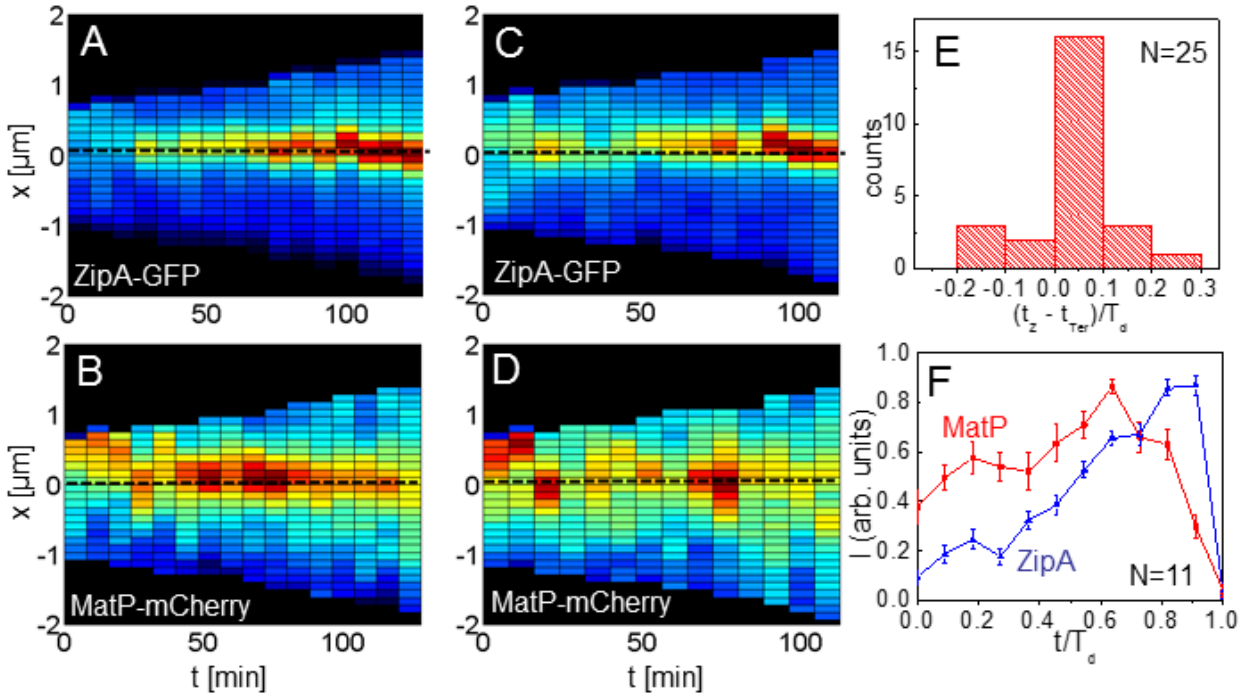

Figure 24. Arrival of the MatP foci and the Z-ring to midcell in wild-type *E. coli.* . (A) Kymograph of ZipA-GFP along the cell length as a function of time for a wild-type cell (strain WD2). (B) Kymograph of MatP-mCherry labeled Ter region for the same cell. In the kymograph, blue corresponds to low and red to high intensity. The dashed black line approximately marks midcell. (C), (D), similar ZipA-GFP and MatP-mCherry kymographs for another wild-type cell. (E) Histogram of time differences between the arrival of MatP (t_{MatP}) and ZipA (t_z) to midcell. The times are expressed in doubling times, N=25. (F) Accumulation of ZipA-GFP (blue triangles) and MatP-mCherry (red rectangles) at midcell as a function of time. Each curve represents the average from measurements of 11 cells. Error bars represent standard errors.

was shortly accompanied by an appearance of the Z-rings in the same locations. In some cases we observed that the Z-ring completely disappeared from the central location, while in other cases, as shown in Figure 23E, F, the Z-ring also persisted in the cell center and was able to complete division. Observations that the Z-ring follows the movement of the Ter macrodomain in a highly correlated manner for both single and multi-nucleoid Δ*slmA* Δ*min* cells are consistent with the hypothesis that the Ter macrodomain acts as a positional landmark for cell division proteins in these cells.

Localization of the Z-ring in the absence of the putative Ter linkage

The protein ZapA is recruited early to the Z-ring, and increases FtsZ protofilament association (Galli and Gerdes 2012). The subsequent binding of ZapB to ZapA is believed to further stabilize the Z-ring (Galli and Gerdes 2012). Moreover, Espeli and colleagues determined that MatP associated with the ZapB protein (Espeli, Borne et al. 2012), and therefore proposed a linkage between the Z-ring (FtsZ) and the chromosome via MatP, ZapB, and ZapA. If the MatP-ZapB-ZapA linkage is involved in the co-localization of the Ter macrodomain and the Z-ring in Δ*slmA* Δ*min* cells, then rendering the linkage dysfunctional by removal of any proteins of the linkage should make the placement of the Z-ring relative to the nucleoid center more random. To verify this prediction we constructed Δ*slmA* Δ*min* Δ*matP*, Δ*slmA* Δ*min* Δ*zapB*, and Δ*slmA* Δ*min* Δ*zapA* triple deletion strains, which shall be referred to as triple deletion MatP, ZapB, and ZapA strains respectively. The triple mutants were imaged using ZipA-GFP as a Z-ring label and DAPI as a stain for nucleoids (Figure 25A-C). Indeed, the distributions of distances between the central Z-ring and nucleoid centers (Figure 25D-F) were more than a factor of two wider after deletion of *matP* ($\sigma_{X_Z-X_n}$= 150nm; p=1·10^{-9}), *zapB* ($\sigma_{X_Z-X_n}$= 220nm; p=5·10^{-18}) and *zapA* ($\sigma_{X_Z-X_n}$= 200nm; p=3·10^{-11}) from Δ*slmA* Δ*min* cells ($\sigma_{X_Z-X_n}$= 66nm). All p-values were calculated using a single

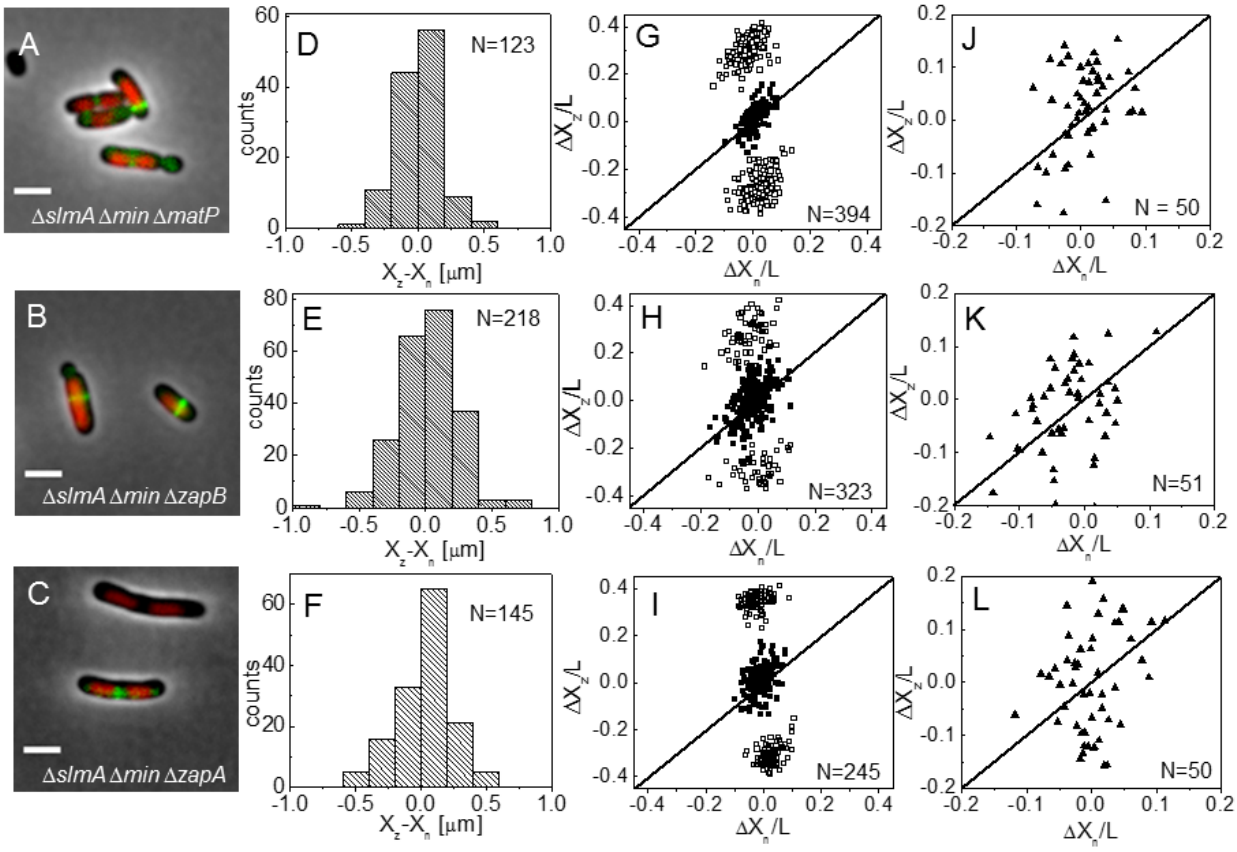

Figure 25. Positioning of the Z-rings relative to the cell and nucleoid centers in triple deletion strains. Composite of DAPI labelled nucleoid (red), ZipA-GFP (green) and phase contrast image in (A) Δ*slmA* Δ*min* Δ*matP*, (B) Δ*slmA* Δ*min* Δ*zapB* and (C) Δ*slmA* Δ*min* Δ*zapA* cells. Scale bar is 2 μm. (D)-(F) Distribution of distances between the Z-ring center and nucleoid center for Δ*slmA* Δ*min* Δ*matP*, Δ*slmA* Δ*min* Δ*zapB*, and Δ*slmA* Δ*min* Δ*zapA* cells, respectively. Displacement of Z-rings relative to the cell center, ΔX_z, as a function of nucleoid displacement, ΔX_n for Δ*slmA* Δ*min* Δ*matP* (G), Δ*slmA* Δ*min* Δ*zapB* (H), and Δ*slmA* Δ*min* Δ*zapA* cells (I). All displacements are normalized by cell length *L*. Solid rectangles mark central and open rectangles polar Z-rings. The solid line corresponds to $\Delta X_z=\Delta X_n$. Data are shown only for cells with a single nucleoid. ΔX_z vs. ΔX_n for central Z-rings over a single compact nucleoids in (J) Δ*slmA* Δ*min* Δ*matP*, (K) Δ*slmA* Δ*min* Δ*zapB*, and (L) Δ*slmA* Δ*min* Δ*zapA* cells, respectively.

tailed Ansari-Bradley test. Note that the horizontal axes in Figure 25D-F spans a distance that is three times larger than in the corresponding graphs for Δ*slmA* Δ*min* and the wild-type cells (Figure 17B, E). Wider X_z-X_n distributions for the triple deletion ZapA and ZapB strains compared to the triple deletion MatP strain are likely caused by irregular Z-ring patterns in the former two strains. ZapA and ZapB have been identified as bundling agents for the FtsZ protofilaments (Galli and Gerdes 2010, Buss, Coltharp et al. 2013). In the absence of these proteins aberrantly shaped Z-rings can be present at the division site which leads to higher uncertainty in Z-ring positions.

We also observed a significantly higher percentage of polar Z-rings (Figure 25G-I) and polar constrictions after deletion of *matP*, *zapB*, and *zapA* from Δ*slmA* Δ*min* background (Table 2). Note that only a fraction of these polar Z-rings leads to polar constrictions. For example, in triple deletion MatP cells the frequency of polar Z-rings was 69% while the frequency of polar constrictions leading to minicelling divisions was 28%. Although the division planes were positioned much more randomly in triple deletion strains than in the Δ*slmA* Δ*min* strain, the cell length distributions were not significantly affected except for the MatP triple deletion strain which was longer (Figure 26). Constancy of cell length may indicate that the timing and duration of cell division are not affected by *zapA* and *zapB* deletions but may be affected by *matP* deletion. Taking that MatP is also involved in organizing the Ter region of chromosome (Niki, Yamaichi et al. 2000, Mercier, Petit et al. 2008), it is conceivable that its deletion could affect cell length more so than a deletion of ZapA or ZapB. Altogether, these findings show that the Ter linkage most strongly affects the accuracy and precision of division plane placement but it appears not to affect the timing of cell division significantly. Consistent with the role of ZapB and MatP in the Ter linkage, we observed a drastic loss of co-localization between the Z-rings and MatP foci in ZapB triple deletion cells and in Δ*slmA* Δ*min* cells when the last 20 amino acids in the C-terminus of MatP were replaced by an mCherry fusion (*matP*Δ*C*-mCherry) (Figure 27). The MatP C-terminal domain has been shown to be important for its interaction with ZapB (Espeli, Borne et al. 2012). While our data indicates that the Ter linkage determines the position of the Z-ring, it has been

Table 2. Frequency of polar Z-rings and minicelling divisions.

Genotype	% of minicelling divisions	N	% of polar Z-rings	N
Wild type	0	943	0	202
Δ*slmA*	0	670	0	166
Δ*minC*	7	1490	16	160
Δ*slmA* Δ*min*	0.2	1326	14	155
Δ*slmA* Δ*min* Δ*matP*	28	660	69	394
Δ*slmA* Δ*min* Δ*zapB*	30	207	33	323
Δ*slmA* Δ*min* Δ*zapA*	8	422	52	245

shown that the linkage is required to stabilize the position of the Ter macrodomain (Espeli, Borne et al. 2012). Our data do not contradict this finding. The MatP focus appeared more delocalized relative to the nucleoid center in the absence of the Ter link in triple deletion MatP and *slmA* Δ*min matP*Δ*C-mCherry* strains compared to the Δ*slmA* Δ*min* and wild type strains (Figure 28). The Ter linkage thus appears to determine the position of the Z-ring and simultaneously stabilize the position of the Ter macrodomain relative to the cell center once the Z-ring has formed.

In cells with compact nucleoids, representative of an early state of chromosome segregation, analysis of Z-ring positions relative to nucleoid-centers revealed essentially no co-localization (Figure 25J-L). The corresponding $\sigma_{X_Z - X_n}$ values for MatP, ZapB, and ZapA triple deletion strains were about a factor of 1.5 larger (230 nm, 344 nm, 280 nm, respectively) than these values for the whole cell population. These differences were statistically significant in both the F-test and in the Ansari-Bradley test. This evidence suggests that the Ter linkage is critical to the specific localization of the Z-ring with the chromosomal terminus at early states of

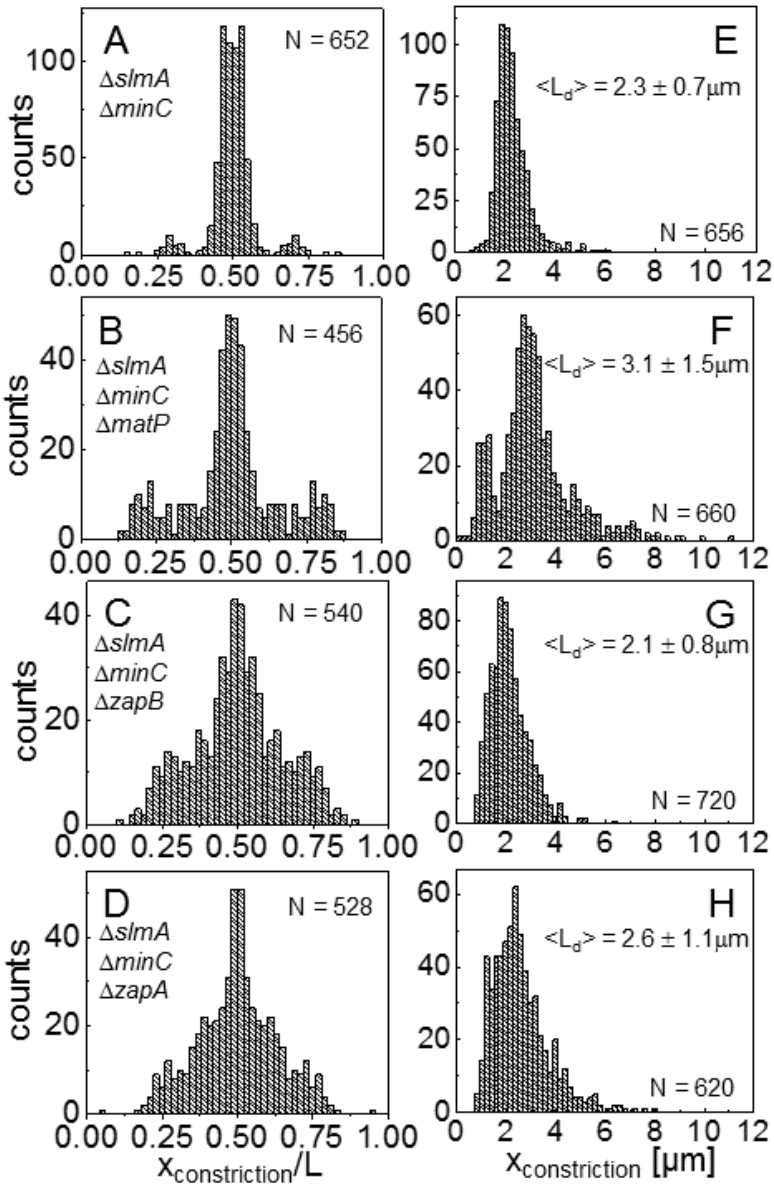

Figure 26. Placement of constrictions for ZapA, ZapB, and MatP triple-deletion *E. coli*. Location of cell constriction in (A) Δ*slmA* Δ*minC* (strain PB194), (B) Δ*slmA* Δ*minC* Δ*zapA* (strain PB300), (C) Δ*slmA* Δ*minC* Δ*zapB* cells (strain PB299), and (D) Δ*slmA* Δ*minC* Δ*matP* cells (strain PB301). Each constriction is measured relative to two different poles and contributes two values to a given histogram that are located symmetrically to 0.5. Note that the placement of constrictions, which are determined from phase contrast images, differ slightly from the final volume fractions (as shown in Figure 14). Constrictions appear closer to mid-cell than the division ratios. For example, constrictions that lead to partitioning of 1 nucleoid to one and 3 nucleoids to another daughter cell are centered at 0.29 in this plot instead of 0.25. Distance distribution of visible constrictions in mother cells based on phase contrast images for corresponding (E) Δ*slmA* Δ*min*, (F) Δ*slmA* Δ*min* Δ*matP*, (G) Δ*slmA* Δ*min* Δ*zapB*, and (H) Δ*slmA* Δ*min* Δ*zapA* *E. coli*. Distances shown are measured from each of the two cell poles. Note that $x_{constriction}$ is somewhat smaller than the length of newborn daughter cells ($L_{daughter}$).

chromosome segregation when the nucleoid morphology is compact. However, once the bi-lobed nucleoid morphology emerges in the triple deletion strains, co-localization between the Z-ring and nucleoid center appears, though much more weakly than in the Δ*slmA* Δ*min* and wild-type strain.

Interestingly, the spatial distributions of those Z-rings that were not located at the poles still displayed a bias towards the cell center (Figure 25D-F). The locations of constrictions in the triple deletion strains, which we measured from phase contrast images, showed an overall positioning bias towards cell centers as well (Figure 26A-D). However, the corresponding distributions were significantly broader in triple deletion strains than in Δ*slmA* Δ*min* cells. The latter findings indicate that while triple deletion strains lack a mechanism to recognize centers of compact nucleoids, they still have a mechanism that can position Z-rings relative to cell center albeit with significantly lower precision and accuracy than the Δ*slmA* Δ*min* and wild-type strains.

Discussion

At the beginning of this work, the Min system and SlmA-mediated nucleoid occlusion were the only two identified molecular systems known to influence Z-ring positioning in *E. coli* (Margolin 2005, Lutkenhaus 2007, Adams and Errington 2009, de Boer 2010). In fast growth conditions, Z-rings form almost exclusively in the space between nucleoids, or at the center of a nucleoid which is in the process of segregating. This localization pattern is consistent with that predicted by the VENO hypothesis. A different localization pattern occurred when cells were grown in nutrient poor media. Slow growing, viable Δ*slmA* Δ*min* remained capable of coordinating cell division and chromosome segregation with high fidelity. The majority of Δ*slmA* Δ*min* cells positioned their division planes accurately relative to nucleoids in slow growth conditions and produced essentially no minicells. In searching for the mechanism responsible for the localization of the Z-ring in these double mutant cells, we found that the Z-rings have a strong tendency to co-localize with the nucleoid centers as opposed to nucleoid free areas of the cell, which ruled out VENO as the

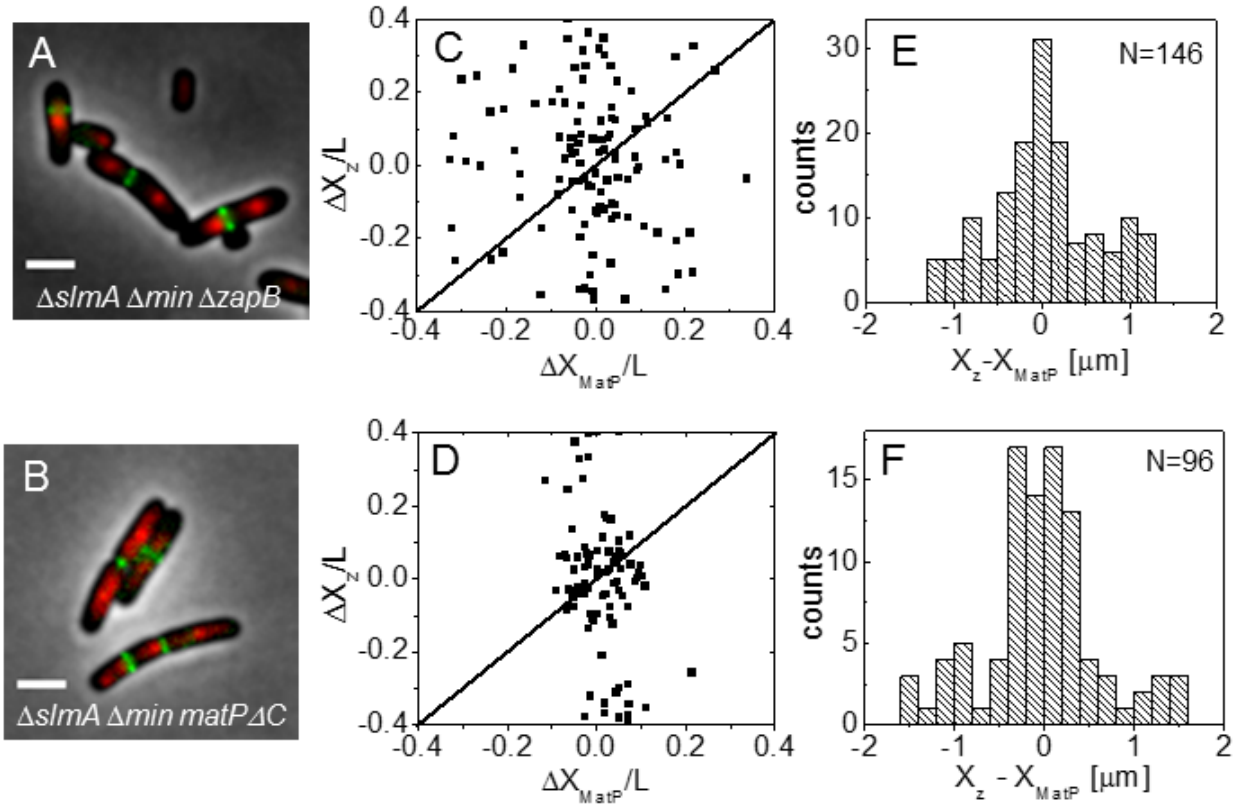

Figure 27. Positioning of the Z-ring relative to the MatP-labeled Ter macrodomain in Δ*slmA* Δ*min* Δ*zapB* (top row) and Δ*slmA* Δ*min matP*Δ*C* (bottom row) strains. (A), (B) A composite of ZipA-GFP (green), MatP-mCherry (red), and phase contrast image (grey). Scale bar is 2 μm. (C), (D) Location of ZipA-GFP labeled Z-ring (ΔX_z) vs location of MatP-mCherry focus (ΔX_{MatP}). Both locations are referenced relative to the cell center. The straight line represents $\Delta X_z = \Delta X_{MatP}$. (E), (F) Distribution of distances between the Z-ring and the MatP focus along the cell length.

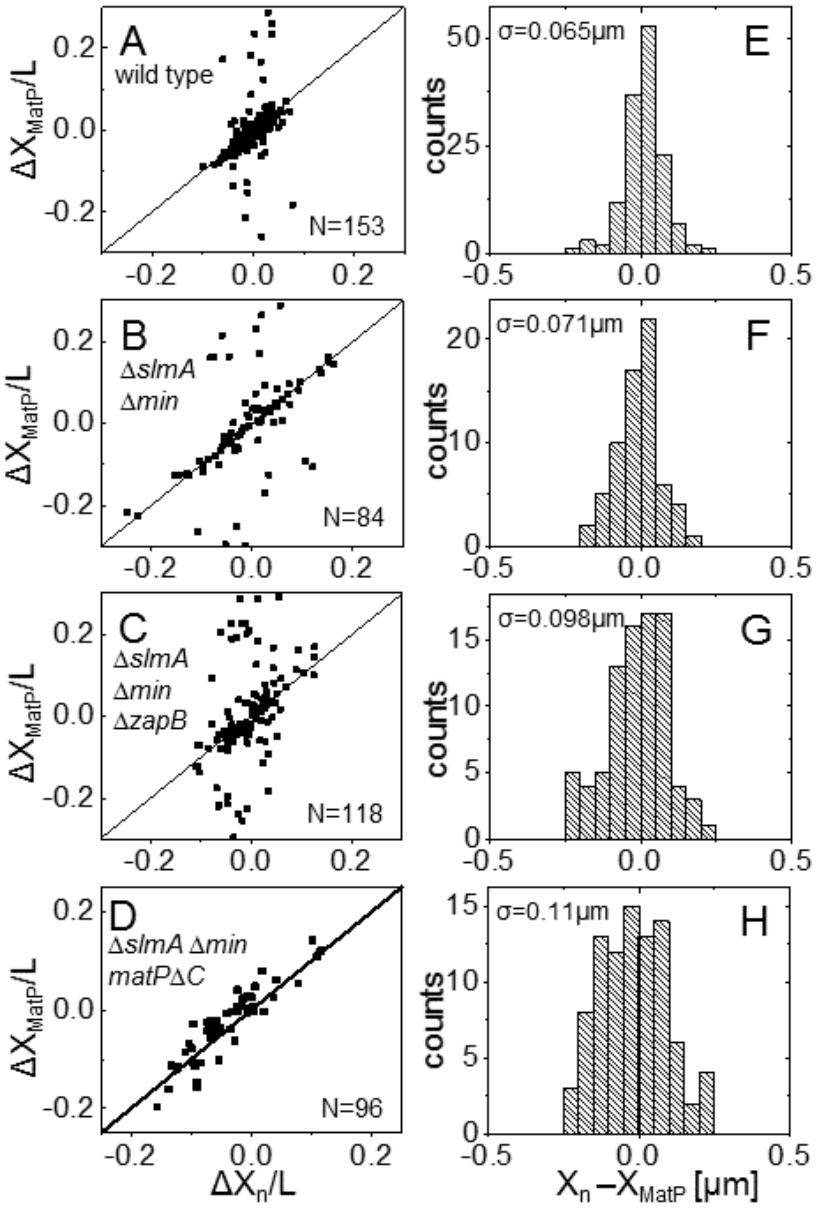

Figure 28. Displacement of MatP relative to the nucleoid center. Left column: Displacements of MatP-focus relative to cell center, ΔX_{MatP}, as a function of nucleoid displacement from cell center, ΔX_n. All displacements are normalized by cell length *L*. The solid line corresponds to $\Delta X_{MatP}=\Delta X_n$. Data are shown only for cells with a single nucleoid. Note that large scatter in $\Delta X_{MatP}/L$ values in all strains is related to movement of Ter macrodomain from the nucleoid periphery to the center of the nucleoid early in the cell cycle. In Δ*slmA* Δ*min matP*Δ*C* strain the movement of Ter macrodomain occurs before cell division and therefore in single nucleoid cells no MatP foci appear at the nucleoid periphery. **Right column:** Distance between nucleoid center and center of MatP focus. Each histogram is compiled from the data on the left column but retaining only these data where ΔX_{MatP} is less than 0.25 μm from the nucleoid center. This selection eliminates spread caused by the cell cycle dependent movement of MatP focus from nucleoid periphery to nucleoid center.

dominating Z-ring positioning mechanism.

Further investigation into the source of the nucleoid signal revealed nucleoid centers were occupied by the Ter region of the chromosome at the time of Z-ring formation, from which the signal originated. The Ter region of the *E. coli* chromosome is organized by MatP proteins (Mercier, Petit et al. 2008). MatP links the Ter macrodomain to the Z-ring through ZapB and ZapA proteins (Espeli, Borne et al. 2012). It was proposed earlier that the Z-ring acts as an anchor for the Ter macrodomain through this linkage (Espeli, Borne et al. 2012). Our time lapse measurements demonstrated a broader role of the Ter linkage. The MatP-decorated macrodomain arrived at the cell center a small fraction of the cell cycle before appreciable assembly of the Z-ring occurred in Δ*slmA* Δ*min* cells. This temporal relationship indicates that the Ter region of the chromosome, through the Ter linkage, localizes the cell division proteins in the early stage of cytokinesis. It is thus the Ter macrodomain that acts as an 'anchor' for cell division proteins during the formation of the divisome. However, the interactions between the Z-ring and the Ter macrodomain appear to stabilize the position of Ter macrodomain later in the cell cycle. During maturation of the divisome, especially when it becomes fixed to the cell wall, the divisome acts as a stabilizing element for the Ter macrodomain, holding it fixed in the cell center (Espeli, Borne et al. 2012).

At this point, we do not understand why Z-rings localize differently depending on whether cells grow quickly or slowly. However, we note that fast-growing Δ*slmA* Δ*min E. coli* have many more Z-rings than slowly growing cells. If we could over-express FtsZ in slow-growth conditions, then perhaps we could generate a similar number of rings. Assuming each chromosomal terminus possesses a colocalized Z-ring, where would the additional Z-rings localize? It is possible that at this point the VENO mechanism would become more prevalent and encourage the remaining Z-rings to form at cell poles or at inter-nucleoid spaces in a similar way to the fast-grown Δ*slmA* Δ*min* cells. More work needs to be done to address this question, as well as the physiological difference between fast and slow grown Δ*slmA* Δ*min E. coli* in general.

A positive regulation mechanism for cell division

The Ter linkage facilitates correct placement of the division plane relative to the chromosomes. Severing the linkage in Δ*slmA* Δ*min* cells leads to increased number of inviable, DNA-less minicells and less symmetric division of mother cells. Both outcomes limit the fitness of cells. Unlike the Min system and SlmA-mediated nucleoid occlusion, which are inhibitors of Z-ring formation, the Ter linkage represents the first system to promote Z-ring localization at a specific location in *E. coli*. The link guides cell division proteins to the location of the future division site and not away from the undesired locations in the cell as do the Min system and SlmA-mediated nucleoid occlusion.

The spatial Z-ring localization signal by the Ter linkage is dynamic and it is likely not very strong. Time-lapse measurements show that the Ter linkage temporarily disassembles when the Ter region of the chromosome moves from the cell pole to its center. Also, the Ter region becomes disconnected from the divisome near the end of cytokinesis. The Ter linkage appears thus to provide a dynamic and reconfigurable connection, which biases assembly of cell division proteins towards the Ter region, but does not commit cells to division.

The Ter linkage and the Min system define two independent positioning systems for the divisome. The Min system is capable of positioning the Z-ring without any nucleoid in *E. coli* minicells albeit with somewhat lower precision than in wild type cells (Sun, Yu et al. 1998). The position defined by the Min system may, however, not always match the position defined by the Ter macrodomain. In these conflicting cases, the Min system has the dominant effect over the Ter linkage. Consistent with this idea, we observed in long cephalexin treated wild-type cells that Z-rings localized only at the cell center rather than at the locations of MatP foci. Also, in the Min^+ cells we observed no appreciable accumulations of the ZipA-GFP reporter at the cell poles although this location is favored by the Ter linkage at the early stages of the cell cycle.

Unlike the Min system, the effect of SlmA on the Ter linkage was less pronounced. The only observed consequence of deleting *slmA* in our measurements was the decrease in polar Z-

rings and minicelling divisions in the Δ*slmA* Δ*min* strain compared to the Δ*minC* strain. We hypothesize that SlmA removal, i.e. removal of the negative regulator, effectively strengthens the positive regulation due to the Ter linkage. The stronger regulation due to the Ter linkage then leads to more abundant Z-rings in the vicinity of the Ter region(s) of the chromosome, which sequester more efficiently the Z-ring related proteins from other regions of the cell including cell poles. As result, less polar Z-rings and minicelling divisions are present in the Δ*slmA* Δ*minC* than in the Δ*minC* cells. More work is needed to further test this hypothesis as well as to understand the exact mechanism of how SlmA regulates Z-ring assembly.

Positive regulation mechanisms in other bacteria

Evidence of positive control in localizing cell division proteins has been reported recently for several bacterial species including *Streptomyces* (Willemse, Borst et al. 2011), *Myxococcus xanthus* (Treuner-Lange, Aguiluz et al. 2013) and *Bacillus subtilis* (Moriya, Rashid et al. 2010, Rodrigues and Harry 2012). In *Streptomyces* the positive control appears to be achieved by a combination of SsgA and SsgB proteins (Willemse, Borst et al. 2011). In *Myxococcus xanthus*, the protein PomZ is shown to have a similar role (Treuner-Lange, Aguiluz et al. 2013). Although these proteins arrive before FtsZ in both organisms, it remains unclear which molecular mechanisms are responsible for their own localization. PomZ appears to localize over the nucleoid although it has not been determined if it is linked to any specific chromosomal region (Treuner-Lange, Aguiluz et al. 2013). Positioning of SsgA and SsgB relative to chromosome also is not clear yet.

A positive localization signal, or potentiaton as the authors refer to it, appears to be present also in *B. subtilis* (Moriya, Rashid et al. 2010). However, the mechanism seems to be very different in *B. subtlis* in which the positive signal was reported to appear during the assembly of the replichore, i.e. much earlier than in *E. coli.* Moreover, it was observed that “some factor” attracted Z-ring assembly to the oldest division site in *B. subtilis* outgrowing spores that lacked Min and

Noc proteins (Rodrigues and Harry 2012). This is contrary to our observation in *E. coli*, where we observe a bias of the Z-ring towards sites between newly segregating nucleoids. Taking that *B. subtilis* is evolutionarily divergent from *E. coli,* differences are expected. It remains to be determined how widespread the Ter linkage is among other bacteria. MatP is conserved in enterobacteria (Mercier, Petit et al. 2008), but taking its important functional role, structurally similar assemblies can be present more broadly.

Additional mechanisms for localization of cell division proteins

Deletion of any of the three proteins involved in the Ter linkage affects the midcell positioning of the Z-ring but does not lead to complete positioning randomness. Accordingly, a mechanism responsible for the localization of cell division proteins must exist in addition to the MatP-ZapB-ZapA mediated Ter linkage in Δ*slmA* Δ*min* cells. The mechanism does not appear to link Z-rings to nucleoid centers at early stages of chromosome segregation when there is no discernable bi-lobed nucleoid structure (compact nucleoids). Interestingly, later in chromosome segregation when a distinct bi-lobed morphology appears, stronger correlations between the Z-rings and nucleoid centers emerge. Two positioning mechanisms that link the nucleoid and divisome have been discussed in the past (Rabinovitch, Zaritsky et al. 2003, Zaritsky and Woldringh 2003) that can possibly explain such behavior. Both mechanisms rely on the transertional linkages that connect bacterial DNA through transcribed RNA and simultaneously translated membrane proteins to the plasma membrane of the cell (Norris 1995). In one hypothesis transertional linkages create local membrane crowding (Zaritsky and Woldringh 2003) that prevents Z-ring formation in the vicinity of the nucleoid. In another hypothesis, mechanical tension produced by the transertional linkages due to chromosomal segregation acts as a (positive) signal to guide localization of cell division proteins (Rabinovitch, Zaritsky et al. 2003). Alternatively, a positioning mechanism not mediated by the nucleoid or transertional linkages but

by the division proteins themselves may properly position the nucleoids relative to the division plane. Answers to this scientific question are devoted to the next chapter.

Chapter 3: In the absence of all known Z-ring positioning systems, large-scale movement of DNA through the septal pore in *Escherichia coli* ensures cell viability – Chromosome movement relative to the divisome

Remarkably, our previous studies demonstrated that despite the complete absence of all known Z-ring localization mechanisms, i.e. SlmA, positive regulation from the Ter region, and the Min system, *E. coli* remained viable in slow growth conditions (Bailey, Bissichia et al. 2014), though the resulting cells had a strong tendency to divide asymmetrically. Viability of these cells alone implies some mechanism remains which is capable of coordinating the overall progression of cell division with the underlying chromosomes such that both daughters received complete chromosomes following cytokinesis. We noted that this mechanism does not appear to link Z-rings to nucleoid centers at early stages of chromosome segregation when there is no discernable bi-lobed nucleoid structure (compact nucleoids), though intriguingly later in chromosome segregation when a distinct bi-lobed morphology appears, stronger correlations between the Z-rings and nucleoid centers emerge.

In this chapter, which has been submitted for review, we present experimental results that demonstrate daughter cells remain viable in many cases because large fractions of the chromosome move through the closing division septum very late in the cell cycle. Though we do know the origin of the force which drives large-scale chromosome movement, we show that this DNA movement is coupled to the cell's ability to constrict. Accordingly, we hypothesize that cell constriction alone may be sufficient to coordinate cell division and chromosome partitioning. If true, this hypothesis may have important implications on early bacteria, namely, that more elaborate and intricate cell division-chromosome partitioning mechanisms (evolved mechanisms) may not have been needed to produce viable progeny.

Z-rings localize over nucleoids when ZapA or ZapB is removed from Δ*slmA* Δ*min* cells.

As previously shown, Z-ring placement in Δ*slmA* Δ*min* Δ*matP* (triple deletion MatP), Δ*slmA* Δ*min* Δ*zapA* (triple deletion ZapA), and Δ*slmA* Δ*min* Δ*zapB* (triple deletion ZapB) strains had only a weak bias towards the nucleoid center (Bailey, Bissichia et al. 2014). Accordingly, we first characterized the placement of the Z-ring in these three strains further. We use ZipA-GFP as a Z-ring label and DAPI to stain the nucleoids. In accordance with the earlier report (Bailey, Bissichia et al. 2014), in ZapA (Figure 29A,B) and in ZapB (Figure 29C, B) triple deletion strains, Z-rings frequently localized over nucleoids instead of the inter-nucleoid regions or at locations over nucleoids that were not completely separated but nevertheless featured a minimum in the intensity line profile of the DAPI labeled nucleoid (cf. Figure 29D). Note that this minimum is associated with a characteristic bilobed appearance of the nucleoid. We will refer to this minimum also as a "gap" between segregating nucleoids even though physically the two nucleoids may be in contact with each other or even linked by an unreplicated region. For both ZapA and ZapB triple deletion cells, approximately 40% of Z-rings localized over nucleoids, which was about twice higher than the percentage of Z-rings localizing over nucleoids in either the wild-type or Δ*slmA* Δ*min E. coli* (Figure 29G). Conversely, in the MatP triple deletion strain, Z-rings localized away from nucleoids at the cell poles or over nucleoid gaps (Figure 29E, F). We found only 8% of Z-rings localized over nucleoids without visible gaps but a large fraction of rings (56%) were found at the cell poles in this strain (Figure 29G). Despite the lack of all known Z-ring positioning systems, Z-ring placement in the MatP triple deletion strain still was consistent with the phenomenological description of nucleoid occlusion.

We hypothesized that some of the gaps between nucleoids in the ZapA and ZapB triple deletion strains could have arisen not because of nucleoid segregation but because the closing division septum forced the two chromosomal masses apart. To investigate this possibility, we treated each strain with cephalexin to produce long (10-15 μm), multi-nucleoid cells that lacked

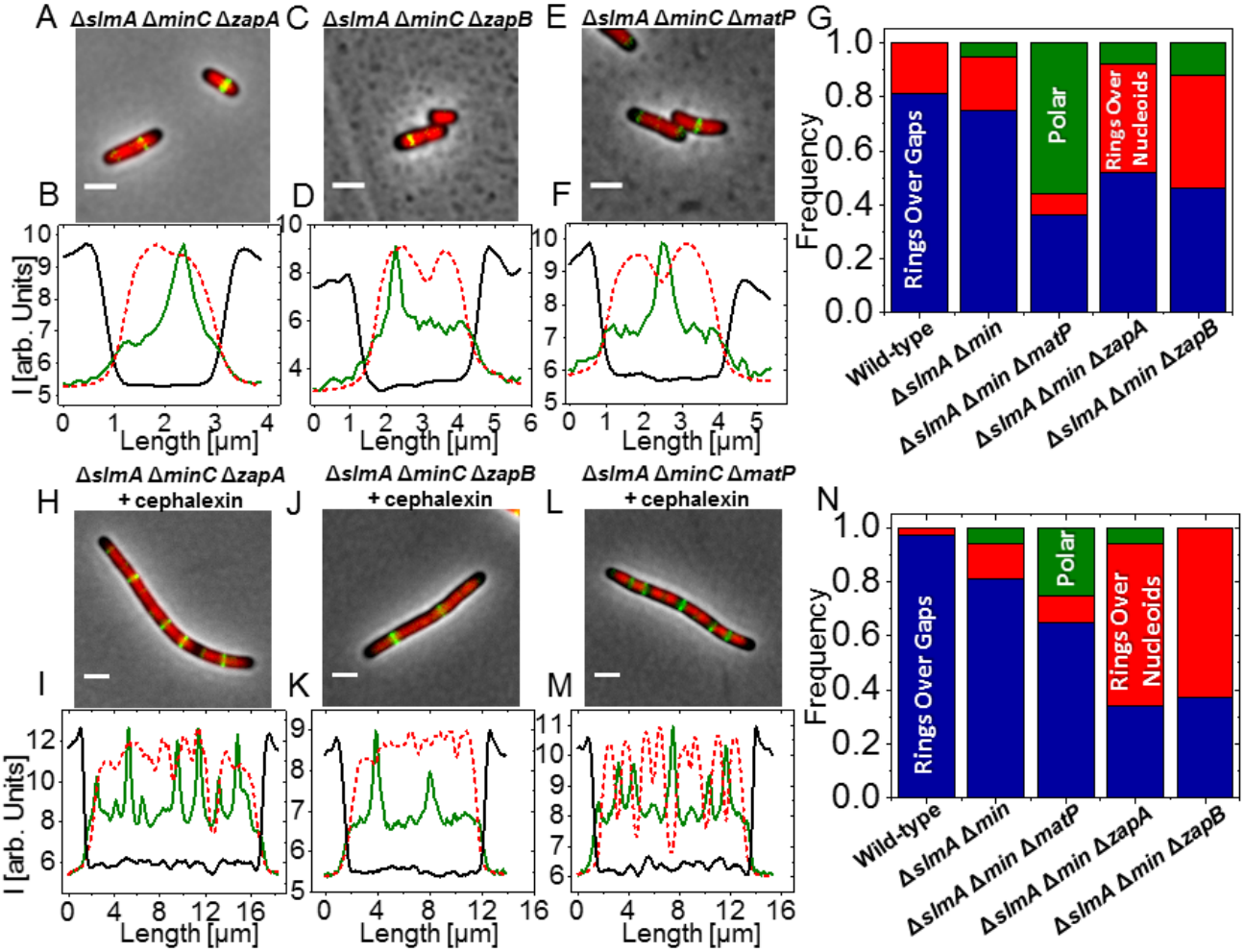

Figure 29. Differential nucleoid occlusion effect in ZapA and MatP triple deletion cells. Composite of ZipA-GFP (green), DAPI (red), and phase contrast images (gray) of a (A) ΔslmA ΔminC ΔzapA, (C) ΔslmA ΔminC ΔzapB, and (E) ΔslmA ΔminC ΔmatP cells. (B), (D), and (F) The intensity line profiles along the long axis of the cell for the cells shown in (A), (C), and (E), respectively. (G) Frequency of Z-rings localized over the nucleoid gaps, over the nucleoids, and at the cell poles in different strains. Composite image of cephalexin-treated (H) ΔslmA ΔminC ΔzapA, (J) ΔslmA ΔminC ΔzapB and (L) ΔslmA ΔminC ΔmatP cells. (I), (K), and (M) The intensity line profiles along the long axis of the cell for the cells shown in (H), (J), and (L), respectively. (N) Frequency of Z-rings in different cellular locations for cephalexin treated cells. Scale bars on all images are 2μm.

constrictions (Figure 29H-M). Consistent with this hypothesis, the percentage of ZapA and ZapB triple deletion cells with Z-rings localized over nucleoids rose from about 40% to 65% (Figure 29N). Interestingly, fewer Z-rings were positioned over the nucleoids in cephalexin treated Δ*slmA* Δ*min* (13%) and wild-type strains (~3%) as compared to the same cells without cephalexin treatment. In the MatP triple deletion strain, the fraction of Z-rings over the nucleoids remained approximately constant (10%) but the frequency of polar rings decreased to 25%. Assuming that in the MatP triple deletion strain Z-rings can localize everywhere but over the nucleoids, such a decrease in polar rings is expected because polar regions comprise a smaller fraction of the total cell volume in filamentous cells than in regularly sized cells. Altogether the data from cephalexin-treated cells further confirms that the nucleoid minimally influences Z-ring placement in ZapA and ZapB triple deletion strains, though intriguingly the NO effect remains in the MatP triple deletion strain even without SlmA.

The majority of cells remain viable even when the division plane is misplaced relative to nucleoids.

To determine the consequences of Z-ring localization over nucleoids in triple deletion ZapA and ZapB cells, we performed fluorescence time-lapse microscopy and followed the fates of these cells after division. Instead of labeling the nucleoid with DAPI, we used a chromosomal HupA-mCherry construct. It has been shown that HupA binds to DNA non-specifically and gives the same localization pattern as the DAPI label but allows for time-lapse imaging without adverse effects to cells (Männik, Wu et al. 2012, Fisher, Bourniquel et al. 2013). Remarkably, the majority of ZapA and ZapB triple deletion cells were viable even though in many cases the Z-ring positioned asymmetrically relative to the nucleoid center and appeared at first sight to guillotine the nucleoids (Figure 30A). Here, we consider a newborn cell to be viable if it is able to produce two new daughter cells with chromosomes after approximately doubling its size (Figure 30A, B). However, not all daughter cells produced in asymmetric division were viable despite inheriting at

least some chromosomal DNA (Figure 30C, D). The inviable cells were always the smaller daughters of the two that resulted from the asymmetric division. The larger daughters from all asymmetric divisions grew robustly. Among the smaller daughter cells, a clear distinction between viable and inviable cell populations could be made based on their change of chromosomal mass in time (Figure 30B, D) and by their elongation rate (Figure 30E, F). The inviable cells containing DNA material stopped growth immediately after division as did anucleate minicells containing no DNA material. On the other hand, the small, viable daughters grew with essentially the same mass-doubling times as the larger daughters with the exception of a group of ZapB triple deletion cells that showed slower rates (Figure 30G, H). It was also clear the inviable cells that resulted from asymmetric division contained less DNA, and their chromosomal content was distinctly smaller than the cells that were capable of supporting growth based on estimates of the apparent, two-dimensional nucleoid area (Figure 31A-E, Figure 32A-D, Table 3) and fluorescence signal from the HupA-mCherry label (Figure 33A-E). The inviable cells did not lyse during the 10 hour observation period and in this respect behaved as DNA-free mini (Sun, Yu et al. 1998) and maxicells (Pazos, Casanova et al. 2014), which show very limited growth but maintain some cellular functions such as membrane integrity. The abrupt halting of growth and low DNA content in inviable cells implies that these cells failed to inherit complete chromosomes while the asymmetrically dividing cells that were viable and did grow likely received at least a full genetic complement of DNA.

Large chromosome fractions move across the division plane in asymmetrically dividing cells.

To better understand chromosomal dynamics during asymmetric divisions in ZapA and ZapB triple deletion cells, we analyzed positions of nucleoids and Z-rings from time-lapse images.

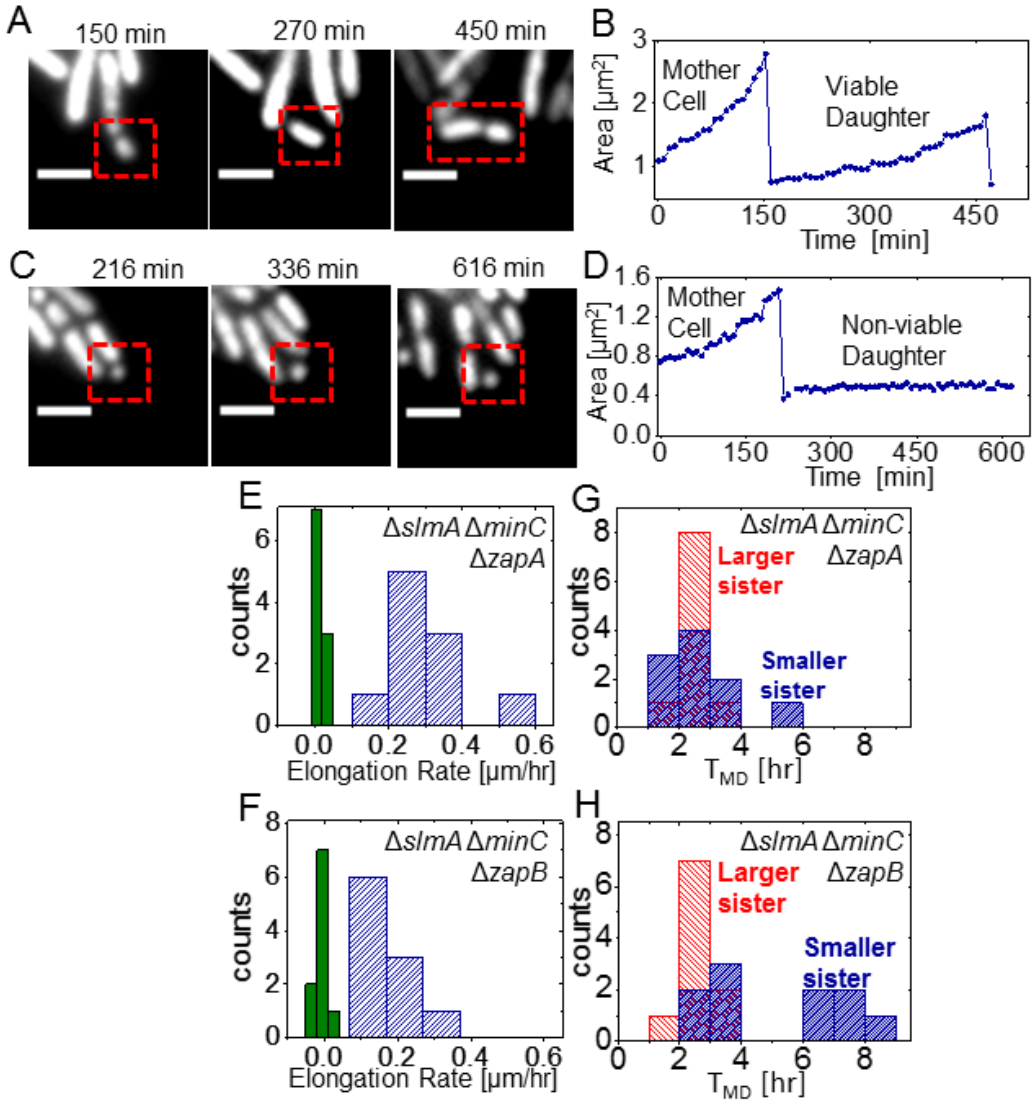

Figure 30. Evidence for nucleoid guillotining in ZapA and ZapB triple deletion cells. (A) Time series of HupA-mCherry labelled nucleoids in ZapA triple deletion strain. A nucleoid from a small viable daughter cell resulting from an asymmetric division is indicated by a red box and is shown at three time points: at birth, at the middle of cell cycle, and when the nucleoids separate from each other. (B) The area of the nucleoid as a function of time for this cell. (C) Nucleoid images of an inviable ZapA triple deletion cell (boxed) at its birth, two hours, and 6.5 hours later. We interpret this nucleoid as having been guillotined during the division. (D) The area of the nucleoid versus time for this cell. (E) Elongation rates for ZapA triple deletion cells that we considered to have a full complement of genes (hatched blue) and guillotined chromosomes (solid green). Both types of cells have resulted from asymmetric division and contain some chromosomal DNA. (F) The same for the ZapB triple deletion strain. (G) Mass doubling times (TMD = 2.75 ± 1.31 [hr]) for ZapA triple deletion cells of (E) that divided asymmetrically but were considered to have a full complement of genes (hatched blue) along with the TMD (2.65 ± 0.50 [hr]) of the larger sister cell (red). (H) The same for the viable ZapB triple deletion cells from (F) from the asymmetric sister TMD = 5.17 ± 2.23 [hr] and for the larger sister TMD = 2.65 ± 0.49 [hr].

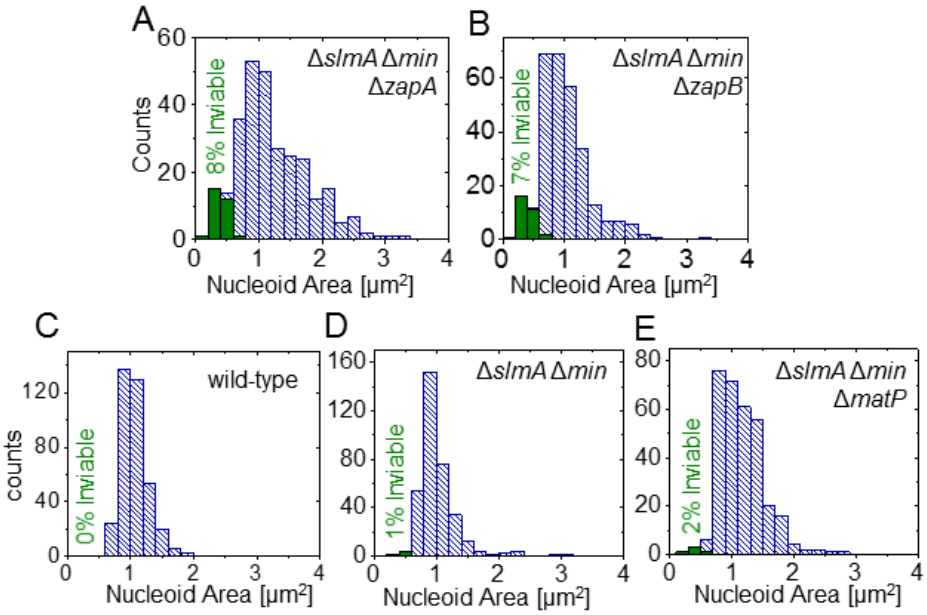

Figure 31. Percentages of inviable divisions and nucleoid areas following cell division for ZapA, ZapB, and MatP triple deletion strains. Histograms of nucleoid areas just following cell division for (A) ZapA triple deletion, (B) ZapB triple deletion, (C) wild-type (D) ΔslmA Δmin, and (E) MatP triple deletion *E. coli*. The areas have been measured from time-lapse images. Both sister chromosomes of the division event are accounted. Green solid bars correspond to nucleoid areas of inviable, and hatched blue bars to viable cells.

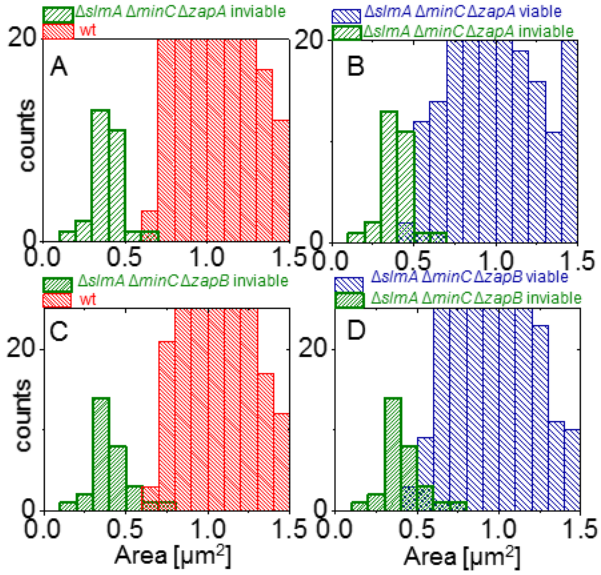

Figure 32. Comparison of nucleoid areas in inviable and viable ZapA and ZapB triple deletion cells and in wild type cells. (A) Comparison of nucleoid areas for inviable ZapA triple deletion cells (MB15, N=29) to wild type cells (strain MB2). The distributions have essentially no overlap. (B) Comparison of nucleoid areas in viable and inviable (N=29) cells both in ZapA triple deletion strain. This Figure shows a zoomed in region of Figure 31A, B. (C) and (D) The same comparisons in ZapB triple deletion strain (strain MB16, N=30 inviable cells).

Table 3: 2D Areas of nucleoids measured just following cell division for viable and inviable triple-deletion *E. coli*

Strain	Viable [μm^2]	Inviable [μm^2]
WT (MB2)	1.05 ± 0.21 (N=372)	NA
Δ*slmA* Δ*min* *(MB1)*	1.02 ± 0.30 (N=343)	0.45 ± 0.07 (N=5)
Δ*slmA* Δ*min* Δ*matP* *(MB14)*	1.18 ± 0.39 (N=319)	0.38 ± 0.10 (N=5)
Δ*slmA* Δ*min* Δ*zapA* *(MB15)*	1.26 ± 0.54 (N=273)	0.39 ± 0.10 (N=29)
Δ*slmA* Δ*min* Δ*zapB* *(MB16)*	1.05 ± 0.39 (N=278)	0.41 ± 0.12 (N=30)

*Means, standard deviation, and number of analyzed cells are indicated. The table is from Figure 30.

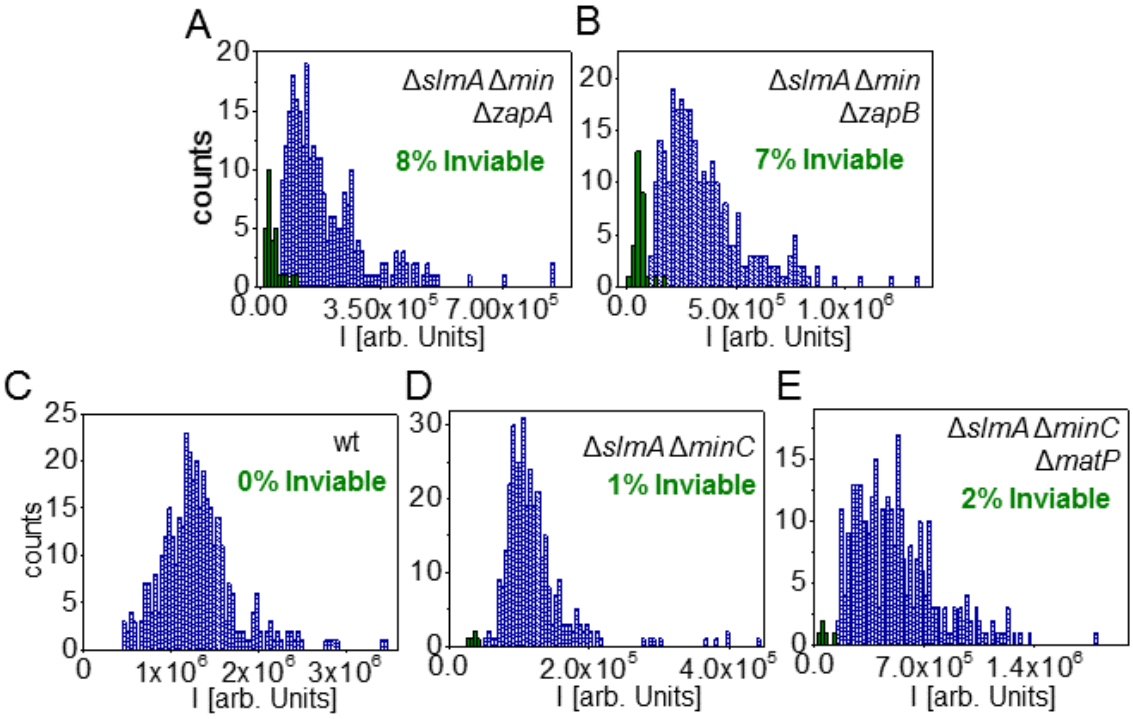

Figure 33. Comparison of integrated fluorescence intensities between inviable and viable cells for different strains. HupA-mCherry fluorescence intensities are measured immediately after division of the mother cell. Solid green bars show integrated fluorescence intensities from inviable daughters and blue hatched bars from viable daughters. Frequencies of inviable cells are indicated for each strain (A) Δ*slmA* Δ*min* Δ*zapA* (strain MB15, N_{viable}=273, $N_{inviable}$=29), (B) Δ*slmA* Δ*min* Δ*zapB* (strain MB16, N_{viable}=278, $N_{inviable}$=30) , (C) Wild-type (strain MB2, N_{viable}=372, $N_{inviable}$=0), (D) Δ*slmA* Δ*min* (strain MB1, N_{viable}=343, $N_{inviable}$=5), and (E) Δ*slmA* Δ*min* Δ*matP* (strain MB14, N_{viable}=319, $N_{inviable}$=5), respectively. The distributions from viable and inviable cells are distinctly different.

In this analysis, we examined cells whose Z-rings were positioned asymmetrically relative to the centers of chromosomes. There was no apparent nucleoid occlusion effect in these cells, which, if present, would have prevented Z-rings from forming and constricting over unsegregated nucleoids. In a typical asymmetric division event (Figure 34A, B, Figure 35), we observed first a small shoulder to emerge from one side of the nucleoid density profile at the location of the Z-ring. In time, the shoulder grew into a well-distinguishable peak in the profile that separated from the mother chromosome (Figure 34D). The nucleoid mass, which eventually partitioned into the smaller daughter cell, underwent the most extensive growth within approximately a 30 minute interval. The growth ceased about the time when the ZipA-GFP label dissociated from the septum. The growth of this cell resumed after a lag period (of about 1 hour) and gave rise to two new viable daughter cells.

To quantify these division plane-induced chromosomal movements, we measured the chromosomal mass changes on both sides the division plane in time (Figure 34C, D). The analysis (described in the Appendix) revealed the relative fraction of the smaller daughter's chromosomal mass to that of the whole chromosome sharply increased in time just before the disappearance of the Z-ring (Figure 34E). Once the division was completed, the fraction stayed constant. The change in the relative amount of DNA on the side of the smaller daughter cell indicates chromosomal DNA crossed the division plane during septum closure, i.e. translocated, from the larger daughter cell's compartment. The change cannot be explained simply by replication and growth, because these processes would not have caused the fraction to change. Indeed, when we treated cells with cephalexin, which inhibits constrictions, cells grew and replicated their chromosomes but the fraction did not change even when Z-rings were positioned very close to nucleoid edges (Figure 40C). We found very similar DNA movement across the septum also occurred in ZapB triple deletion cells (Figure 36) and that in both strains it was not dependent on whether the resulting daughter cells were viable or not. However, we observed

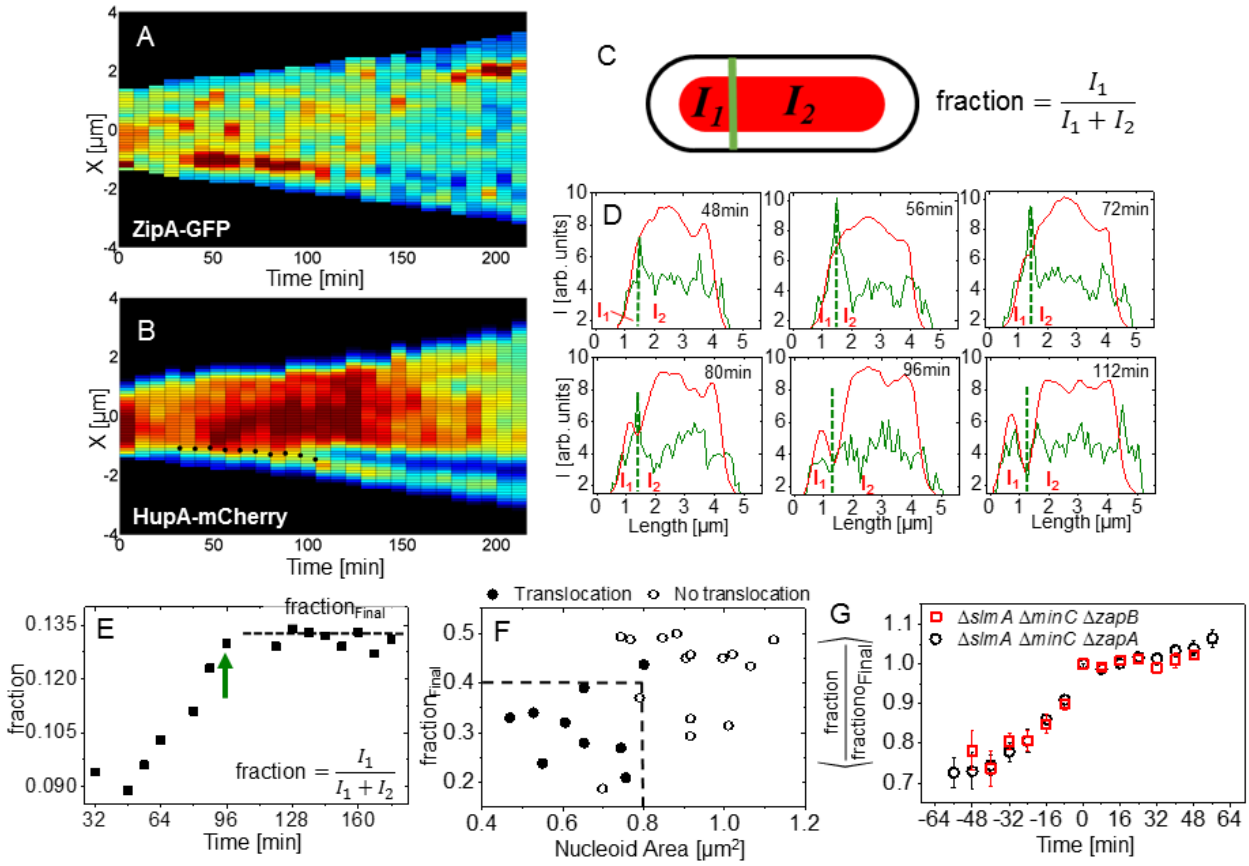

Figure 34. The nucleoid translocates across the septum in asymmetrically dividing ZapA triple deletion cells. (A) Kymograph of ZipA-GFP (Z-ring label) for a triple deletion ZapA cell (strain MB15). Blue corresponds to low and red to high intensity. Black areas are outside the cell. (B) Kymograph of HupA-mCherry labeled nucleoid for the same cell. Overlaid black dots show locations of the Z-ring as determined from the data shown on panel (A). (C) Schematic illustrating the chromosomal mass ratio calculation for the smaller daughter. Red represents the nucleoid, and the green vertical line represents the Z-ring. I_1 and I_2 indicates the integrated fluorescent intensities of the nucleoid label on either side of the cell division plane. (D) The intensity line profiles of the ZipA-GFP (green) and HupA-mCherry (red) at selected time points for the same cell. The septum is marked by dashed vertical line. (E) The fraction of the nucleoid material in smaller daughter side of the septum as a function of time (same cell). The vertical arrow shows the approximate time the ZipA-GFP ring disassembles. (F) Distribution of division events showing translocation (filled circles) or no translocation (empty circles) a as a function of nucleid area and fraction of chromosomal material within the smaller daughter's compartment immediately after cell division. (G) The population averaged normalized fraction of nucleoid material in the smaller daughter's compartment of the septum as function of time for ZapA (MB15, N=12, circles) and ZapB (strain MB16, N=11, squares) triple deletion cells. Error bars represent s.e.m.

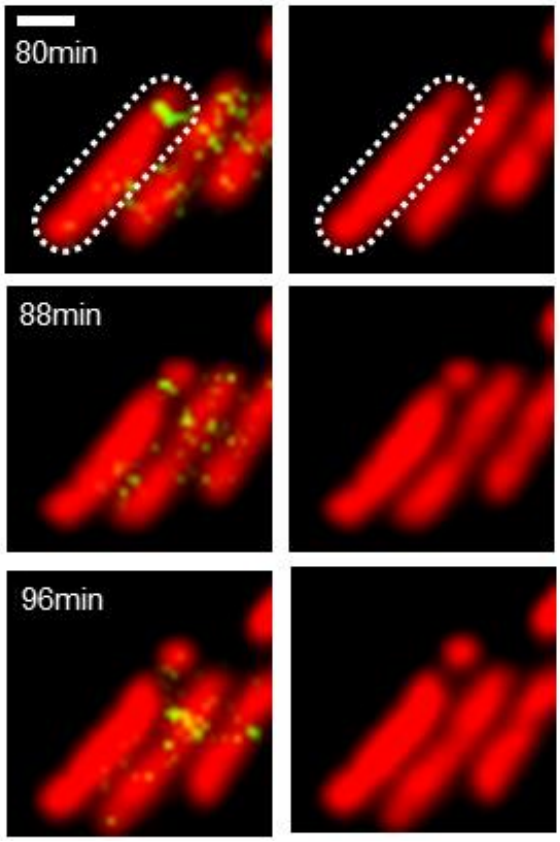

Figure 35. Fluorescent images of nucleoids and Z-ring during the translocation process for the cell shown in Figure 34A, B, D, and E. Only frames with the largest chromosomal movement are shown. Left Panel: Overlay of HupA-mCherry (red) and ZipA-GFP (green) signals. Right Panel: HupA-mCherry image only. Scale bar is 1 μm.

clear chromosomal movement only for asymmetric divisions (final fraction ≤ 0.4) that produced small daughter cells (nucleoid area ≤ 0.8 μm^2) (Figure 34F). For such divisions, and restricting the following analysis only to viable cells, the translocating movement was observable within about a 30 min interval preceding the completion of division (Figure 34G). During this period the relative amount of chromosomal mass within the smaller daughter's side increased on average about 30% relative to the larger daughter's side. The change in the normalized fraction (i.e. curve in Figure 34G) can also be used to estimate the total fraction of DNA translocated during the division and the average translocation rate. The fraction of the total amount of DNA translocated to the total amount of chromosomal DNA contained within the smaller daughter at the end of division is equivalent to the difference between the normalized fraction at the beginning and end of translocation (for details see SI Appendix, Text). Thus, in both ZapA and ZapB triple deletion strains, about 30% of the chromosomal mass that ultimately ende up within the smaller daughter moved across the division plane just prior to division. Assuming smaller daughters inherited one full chromosome equivalent (4.6 Mb), we determine the population averaged translocation rate to be approximately 770 bp/s. It is possible that the daughters contained more than one genome equivalent of DNA at the time of division because cells growing in glucose minimal medium typically do. In this case, the actual rate is somewhat higher. In individual translocation curves, much more abrupt increases in chromosome content could be seen with the estimated rates as high as 3000 bp/s. In rare cases we could also observe retractions of chromosomes, which lead to complete (Figure 37) or partial removal of DNA from the compartment of the smaller daughter. Note that retraction events were excluded from analysis in Figure 34G.

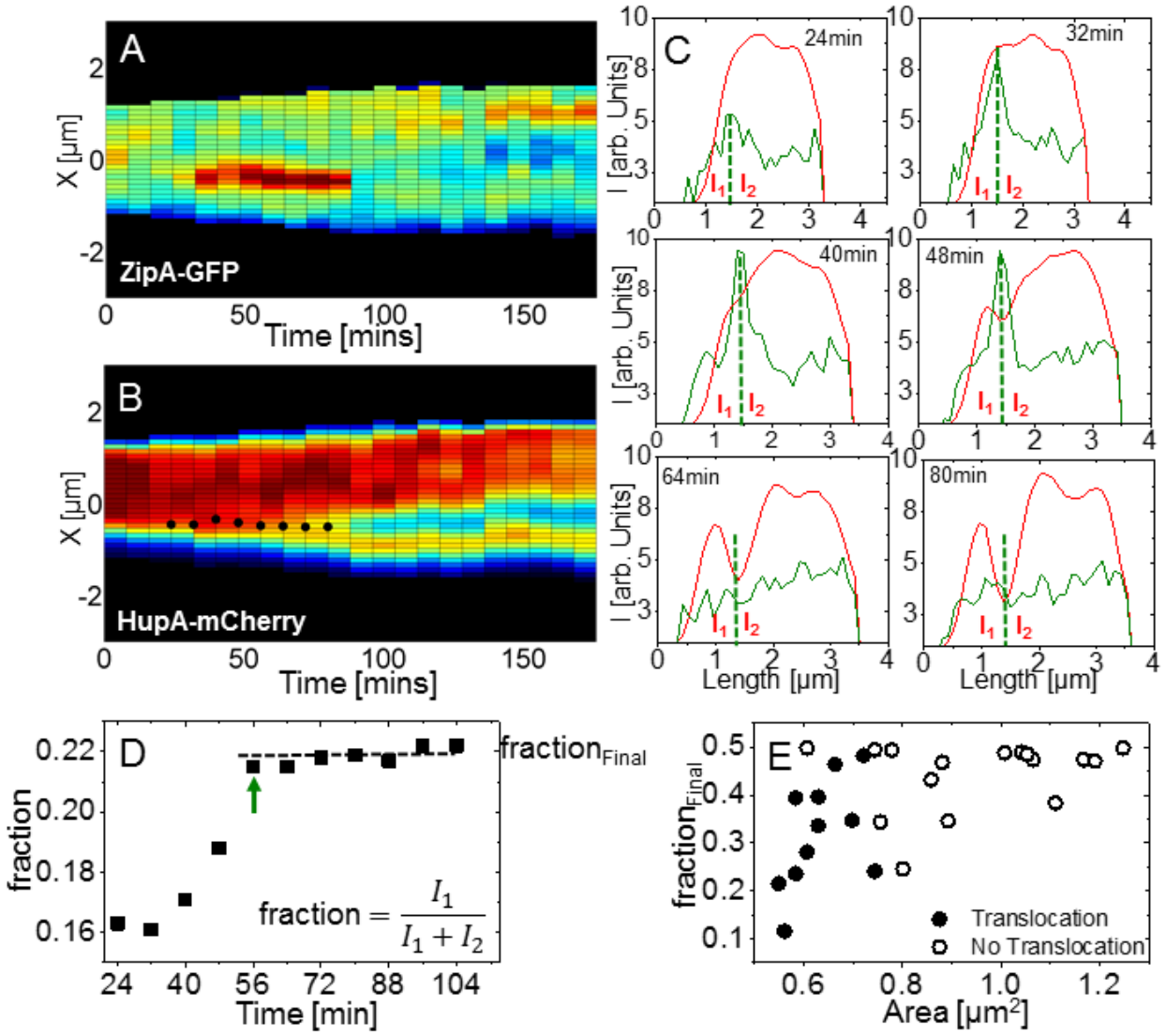

Figure 36. The nucleoid translocates across the septum in asymmetrically dividing ZapB triple deletion cells. (A) Kymograph of ZipA-GFP (Z-ring label) for a Δ*slmA* Δ*minC ΔzapB* cell (strain MB16). Blue corresponds to low and red to high intensity. Black areas are outside the cell. Note this cell is viable (B) Kymograph of HupA-mCherry labeled nucleoid for the same cell. Overlaid black dots show locations of the Z-ring as determined from the data shown on panel (A). (C) The intensity line profiles of the ZipA-GFP (green) and HupA-mCherry (red) at selected time points for the same cell. The vertical dashed lines indicate the location of septum. (D) The fraction of the nucleoid translocated across the septum relative to the total amount of nucleoid material within the cell as a function of time (same cell). The arrow represents the approximate time the ZipA-GFP ring disassembles. (E) Distribution of division events showing translocation (filled circles) or no translocation (empty circles) as a function of nucleoid area and fraction of chromosomal material at the smaller daughter side right after cell division.

The Ter region translocates rapidly through the closing septum in late stages of cytokinesis.

To further confirm the translocation process, we used time-lapse microscopy to monitor simultaneously the replication terminus region and divisome. To label the replication terminus region, we used MatP-mCherry expressed from its native promotor, and inducible ZipA-GFP as a divisome label (Bailey, Bissichia et al. 2014). MatP binds specifically to 23 binding sites on the *E. coli* chromosome located at the replication terminus region within the Ter macrodomain, which spans 400kb in both direction from the *dif* site (Mercier, Petit et al. 2008, Dupaigne, Tonthat et al. 2012). While in wild type (Espeli, Borne et al. 2012) and Δ*slmA* Δ*min* cells the Ter macrodomain and Z-ring co-localize, in ZapA, ZapB, and MatP triple deletion cells no co-localization is present when the Ter linkage is absent (Bailey, Bissichia et al. 2014). In many asymmetrically dividing ZapA and ZapB triple deletion cells, a single MatP-mCherry labelled Ter focus remains localized on one side of the closing septum (Figure 38A-C). Only in very late stages of cell division does the Ter focus split into two. During this splitting, one of the foci moves across the septum (Figure 38C). Interestingly, in many cases we observed the MatP focus split and translocate across the divisome after the ZipA-GFP label had dissociated from the divisome (Figure 38D). However, on average the time difference between splitting of MatP focus ($t_{MatP\ Split}$) and disassembly of ZipA decorated Z-ring (t_Z) was zero for both ZapA ($t_{MatP\ Split} - t_Z = 4 \pm 23$ min; p=0.96) and ZapB ($t_{MatP\ Split} - t_Z = 6 \pm 12$ min; p=0.50) triple deletion cells. Since ZipA is one of the two membrane anchors of FtsZ, the disappearance of ZipA and FtsZ from the septum can be expected to occur simultaneously. As perhaps expected, the Ter region appears to be the last region of the chromosome to be translocated across the closing septum and that this movement occurs just before the division septum closes.

A notable feature of the Ter translocation is the distance it travels (Figure 38C). We found the distance traveled by the Ter region that ended up in the smaller daughter to be 0.90 ± 0.30 μm and 0.77 ± 0.29 μm for the ZapA and ZapB triple deletion *E.coli,* respectively (Figure 38E).

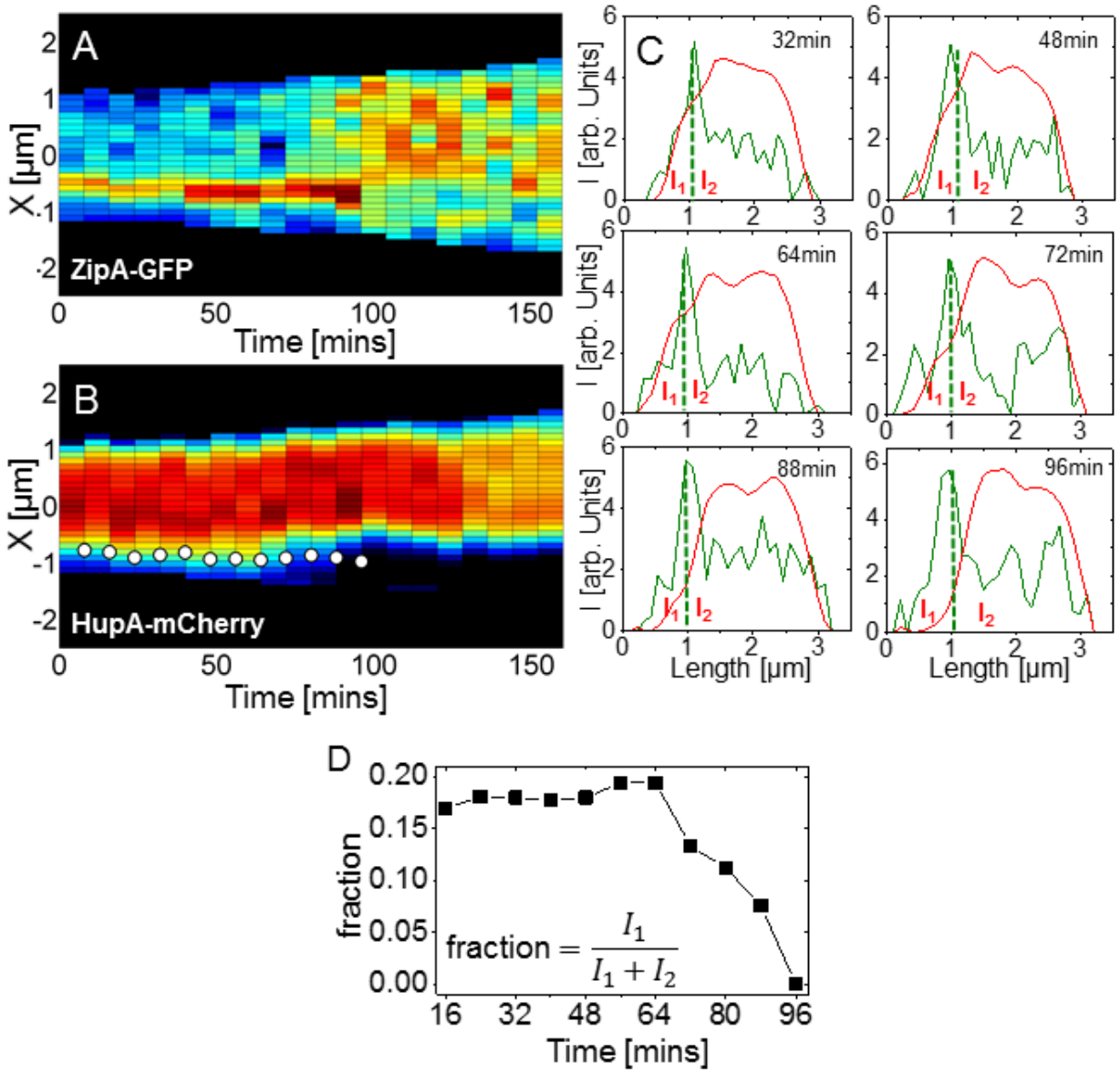

Figure 37. Complete retraction of chromosomal DNA from the smaller daughter. (A) Kymograph of ZipA-GFP (Z-ring label) and (B) HupA-mCherry labeled nucleoid for a triple deletion ZapA cell (strain MB15). Overlaid white dots show locations of the Z-ring as determined from the data shown on panel (A). (C) The intensity line profiles of the ZipA-GFP (green) and HupA-mCherry (red) at selected time points for the same cell. The septum is marked by dashed vertical line. (D) The fraction of the nucleoid material in the smaller daughter's side of the septum as a function of time (same cell).

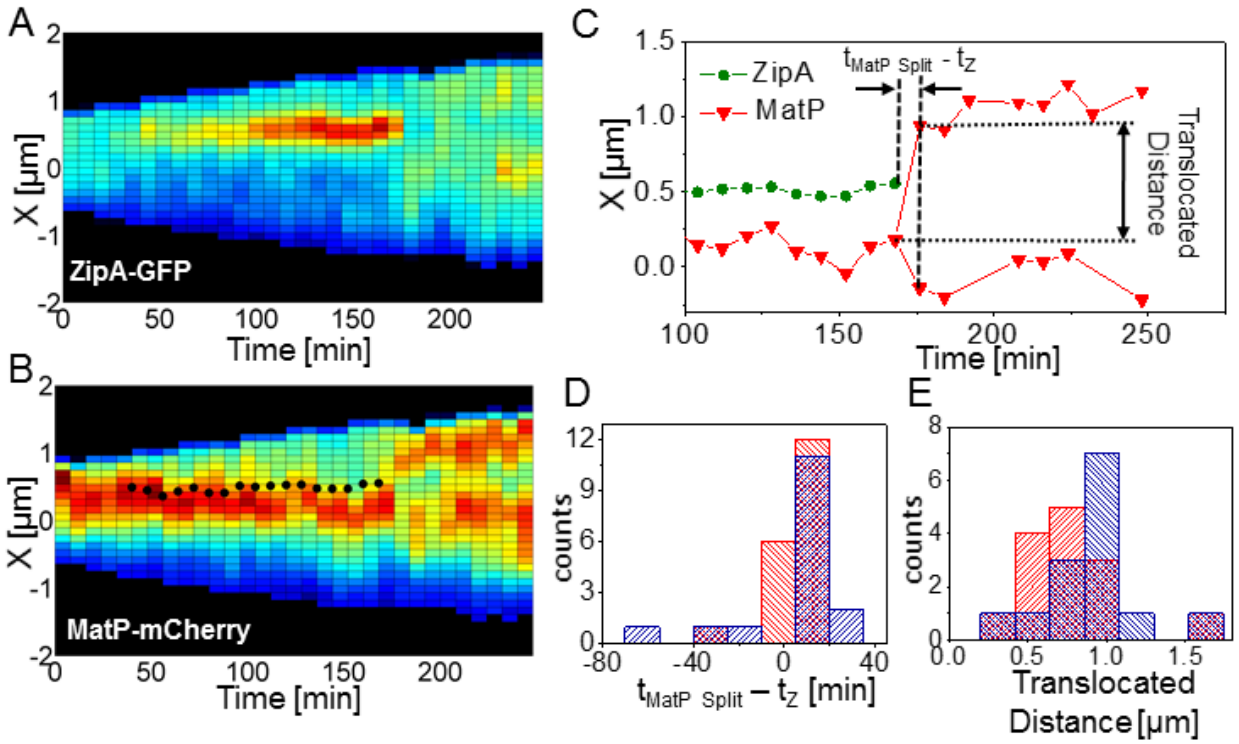

Figure 38. The Ter region translocates across the closing septum just before completion of cytokinesis. (A) Distribution of ZipA-GFP along the cell length as a function of time for a ZapB triple deletion cell (strain MB16). (B) Distribution of MatP-mCherry labeled replication terminus region for the same cell. In the kymographs, blue corresponds to low and red to high intensity. The black data points in panel (B) shows the centroid of the ZipA-GFP signal shown in panel (A). (C) Positions of ZipA-GFP labelled Z-rings (green circles) and MatP-mCherry labeled terminus region (red triangles) as a function of time. (D) Histogram of time differences between the splitting of the MatP focus ($t_{MatP\ Split}$) and the disappearance of ZipA-GFP from midcell (t_Z). (E) Histogram of the distances moved by the terminus region during translocation. In (D) and (E) ZapA triple deletion is represented by blue (N=17 in (D); N=16 in (E)) and ZapB triple deletion by red hatched bars (N=18 in (D); N=19 in (E)).

The distance travelled by the Ter focus is comparable to size of the fully replicated nucleoid in these growth conditions. Taking that the Ter region comprises about 20% of the nucleoid, its fast long-distance movement indicates very rapid changes in the whole chromosomal organization during the translocation process.

FtsK is not required for DNA translocation but cell constriction is.

What biological mechanism can generate such large-scale DNA translocation? *E. coli* like most other bacteria harbor the DNA pump FtsK, which can rapidly move DNA across the septum. Bacterial FtsK is a protein that localizes to the divisome late in the cell cycle and participates in coordinating cell division with the late stages of chromosome segregation (Sherratt, Arciszewska et al. 2010). In particular, the C-terminal domain is a double-stranded DNA pump (called a "translocase") that pulls the replication terminus to the location of the divisome, where it is involved in the process of separating chromosomes that occasionally link together during the segregation process (Sherratt, Arciszewska et al. 2010). Inside the cell, FtsK forms a hexameric assembly (Bisicchia, Steel et al. 2013) that can pump or translocate DNA at a rate of about 5 kb/s and stops when FtsK reaches a specific sequence of terminus DNA known as the dif site (Sherratt, Arciszewska et al. 2010). Although thus far in *E. coli* FtsK has been shown to act only on a 400 kb region around the *dif* site (Deghorain, Pages et al. 2011, Stouf, Meile et al. 2013) (9% of the full chromosome), its analog in *B. subtilis* SpoIIIE can translocate 75% of the mother genome into the forespore (Wu and Errington 1994). Due to the structural similarity between FtsK and SpoIIIE, it is conceivable that FtsK is capable of acting on larger chromosomal regions than only in the immediate vicinity of the *dif* site. To determine if FtsK was responsible for the observed DNA translocation we introduced an FtsK-K997A mutation to both ZapA and ZapB triple deletion strains. The K997A substitution abolishes ATP binding and renders FtsK inactive in DNA pumping (Kennedy, Chevalier et al. 2008).

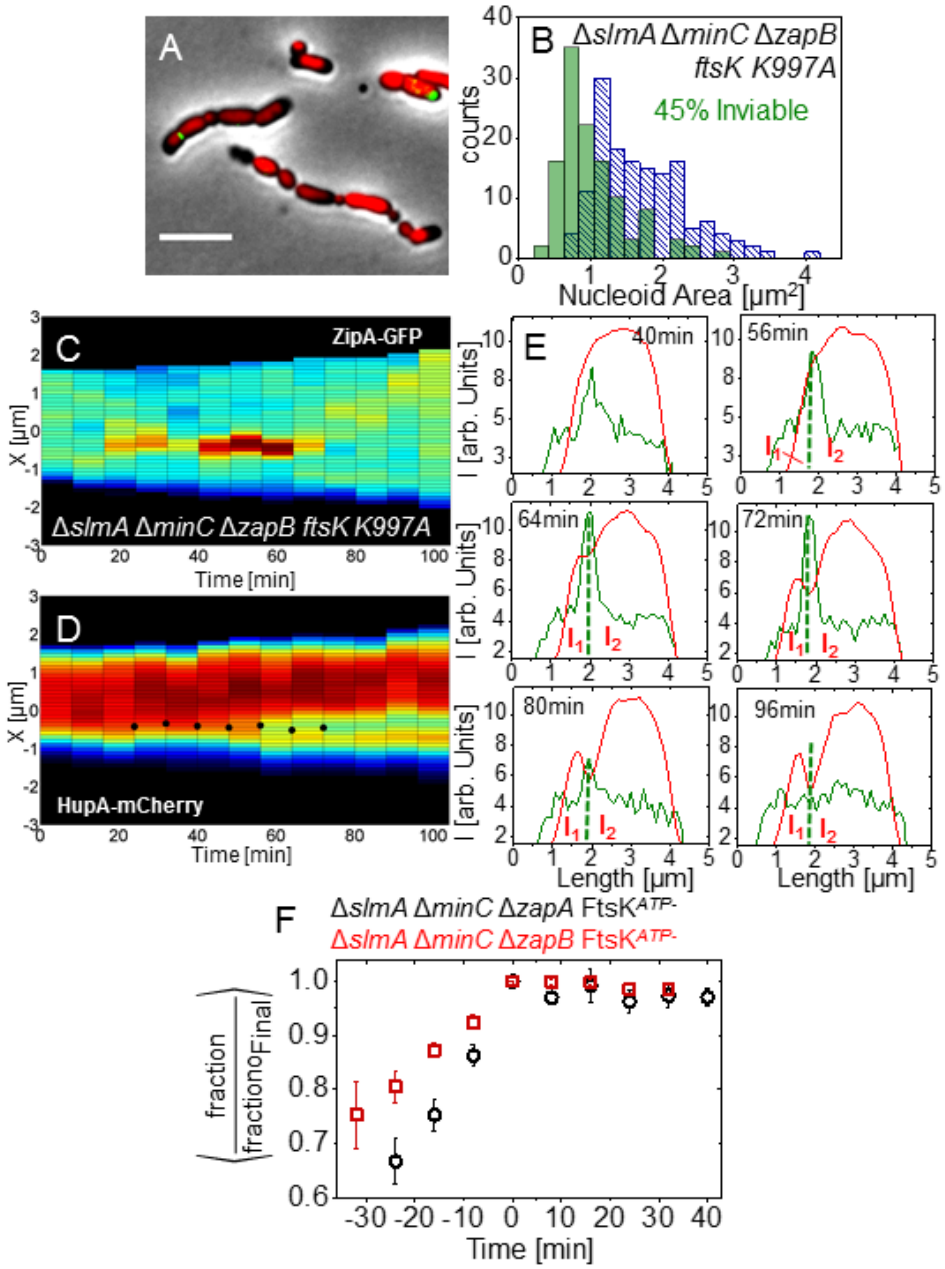

Figure 39. FtsK DNA-pumping activity is not required for observing translocation. (A) Composite of ZipA-GFP (green), DAPI (red), and phase contrast images (gray) of a Δ*slmA* Δ*minC* Δ*zapB* FtsK-K997A *E. coli* (strain MB38). Scale bar is 5 μm. (B) Histograms of nucleoid areas just following cell division for the same strain. Green solid bars correspond to nucleoid areas of inviable and hatched blue bars to viable cells. (C) Kymograph of ZipA-GFP (Z-ring label) and (D) Intensity line profiles for the cell shown in the kymographs (C) and (D). (E) The intensity line profiles of the ZipA-GFP (green) and HupA-mCherry (red) at selected time points for the cell shown in (C) and (D). (F) The population averaged normalized fraction of nucleoid material in the smaller daughter's side of the septum as function of time for a Δ*slmA* Δ*minC* Δ*zapB* FtsK-K997A (squares, N=10) and Δ*slmA* Δ*minC* Δ*zapA* FtsK-K997A cells (circles, strain MB40, N=10). Note that all smaller daughters resulting from these divisions are inviable.

The introduced mutation led to the frequent appearance of long (~10 μm or longer) cells that exhibited multiple constrictions resulting in very unequally and randomly sized septated chains of cells containing correspondingly unequally sized portions of DNA (Figure 39A). Some cells in the chain were very small, <1 μm, in size yet still contained DNA material. Time-lapse imaging of the ZapB triple deletion strain containing the FtsK-K997A mutation revealed that approximately 45% of cells resulting from divisions were inviable (Figure 39B). Unlike the triple deletions strains, the inviable cells in this strain were not exclusively small in size. Unlike smaller inviable cells, larger inviable cells typically did not stop their growth immediately after division but lysed later on. This observation suggests that viability loss in these larger cells may not have resulted from the inheritance of an incomplete genome.

Although the FtsK-K997A mutation in ZapA and ZapB triple deletion cells had a dramatic effect on cell morphology and viability, time lapse imaging showed they were still able to translocate DNA (Figure 39C-F). The translocated DNA amounts were almost indistinguishable for ZapA and ZapB triple deletion cells with the FtsK-K997A mutation (total fraction near 30%) from their triple deletion counterparts (Figure 39F). From this finding, we conclude that FtsK translocase activity is not required for observing rapid DNA movement across the closing septum even though FtsK may contribute to the process. We then hypothesized that perhaps the closing septum itself is responsible for the observed DNA movement by physically pushing chromosome masses apart during division. To test this idea, we treated ZapA and ZapB triple deletion cells with cephalexin to inhibit septal cell wall growth and constriction formation but not assembly of the Z-ring (Pogliano, Pogliano et al. 1997). We monitored cells with Z-rings located near the nucleoid periphery to see if nucleoid profiles revealed any DNA movements across the division plane. Unlike the untreated triple deletion cells, no translocating behavior could be observed in these cells (Figure 40A-D). The fraction of chromosomal mass on either side of the Z-ring relative to the whole chromosomal mass remained essentially constant (Figure 40D), suggesting cells

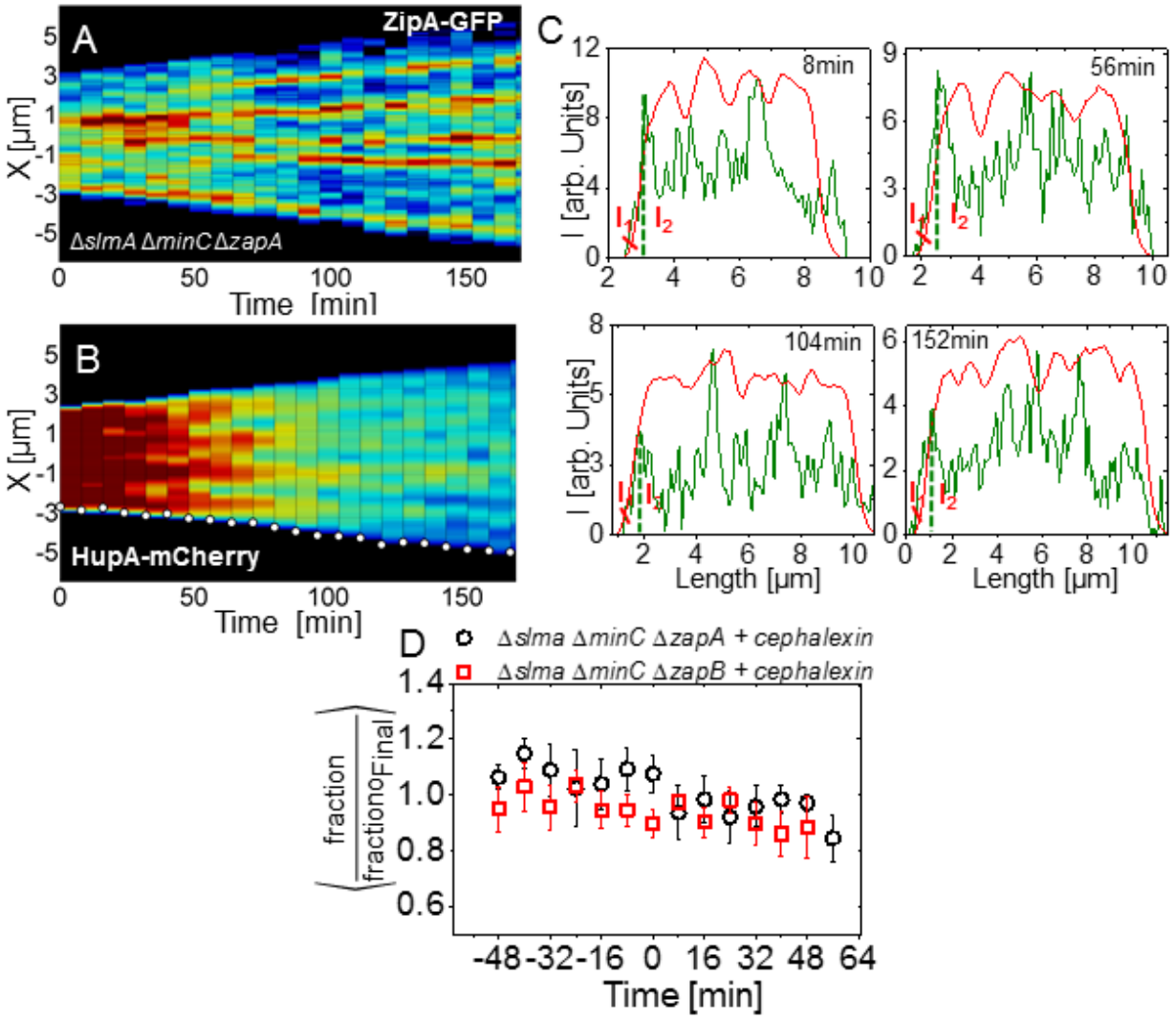

Figure 40. No DNA translocation is observed when septum constrictions are inhibited. (A) and (B) Kymographs of ZipA-GFP and HupA-mCherry, respectively, for a Δ*slmA* Δ*minC* Δ*zapA* cell treated with 50 ug/ml cephalexin to inhibit cell division. (C) Intensity line profiles for the cell shown in (A) and (B). Red traces correspond to HupA-mCherry and green traces to the ZipA-GFP signal. Vertical, dashed line points to the location of peripheral Z-ring. (D) The population averaged normalized fraction of nucleoid material in the smaller daughter's side of the septum as function of time for Δ*slmA* Δ*minC* Δ*zapA* (MB15, N=10) and Δ*slmA* Δ*minC* Δ*zapB* (MB16, N=12) cells. Error bars in (E) are s. e. m.

needed to form constrictions for DNA movement across the division plane to be observable.

Discussion

Removal of *slmA* and *minC* together with *zapA* or *zapB* from the *E. coli* genome results in cells where Z-rings and division planes frequently (40% occurrence) localize over unsegregated nucleoids. In these cells, once the Z-ring forms and matures there appears to be no feedback mechanism present to prevent the septum from constricting over underlying nucleoids. Interestingly, such divisions produce predominantly viable cells (in about 70% of occurrences). High viability of cells from such divisions can be explained by the observed movement of chromosomal DNA across the division plane during late stages of cytokinesis. Such directed movement appears to rescue the chromosomes in all but in the most asymmetric divisions and provides each daughter cell with a complete set of genomic information.

Our estimates suggest that about one third of the chromosome moves across the septum at an average rate of about 770 bp/s in asymmetric divisions. FtsK is a known DNA pump in *E. coli*, which *in vitro* can translocate DNA at rates of 5000 bp/s. Investigation of an FtsK ATPase mutant showed that DNA movement across the division plane can occur even when this DNA pump was disabled, although in the ZapB triple deletion which carried the additional FtsK-K997A mutation, the process appeared to be significantly affected. While FtsK mediates the translocation process and has a significant effect on cell viability, it may effectively pump DNA in *E. coli* only within the 200 kb region flanking the *dif*-site in the replication terminus region as reported earlier (Deghorain, Pages et al. 2011, Stouf, Meile et al. 2013).

The constricting division septum coupled with chromosome fluctuations may drive translocation

FtsK is the only known DNA pump in *E. coli*. How could the nucleoid translocation process occur in cells without this pump? We hypothesize that the constricting division septum coupled

to thermal or non-equilibrium fluctuations in the nucleoid drive the process rather than some dedicated protein machinery (Figure 41). This hypothesis is consistent with the finding that in cephalexin treated cells translocation is absent when there is no constriction formation. The timing of translocation is also indicative that the closing division septum is involved. Most of the translocation occurs in the last stages of cytokinesis when the constricted region is known to rapidly shrink (Reshes, Vanounou et al. 2008). How can constriction cause DNA movement then? As can be seen from time-lapse movies, the constriction physically/sterically separates chromosomal masses from a single chromosome to two daughter compartments. As a result of separation, a restoring force is created that tries to pull these separated chromosomal masses back together. The restoring force is entropic in nature and arises because chromosomal DNA is stretched in the constricted septal region. Of course, the force acts on both DNA masses and therefore could also lead to movement of DNA from the smaller daughter's to the larger daughter's compartment. In a few cases we did indeed observe retractions of DNA. In these cases, the constriction formed over the periphery of the nucleoid capturing initially only a small fraction of the chromosome. Although retractions can be observed, the process clearly carries an entropic penalty because the DNA in the larger daughter's compartment is more confined than if it were distributed between two daughters. Accordingly, there should be an overall tendency for DNA to move towards the compartment of the smaller daughter cell rather than leaving it empty. It is not clear, however, if the resulting entropic force is of a sufficient magnitude to drive chromosomal movement at the observed time scale. Clearly, alternative scenarios cannot be ruled out at this stage. For example, it is possible that the release of cohesive tethers within the replicating chromosome leads to abrupt extrusions along the nucleoid edge (Joshi, Bourniquel et al. 2011) and that the nucleoid shape oscillates on the time scale of tens of seconds (Fisher, Bourniquel et al. 2013). It is possible that these fluctuations are captured by the closing septum. However, we did not observe similar extrusions in cephalexin treated cells but at this stage we cannot rule

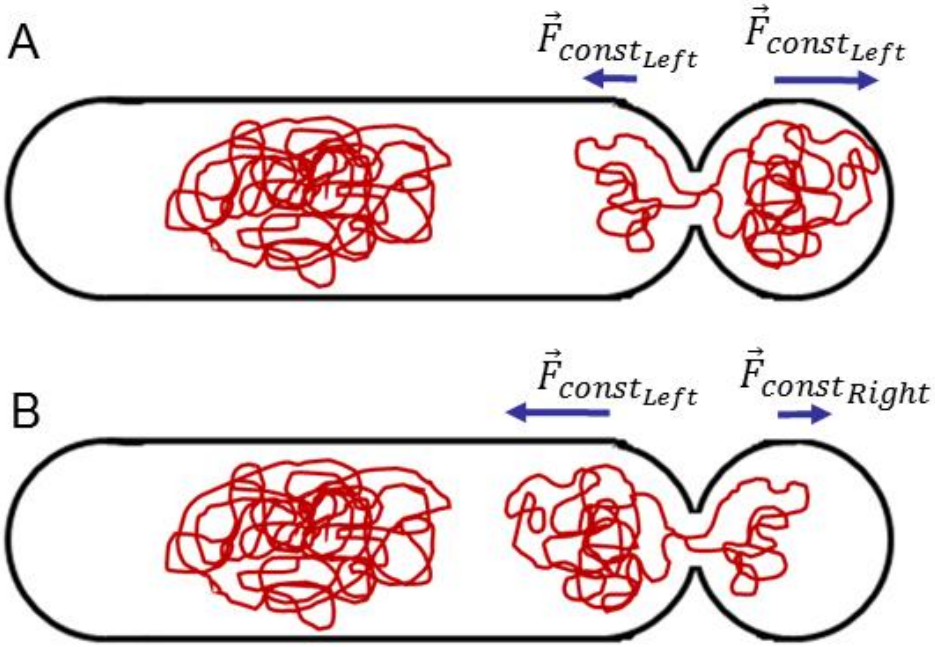

Figure 41. Cell constrictions alone may be sufficient to explain the observed DNA translocation. (A) Schematic of an asymmetric division plane constricting a portion of the chromosomal DNA. If the majority of the chromosome is already within the smaller, asymmetric daughter then perhaps the closing septum could push/pull over the remainder of the chromosome. $\vec{F}$ represents the net force on the chromosome generated by the constricting septum. (B) If the majority of the chromosome is on the side of the larger daughter cell, we expect cell division to produce an anucleate minicell.

out interfering effects of the cephalexin treatment to the release of cohesive tethers and non-equilibrium fluctuations of the nucleoid.

Nucleoid translocation in other bacteria

Such large scale chromosomal movements have been described in sporulating *B. subtilis* where the translocation results from DNA pumping by SpoIIIE (Wu and Errington 1994). In vegetatively growing bacteria, no large scale chromosomal movements have been described yet. However, it has been hypothesized that nucleoid translocation is common in coccal bacteria that lack both the Min and nucleoid occlusion systems (Pinho, Kjos et al. 2013). Our work provides support for this hypothesis and implies that some bacterial species may use nucleoid translocation, either by a dedicated motor protein or by cell constriction alone, as a dominant mechanism to coordinate positioning of chromosomes and cell division proteins.

Chapter 4: Unanswered Questions and the Direction of Future Research

Several questions have been produced as a result of this work, which can become research projects of their own. With regards to the Ter linkage, while it is known that FtsZ binds ZapA, ZapA binds ZapB, and ZapB binds MatP, a physical model of the linkage's structure has only recently been proposed. This structure will be discussed here. Still, an outstanding question is how the Ter linkage forms as a function of time. In other words, in what order do the proteins assemble, in what stoichiometry do these proteins bind each other, and where in the cell does the Ter linkage form?

A closely related question is to what extent does the Ter linkage influence Z-ring formation? Does the Z-ring build, according to the current paradigm, primarily on the membrane independently of the Ter linkage and then once formed, and associated with ZapA and ZapB, connect to the underlying MatP-bound chromosomal terminus? Or, does the MatP-bound terminus, decorated with ZapB, first bind ZapA and then recruit cytosolic FtsZ? It is equally possible that both of these scenarios occur simultaneously, namely that the Z-ring forms from the membrane "down", and from the cytosol near the terminus "up" toward the membrane, and realizes the connection by meeting in the middle.

A different but equally interesting question is why do we not see VENO in slow growing Δ*slmA* Δ*minC E. coli*? Similarly, why do we see nucleoid occlusion in Δ*slmA* Δ*minC* Δ*matP E. coli* but not in the Δ*slmA* Δ*minC* Δ*zapA* or Δ*slmA* Δ*minC* Δ*zapB* strains? Is it possible that a mechanism akin to our original VENO hypothesis is responsible for the exclusion of the Z-ring from the regions of the cell occupied by the nucleoid in Δ*slmA* Δ*minC* Δ*matP* cells?

With respect to large-scale chromosome rearrangement, the question of how the closing septum mechanistically translocates the DNA remains. Is the force which seems to pull the DNA

into the asymmetrically dividing daughter cell purely entropic in nature, or are there other unknown pulling forces that arise from septal cell wall synthesis?

Lastly, because in slow growth conditions neither the Min system, SlmA-mediated nucleoid occlusion, or the Ter linkage are strictly essential in *E. coli*, we are left with the fundamental question "What are the minimal requirements for coordination between divisome formation and chromosome replication/segregation?"

Though we have yet to perform experiments on all these questions, we have begun experiments to understand the time-dependent formation of the Ter linkage, as well as to understand whether or not the Ter linkage influences Z-ring formation. In addition to these preliminary results, I will present an argument regarding the apparent absence of VENO in slow growing Δ*slmA* Δ*min E. coli*, as well as the minimal requirements for coordination between divisome formation and chromosome replication/segregation.

How is the Ter linkage structurally and dynamically formed?

Timelapse microscopy of fluorescently labeled ZapA, ZapB, and FtsZ showed that ZapA and ZapB are both recruited early to the Z-ring as both ZapA and ZapB colocalized with FtsZ from approximately the time the Z-ring formed at midcell (Galli and Gerdes 2010). By forming 3D reconstructions of deconvoluted images, Galli and Gerdes were able to show that ZapB formed what appeared to be a ring-like structure inside the Z-ring, while ZapA, which also forms a ring-like structure, has a diameter that is indistinguishable from that of the Z-ring. Furthermore, they showed that ZapB colocalization to the Z-ring was lost when ZapA was removed (Galli and Gerdes 2010). Earlier *in vitro* studies showed that in the presence of ZapA, FtsZ formed large cable like structures (Low, Moncrieffe et al. 2004), and that similar *in vitro* studies showed that ZapB self-assembled into similar large cable-like structures (Ebersbach, Galli et al. 2008). Due to the ability of ZapA to colocalize with FtsZ and support the self-organization of ZapB ring-like structure, the model that emerged is one where ZapA and ZapB increase Z-ring stability by connecting

smaller clusters of FtsZ filaments (Galli and Gerdes 2012, Buss, Coltharp et al. 2013). This idea was supported by observations of abnormal septa in cells lacking only ZapA or ZapB. Interestingly, removal of ZapA or ZapB did not affect the arrival of subsequent divisome proteins, nor did it stop cells diving in an otherwise wild-type manner (Buss, Coltharp et al. 2013). Nevertheless, despite the discovery that ZapB interacts with replication terminus binding protein MatP, and in the presence of ZapA localized at midcell (Espeli, Borne et al. 2012), a complete structure of the Ter-linkage was only recently proposed.

By using single-molecule based super-resolution imaging techniques (PALM and iPALM), Buss et al. quantified the spatial arrangement of FtsZ, ZapA, ZapB, and MatP and found together they form a large, multi-layered network which extends from the membrane to the Ter region of the chromosome. In addition to showing the Z-ring was composed of a heterogeneous and punctate arrangement of FtsZ clusters, which were displaced away from the cytoplasmic face of the inner membrane by approximately 13nm, they showed that ZapA adopted a similar heterogeneous, punctate clustered arrangement. ZapB, on the other hand, was found to form a wider, larger, and more cohesive structure that was displaced about 40nm inside (toward the cell center) of the FtsZ and ZapA structure, consistent with previous live cell, fluorescence microscopy results (Galli and Gerdes 2010). Interestingly, MatP was observed to form clusters of its own with an average diameter of approximately 100nm located a further 30nm inside the ZapB structure. With respect to the cell center, the MatP structure was displaced approximately 280nm radially outward (Buss, Coltharp et al. 2015). A visual summary of their work is illustrated in Figure 42.

Care must be given, however, to any subcellular structures determined from super resolution since the technique requires a cell's internal substructures to be "fixed" in place, preserving them from decay or destruction. Consequently, the process of fixing cells kills them. Images acquired in this way are only valid if the fixation method accurately captures the internal structures as they existed when the cell was alive. Unfortunately, cell fixation can alter substructures and therefore introduce artifacts (Huang, Bates et al. 2009). When possible, super-

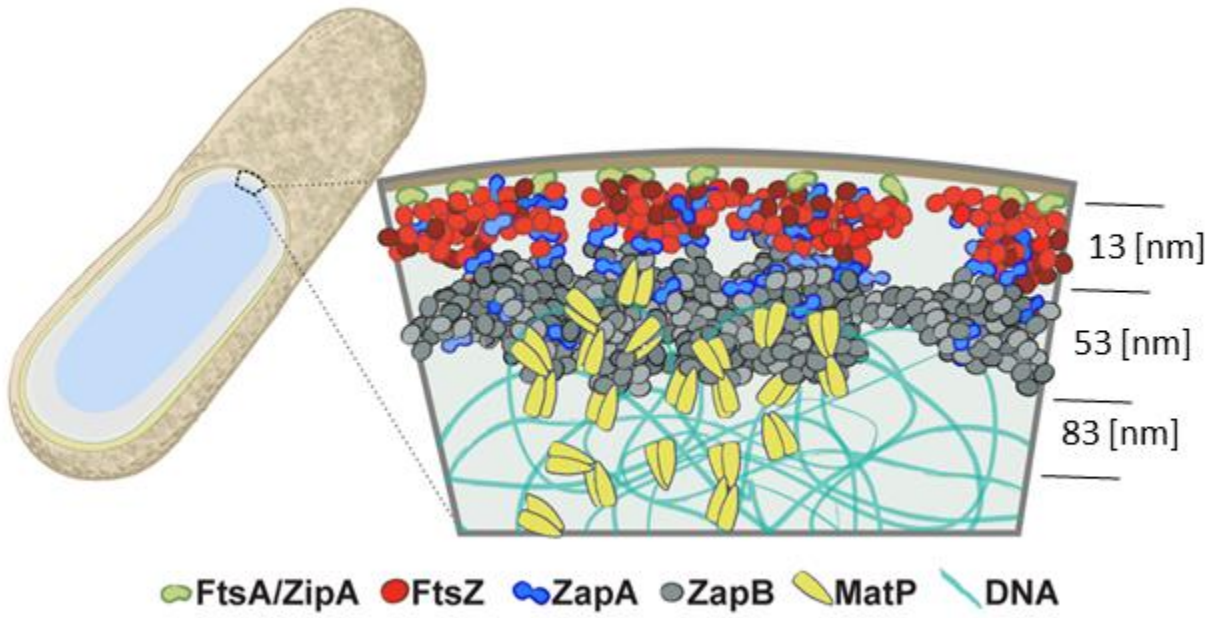

Figure 42. Schematic illustration of the multi-layered organization of the FtsZ-ZapA-ZapB-MatP macrostructure in *E. coli* by (Buss, Coltharp et al. 2015). The FtsA (green) and ZipA (orange) proteins tether the punctate FtsZ (red) ring to the inner plasma membrane. ZapA (blue) is arranged similarly to FtsZ. Deviation of ZapA from FtsZ may result from interactions with ZapB or other membrane proteins. ZapB (grey) forms the structure that extends most into the cytosol, and associates with FtsZ indirectly through ZapA. ZapB also associates with DNA-bound MatP (yellow). Schematic adapted from (Buss, Coltharp et al. 2015).

resolution results should be substantiated with other independent experiments such as live cell microscopy, or immunofluorescence microscopy.

Fortunately, recent live cell microscopy results seem to support the PALM and iPALM results. Mannik et al. demonstrated that MatP can assume an extended, or elongated formation along the short axis of the cell at the location of the divisome (Mannik, Castillo et al. 2016). Instead of creating a uniform, annular distribution, MatP was observed to make only limited attachments with the divisome, suggesting that the Ter linkage is only fully realized along certain subregions, or along certain arcs, of the divisome. As expected, when ZapA or ZapB were removed, MatP elongation along the lateral direction markedly decreased (Mannik, Castillo et al. 2016).

Despite the insight gained into the physical structure of the Ter linkage, the time-dependent behavior of the Ter-linkage, namely how the network is constructed as a function of the cell cycle, is unknown. Though the PALM technique offers enhanced spatial resolution, it is not a technique easily applicable to timelapse imaging. A straightforward series of experiments to gain insight into the time-dependent behavior of the FtsZ-ZapA-ZapB-MatP network would be to label pairs of proteins, e.g., FtsZ – ZapA, ZapA – ZapB, and ZapB – MatP, and monitor their respective colocalization as a function of time. Though the project remains in its infancy, we have begun such a series of experiments. Thus far, we have constructed strain RH14 which is a wild-type *E. coli* strain having ZapB-GFP and MatP-mCherry protein fusions. From static images (Figure 43A-D), we find that whether MatP is located in the center of the nucleoid, or at the nucleoid periphery (indicative of an early stage of the cell cycle), ZapB and MatP were found to colocalize in every cell observed (N=105) (Figure 43E). While the colocalization accuracy was approximately the same as the colocalization accuracy between ZipA and MatP (Figure 43F), interestingly no ZapB was found at midcell when MatP was located at a pole. This observation differs from the colocalization pattern between ZipA-GFP and MatP-mCherry labels where occasionally Z-rings were found to localize at midcell when MatP was located at the nucleoid

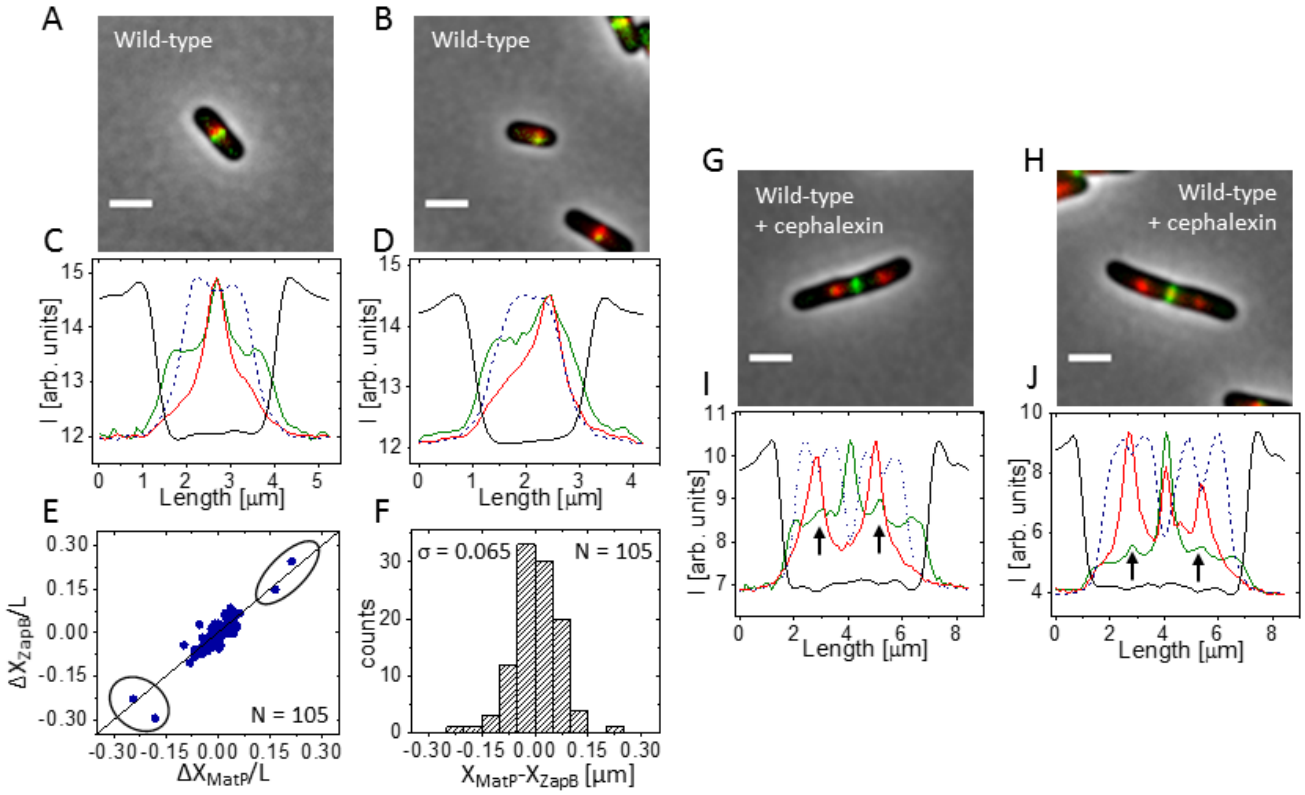

Figure 43. ZapB colocalizes with MatP even when MatP is located at the nucleoid periphery. (A), (B) Composite of ZapB-GFP (green), MatP-mCherry (red), and phase contrast images (gray) of an otherwise wild-type *E. coli* (strain RH14) (C), (D) The intensity line profiles of the ZapB-GFP (green), MatP-mCherry (red), nucleoid-labeled by DAPI (blue), and phase constrast cell contour (black) for the cells in (A) and (B), respectively. (E) Displacements of ZapB-GFP relative to the cell center, ΔX_{ZapB}, as a function of the MatP-focus displacement from the cell center, ΔX_{MatP}. All displacements are normalized by cell length *L*. The solid line corresponds to $\Delta X_{ZapB}=\Delta X_{MatP}$. The circled data points represent cells which have MatP foci located at the nucleoid perihery for which ZapB is colocalized. (F) Histogram of distances between MatP-mCherry and ZapB-GFP. (G), (H) Composite of ZapB-GFP (green), MatP-mCherry (red), and phase contrast images (gray) of an otherwise wild-type *E. coli* treated with cephalexin (strain RH14). (I), (J) The intensity line profiles of the ZapB-GFP (green), MatP-mCherry (red), nucleoid-labeled by DAPI (blue), and phase constrast cell contour (black) for the cells in (G) and (H), respectively. The arrows represent small ZapB accumulations that colocalize with MatP-foci located away from the cell center. All scale bars are 2μm.

periphery (Figure 17). This observation suggest that ZapB may decorate MatP rather than the ZapA-bound Z-ring, at least at early stages of the cell cycle. If so, then ZapB might build from the cytosol toward the membrane. To test this idea further, we treated the RH14 strain with cephalexin to inhibit septal cell wall synthesis and prevent the formation of constrictions. In wild-type *E. coli* treated with cephalexin that are less than about 10μm long, usually only one Z-ring is present at midcell. If we observed ZapB to accumulate with MatP which had split and moved to the centers of the replicated nucleoids while the Z-ring remained at the cell center, this observation would further indicate that ZapB decorates MatP even in the absence of the Z-ring. This observation would provide further evidence that ZapB might build from the cytosol and connect later to the forming membrane-proximal Z-ring. Though the majority of ZapB was found in the center of cephalexin-treated cells at the location of the Z-ring, essentially all MatP foci which had replicated and moved to the centers of sister nucleoids were accompanied by smaller accumulations of ZapB (Figure 43G-J). Smaller ZapB accumulations at MatP foci relative to the ZapB accumulation at the central Z-ring is reasonable since each MatP focus is composed of about 40 MatP proteins for ZapB to bind to. In comparison, a much larger number of Z-ring bound ZapA proteins are available to bind ZapB. Taken together, these results suggest that ZapB can decorate MatP foci in the absence of the Z-ring, implying that the ZapB-bound terminus could serve as a Velcro-like cluster that, under DNA fluctuations which bring the DNA close to the membrane, can “stick” to the FtsZ-ZapA clusters composing the Z-ring.

In addition to static images, we performed timelapse microscopy on the ZapB-GFP, MatP-mCherry labeled wild-type *E. coli*. As suggested by the static images, throughout the cell cycle, we observed ZapB colocalize with MatP. At the beginning of the cell cycle, when MatP moved from the pole of the daughter cell to the cell center, ZapB followed (Figure 44). In some cases, MatP was observed to move more diffusely from the pole to the cell center, often moving back toward the pole of the cell before settling in at midcell later in the cell cycle. In these cases, ZapB

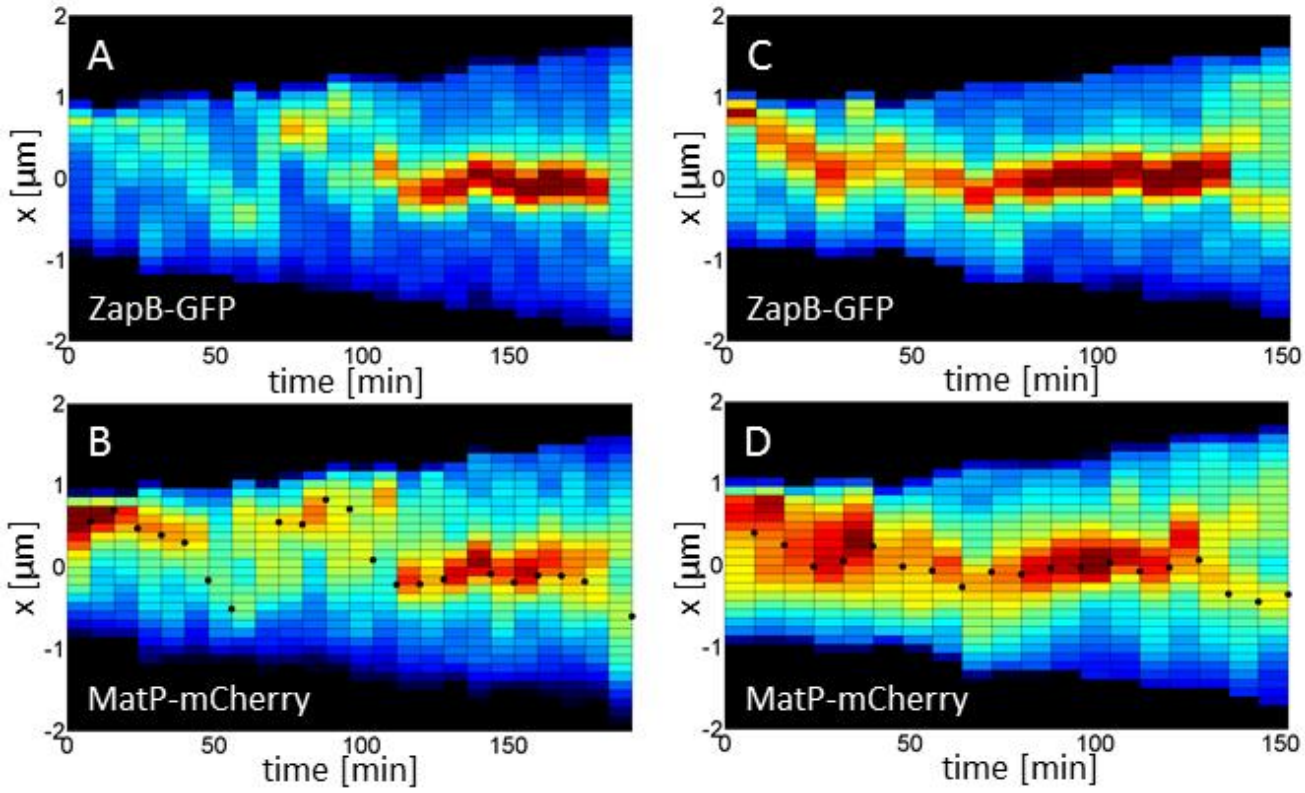

Figure 44. ZapB colocalizes with MatP throughout the cell cycle. (A) Kymograph of ZapB-GFP and (B) MatP-mCherry for a wild-type *E. coli* cell (strain RH14). Blue corresponds to low and red to high intensity. Black areas are outside the cell. Overlaid black dots show locations of ZapB-GFP as determined from the data shown on panel (A). Note, after ZapB splits, only the lower branch is followed here. (C) Kymograph of ZapB-GFP and (D) MatP-mCherry for another wild-type *E. coli* cell.

also adopted the same diffuse, and occasionally jumpy pattern (Figure 44A, B). At the end of the cell cycle, when MatP replicated and split, ZapB was observed to split at approximately the same time (Figure 44A-D). Though more analysis needs to be performed to characterize the timing between MatP-splitting and the subsequent ZapB-splitting, the preliminary results suggest that ZapB decorates MatP throughout the entire cell cycle, raising the possibility that the FtsZ-ZapA-ZapB-MatP network may be partially present throughout the cell cycle.

Why did we fail to see VENO in Δ*slmA* Δ*min E. coli*?

FtsZ filaments have not been directly observed diffusing through the cytosol. However, *in vitro*, FtsZ monomers polymerize into filaments at a critical concentration between 0.5μM - 1μM (Adams and Errington 2009). Interestingly, the estimated concentration of FtsZ in *E. coli* ranges between 4μM - 7μM, depending on the strain (Erickson, Anderson et al. 2010), suggesting FtsZ should exist as filaments *in vivo* (*in vivo*, see Appendix Glossary). Nevertheless, it is possible that filaments do not exist inside bacteria. Alternatively, even if filaments are present *in vivo*, it is possible that VENO is not sufficient to position Z-rings. It is plausible that filaments are excluded from nucleoids, consistent with the estimation presented here, and yet filaments lack a signal that triggers their coordinated polymerization at one location. If true, filaments, though expelled from the nucleoid, would diffuse through the surrounding cytosol without forming a Z-ring.

What are the minimal requirements for divisome-chromosome coordination in bacteria?

An overarching question, not only in our lab but throughout bacterial cell biology, is what are the minimum requirements for a system to provide sufficient coordination between cell division and chromosome segregation so that cell division produces two viable cells? The following argument has been presented in our review (Männik and Bailey 2015), and suggests that if cells are sufficiently large, perhaps no coordination is needed at all.

Remarkably, neither the Min system, SlmA-mediated nucleoid occlusion, nor the Ter linkage is strictly essential in *E. coli*. Moreover, even though FtsK is essential, its DNA translocating domain (C-terminal domain) is not (Sherratt, Arciszewska et al. 2010). Is it possible that *E. coli* harbors some additional molecular system(s) that coordinates its divisome and chromosome, and this yet to be discovered system is indispensable? As demonstrated particularly with the Δ*slmA* Δ*min* Δ*matP* triple deletion *E. coli* strain, there is strong evidence that the NO effect can occur without SlmA. Although the molecular bases of this mechanism remains unknown it could be an essential mechanism for some bacteria. It is also possible that early protocells might have had mechanisms that provided some coordination between division planes and chromosomes but which were not specifically dedicated for the task. For example, in rod-shaped bacteria cell membrane mechanics dictates that divisions which partition a mother cell into two equal halves are energetically more favorable than asymmetric divisions (Shlomovitz and Gov 2009). Also, as we have observed in Δ*slmA* Δ*min* Δ*zapA* and Δ*slmA* Δ*min* Δ*zapB E. coli,* it is likely that chromosomes could be pushed mechanically away as the division septum closes preventing them from being guillotined. Depending upon the rigidity of early bacteria's cell wall, it is possible the chromosomes could have provided enough mechanical hindrance to prevent the septum from closing. These mechanisms could still be present in modern *E. coli* even though their influence is overridden by the more efficient molecular systems such as Min, SlmA, and the Ter linkage.

Alternatively, it is possible that there are no indispensable mechanisms that coordinate cell division and chromosome segregation in *E. coli*. For propagation of a sizeable cell population, the ultimate limit appears to be that on average more than half of the nucleoids need to survive cell division undamaged, and emerge in newborn daughter cells (note that small cell populations can go extinct even when more than half of the nucleoids survive cell division). One way to fulfill this requirement in cells that lack any dedicated coordination mechanism between cell division and chromosomes is to increase cell size. If the division plane is placed randomly in the cell then

the probability to produce viable daughter cells increases as the cell size increases (Figure 45). Mutli-nucleoid cells are more likely to produce two viable daughters upon random placement of the division plane at the expense of losing some genetic material (Figure 45). However, in rod-shaped bacteria, cells with two nucleoids also can give rise to a viable population when their sizes are sufficiently large. In the latter case, the assumption is that the physical size of the nucleoid does not depend on cell size, and nucleoids are also randomly placed in the cell before division. It also remains to be proven if viable populations can emerge in other cell geometries under these assumptions. Interestingly, as the cell division protein positioning systems are progressively deleted from *E. coli,* the cells become larger (longer) but remain viable in slow growth conditions (Bailey, Bissichia et al. 2014) in accordance with this hypothesis. From this reasoning, we may predict early protocells were perhaps larger than present day bacteria.

Although large cells can cope with random placement of division planes, at least in rod shapes, their fitness is very low because these cells lose a substantial amount of resources when they produce unviable cells or guillotined nucleoids. Contrary to being essential for viable cell progeny, the mechanisms that coordinate cell division proteins and chromosomes are therefore essential for cellular fitness. These mechanisms are highly efficient in modern bacteria. The probability that wild type *E. coli* produces minicells has been estimated to be less than 0.03% (Niki, Jaffe et al. 1991). This argument is supported further by findings that different bacterial species have evolved very different molecular mechanisms that coordinate divisomes and chromosomes (Monahan, Liew et al. 2014).

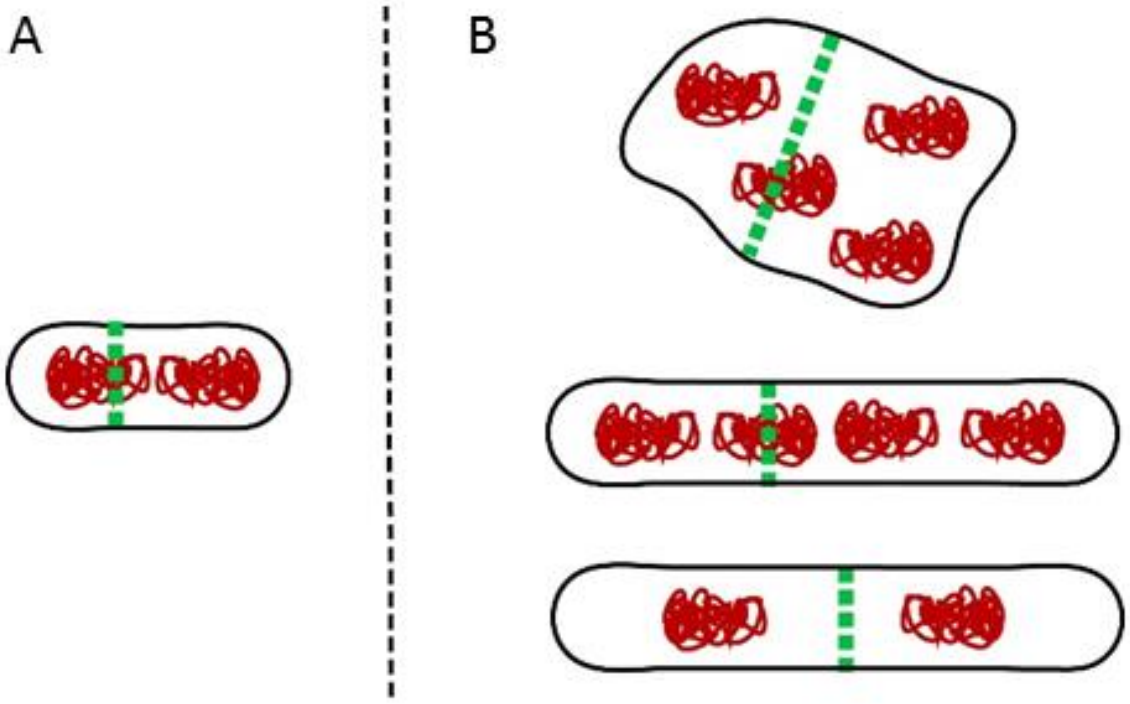

Figure 45. Larger cell size mitigates the lack of spatial coordination between cell division machinery and genetic information from (Männik and Bailey 2015)**.** (A) A small cell (left) requires sophisticated apparatus to coordinate cell division and chromosomes. (B) For larger cells (right) the requirements for coordination are much more relaxed. This applies even for multi-nucleoid cells. Some of the genetic material of multi-nucleoid cell may become damaged during division but the daughter cells still may remain viable. Figure from (Männik and Bailey 2015).

Conclusion

This dissertation set out to find a common physical mechanism for how cell division proteins could localize in modern bacterial cells, and perhaps in early protocells also. Modern bacteria have developed a variety of different molecular systems that are involved in this positioning. Our strategy consisted of removing known positioning systems and monitoring the subsequent effect on protein localization. Originally, we hypothesized that excluded volume interactions between FtsZ filaments and supercoiled DNA branches would lead to FtsZ filament expulsion from the nucleoid (VENO). Accordingly, the Z-ring should preferentially form away from the nucleoid, either at the cell poles or within the space between segregated nucleoids. Though the VENO hypothesis failed to explain Z-ring positioning in slow growing Δ*slmA* Δ*min E. coli*, we found two additional molecular mechanisms that coordinate positioning of the chromosome and cell division proteins.

The first mechanism revealed itself in cells having both the Min system and the SlmA proteins removed. In these cells, we showed that division planes colocalized with the centers of nucleoids. Furthermore, we determined this nucleoid-centric signal originated from the Ter region of the chromosome, and identified the involvement of ZapA, ZapB, and MatP proteins. Removal of either ZapA, ZapB, or MatP significantly affected the accuracy and precision with which the Z-ring localized over nucleoid centers, and often lead to misplaced Z-rings. It is possible, however, that additional proteins are present in the Ter linkage that have yet to be found. Contrary to the Min system and SlmA proteins, the Ter linkage is the first positioning system for division proteins in *E. coli* that promotes, rather than inhibits, the placement of the division plane.

The second mechanism was revealed in cells where Z-rings were strongly misplaced relative to chromosomes. Interestingly, most of these cells were still viable. We determined that cells retained their viability because as much as 1/3 of the chromosome moved across the closing division plane in the late stages of cytokinesis. Consequently, this mechanism rescued most

sister chromosomes from being guillotined. Chromosome repositioning appears to rely on septal cell wall synthesis rather than on DNA translocase activity. Such large scale chromosomal movements during cell division has not been described previously in vegetatively growing bacteria (vegetative growth, see Appendix Glossary). The second mechanism also challenges the commonly held view that coordination between division plane placement and chromosome segregation is realized primarily through the Min system and the bacterial nucleoid (either by nucleoid occlusion or the Ter linkage). Lastly, this mechanism suggests that cell constriction alone may be sufficient to coordinate the positioning of chromosomes relative to the cell division proteins. If true, constriction-mediated coordination may have been an important, if not a prevalent factor, for cell division in early bacteria that lacked dedicated coordination systems.

This work has left us with several outstanding questions. Though we now know the Ter-linkage promotes Z-ring localization at nucleoid centers, we still do not understand how the linkage dynamically forms. Furthermore, though we know the divisome can reorganize large fractions of the chromosome, we do not have a mechanistic understanding of the process. How can septal cell wall synthesis carry out directed movement of the chromosome so that asymmetrically dividing daughter cells inherit complete chromosomes versus guillotined ones? Despite these questions, this work has left us with a deeper understanding of the robustness of modern bacteria and the degree of redundancy they possess to achieve proper coordination between cell division protein placement and chromosome segregation.

References

Adams, D. W. and J. Errington (2009). "Bacterial cell division: assembly, maintenance and disassembly of the Z ring." Nature Reviews Microbiology **7**(9): 642-653.

Adler, H. I., et al. (1967). "Miniature *Escherichia coli* cells deficient in DNA." Proceedings of the National Academy of Sciences of the United States of America **57**(2): 321-326.

Akerlund, T., et al. (2002). "Effects of the Min system on nucleoid segregation in *Escherichia coli*." Microbiology-Sgm **148**: 3213-3222.

Baba, T., et al. (2006). "Construction of *Escherichia coli* K-12 in-frame, single-gene knockout mutants: the Keio collection." Molecular Systems Biology **2**: 1-11.

> We have systematically made a set of precisely defined, single-gene deletions of all nonessential genes in Escherichia coli K-12. Open-reading frame coding regions were replaced with a kanamycin cassette flanked by FLP recognition target sites by using a one-step method for inactivation of chromosomal genes and primers designed to create in-frame deletions upon excision of the resistance cassette. Of 4288 genes targeted, mutants were obtained for 3985. To alleviate problems encountered in high-throughput studies, two independent mutants were saved for every deleted gene. These mutants-the 'Keio collection'-provide a new resource not only for systematic analyses of unknown gene functions and gene regulatory networks but also for genome-wide testing of mutational effects in a common strain background, E. coli K-12 BW25113. We were unable to disrupt 303 genes, including 37 of unknown function, which are candidates for essential genes. Distribution is being handled via GenoBase (http://ecoli.aist-nara.ac.jp/).

Bachmann, B. J. (1972). "PEDIGREES OF SOME MUTANT STRAINS OF ESCHERICHIA-COLI K-12." Bacteriological Reviews **36**(4): 525-557.

Bailey, M. W., et al. (2014). "Evidence for divisome localization mechanisms independent of the Min system and SlmA in *Escherichia coli*." Plos Genetics **10**: e1004504.

Berg, R. D. (1996). "The indigenous gastrointestinal microflora." Trends in Microbiology **4**(11): 430-435.

Bernhardt, T. G. and P. A. J. de Boer (2005). "SlmA, a nucleoid-associated, FtsZ binding protein required for blocking septal ring assembly over chromosomes in *E. coli*." Molecular Cell **18**(5): 555-564.

Bertani, G. (2004). "Lysogeny at mid-twentieth century: P1, P2, and other experimental, systems." Journal of Bacteriology **186**(3): 595-600.

Bi, E. and J. Lutkenhaus (1991). "FtsZ ring structure associated with division in *Escherichia coli*." Nature **354**(6349): 161-164.

Bisicchia, P., et al. (2013) The N-terminal membrane-spanning domain of the *Escherichia coli* DNA translocase FtsK hexamerizes at midcell. Mbio **4**, DOI: 10.1128/mBio.00800-13

Bonny, M., et al. (2013) Membrane Binding of MinE Allows for a Comprehensive Description of Min-Protein Pattern Formation. Plos Computational Biology **9**, DOI: 10.1371/journal.pcbi.1003347

Buss, J., et al. (2013). "In vivo organization of the FtsZ-ring by ZapA and ZapB revealed by quantitative super-resolution microscopy." Molecular Microbiology **89**(6): 1099-1120.

Buss, J., et al. (2015). "A Multi-layered Protein Network Stabilizes the Escherichia coli FtsZ-ring and Modulates Constriction Dynamics." PLoS genetics **11**(4): e1005128-e1005128.

Buss, J., et al. (2015). "A Multi-layered Protein Network Stabilizes the Escherichia coli FtsZ-ring and Modulates Constriction Dynamics." Plos Genetics **11**(4).

> The prokaryotic tubulin homolog, FtsZ, forms a ring-like structure (FtsZ-ring) at midcell. The FtsZ-ring establishes the division plane and enables the assembly of the macromolecular division machinery (divisome). Although many molecular components of the divisome have been identified and their interactions extensively characterized, the spatial organization of these proteins within the divisome is unclear. Consequently, the physical mechanisms that drive divisome assembly, maintenance, and constriction remain elusive. Here we applied single-molecule based superresolution imaging, combined with genetic and biophysical investigations, to reveal the spatial organization of cellular structures formed by four important divisome proteins in E. coli: FtsZ, ZapA, ZapB and MatP. We show that these interacting proteins are arranged into a multi-layered protein network extending from the cell membrane to the chromosome, each with unique structural and dynamic properties. Further, we find that this protein network stabilizes the FtsZ-ring, and unexpectedly, slows down cell constriction, suggesting a new, unrecognized role for this network in bacterial cell division. Our results provide new insight into the structure and function of the divisome, and highlight the importance of coordinated cell constriction and chromosome segregation.

Cambridge, J., et al. (2014). "A replication-inhibited unsegregated nucleoid at mid-cell blocks Z-ring formation and cell division independently of SOS and the SlmA nucleoid occlusion protein in *Escherichia coli*." Journal of Bacteriology **196**(1): 36-49.

Chen, I. A. and P. Walde (2010). "From Self-Assembled Vesicles to Protocells." Cold Spring Harbor Perspectives in Biology **2**(7).

Chen, Y. D., et al. (2005). "A rapid fluorescence assay for FtsZ assembly indicates cooperative assembly with a dimer nucleus." Biophysical Journal **88**(1): 505-514.

Cherepanov, P. P. and W. Wackernagel (1995). "GENE DISRUPTION IN ESCHERICHIA-COLI - TCR AND KM(R) CASSETTES WITH THE OPTION OF FLP-CATALYZED EXCISION OF THE ANTIBIOTIC-RESISTANCE DETERMINANT." Gene **158**(1): 9-14.

Two cassettes with tetracycline-resistance (Tc-R) and kanamycin-resistance (Km(R)) determinants have been developed for the construction of insertion and deletion mutants of cloned genes in Escherichia coli. In both cassettes, the resistance. determinants are flanked by the short direct repeats (FRT sites) required for site-specific recombination mediated by the yeast Flp recombinase. In addition, a plasmid with temperature-sensitive replication for temporal production of the Flp enzyme in E. coli has been constructed. After a gene disruption or deletion mutation is constructed in vitro by insertion of one of the cassettes into a given gene, the mutated gene is transferred to the E. coli chromosome by homologous recombination and selection for the antibiotic resistance provided by the cassette. If desired, the resistance determinant can subsequently be removed from the chromosome in vivo by Flp action, leaving behind a short nucleotide sequence with one FRT site and with no polar effect on downstream genes. This system was applied in the construction of an E. coli end A deletion mutation which can be transduced by P1 to the genetic background of interest using Tc-R as a marker. The transductant can then be freed of the Tc-R if required.

Cho, H. B. and T. G. Bernhardt (2013). "Identification of the SlmA active site responsible for blocking bacterial cytokinetic ring assembly over the chromosome." Plos Genetics **9**(2): e1003304.

Cho, H. B., et al. (2011). "Nucleoid occlusion factor SlmA is a DNA-activated FtsZ polymerization antagonist." Proceedings of the National Academy of Sciences of the United States of America **108**(9): 3773-3778.

Cook, W. R. and L. I. Rothfield (1999). "Nucleoid-independent identification of cell division sites in *Escherichia coli*." Journal of Bacteriology **181**(6): 1900-1905.

Cullum, J. and M. Vicente (1978). "CELL-GROWTH AND LENGTH DISTRIBUTION IN ESCHERICHIA-COLI." Journal of Bacteriology **134**(1): 330-337.

Cunha, S., et al. (2001). "Polymer-mediated compaction and internal dynamics of isolated Escherichia coli nucleoids." Journal of Structural Biology **136**(1): 53-66.

Curtis, T. P. and W. T. Sloan (2005). "Exploring microbial diversity - A vast below." Science **309**(5739): 1331-1333.

Datsenko, K. A. and B. L. Wanner (2000). "One-step inactivation of chromosomal genes in Escherichia coli K-12 using PCR products." Proceedings of the National Academy of Sciences of the United States of America **97**(12): 6640-6645.

de Boer, P. A. J. (2010). "Advances in understanding *E. coli* cell fission." Current Opinion in Microbiology **13**(6): 730-737.

de Vries, R. (2010). "DNA condensation in bacteria: Interplay between macromolecular crowding and nucleoid proteins." Biochimie **92**(12): 1715-1721.

Deghorain, M., et al. (2011) A defined terminal region of the *E. coli* chromosome shows late segregation and high FtsK activity. Plos One **6**, DOI: 10.1371/journal.pone.0022164

Den Blaauwen, T., et al. (1999). "Timing of FtsZ assembly in *Escherichia coli*." Journal of Bacteriology **181**(17): 5167-5175.

Di Ventura, B., et al. (2013) Chromosome segregation by the *Escherichia coli* Min system. Molecular Systems Biology **9**, DOI: 10.1038/msb.2013.44

Dorman, C. J. (2013). "Genome architecture and global gene regulation in bacteria: making progress towards a unified model?" Nature Reviews Microbiology **11**(5): 349-355.

Du, S. S. and J. Lutkenhaus (2014) SlmA antagonism of FtsZ assembly employs a two-pronged mechanism like MinCD. Plos Genetics **10**, DOI: 10.1371/journal.pgen.1004460

Dupaigne, P., et al. (2012). "Molecular basis for a protein-mediated DNA-bridging mechanism that functions in condensation of the *E. coil* chromosome." Molecular Cell **48**(4): 560-571.

Durand-Heredia, J. M., et al. (2011). "Identification and Characterization of ZapC, a Stabilizer of the FtsZ Ring in Escherichia coli." Journal of Bacteriology **193**(6): 1405-1413.

Ebersbach, G., et al. (2008). "Novel coiled-coil cell division factor ZapB stimulates Z ring assembly and cell division." Molecular Microbiology **68**(3): 720-735.

Erickson, H. P. (2009). "Size and Shape of Protein Molecules at the Nanometer Level Determined by Sedimentation, Gel Filtration, and Electron Microscopy." Biological Procedures Online **11**(1): 32-51.

Erickson, H. P., et al. (2010). "FtsZ in bacterial cytokinesis: cytoskeleton and force generator all in one." Microbiology and Molecular Biology Reviews **74**(4): 504-528.

Espeli, O., et al. (2012). "A MatP-divisome interaction coordinates chromosome segregation with cell division in *E. coli*." EMBO Journal **31**(14): 3198-3211.

Falkowski, P. G., et al. (2008). "The microbial engines that drive Earth's biogeochemical cycles." Science **320**(5879): 1034-1039.

Fange, D. and J. Elf (2006). "Noise-induced Min phenotypes in E-coli." Plos Computational Biology **2**(6): 637-648.

Fisher, J. K., et al. (2013). "Four-Dimensional Imaging of E. coli Nucleoid Organization and Dynamics in Living Cells." Cell **153**(4): 882-895.

Galli, E. and K. Gerdes (2010). "Spatial resolution of two bacterial cell division proteins: ZapA recruits ZapB to the inner face of the Z-ring." Molecular Microbiology **76**(6): 1514-1526.

Galli, E. and K. Gerdes (2012). "FtsZ-ZapA-ZapB Interactome of Escherichia coli." Journal of Bacteriology **194**(2): 292-302.

Guberman, J. M., et al. (2008). "PSICIC: Noise and asymmetry in bacterial division revealed by computational image analysis at sub-pixel resolution." Plos Computational Biology **4**(11): e1000233.

Halatek, J. and E. Frey (2012). "Highly canalized MinD transfer and MinE sequestration explain the origin of robust MinCDE-protein dynamics." Cell Reports **1**(6): 741-752.

Hanczyc, M. M. and J. W. Szostak (2004). "Replicating vesicles as models of primitive cell growth and division." Current Opinion in Chemical Biology **8**(6): 660-664.

Hedges, S. B. (2002). "The origin and evolution of model organisms." Nature Reviews Genetics **3**(11): 838-849.

Hendricks, E. C., et al. (2000). "Cell division, guillotining of dimer chromosomes and SOS induction in resolution mutants (dif, xerC and xerD) of *Escherichia coli*." Molecular Microbiology **36**(4): 973-981.

Huang, B., et al. (2009). Super-Resolution Fluorescence Microscopy. Annual Review of Biochemistry. **78:** 993-1016.

> Achieving a spatial resolution that is not limited by the diffraction of light, recent developments of super-resolution fluorescence microscopy techniques allow the observation of many biological structures not resolvable in conventional fluorescence microscopy. New advances in these techniques now give them the ability to image three-dimensional (3D) structures, measure interactions by multicolor colocalization, and record dynamic processes in living cells at the nanometer scale. It is anticipated that super-resolution fluorescence microscopy will become a widely used tool for cell and tissue imaging to provide previously unobserved details of biological structures and processes.

Huang, K. C., et al. (2003). "Dynamic structures in *Escherichia coli*: Spontaneous formation of MinE rings and MinD polar zones." Proceedings of the National Academy of Sciences of the United States of America **100**(22): 12724-12728.

Hussain, K., et al. (1987). "ParD - a new gene coding for a protein required for chromosome partitioning and septum localization in *Escherichia coli*." Molecular Microbiology **1**(1): 73-81.

Ivanov, V. and K. Mizuuchi (2010). "Multiple modes of interconverting dynamic pattern formation by bacterial cell division proteins." Proceedings of the National Academy of Sciences of the United States of America **107**(18): 8071-8078.

Jia, S., et al. (2014) Effect of the Min system on timing of cell division in *Escherichia coli*. Plos One **9**, DOI: 10.1371/journal.pone.0103863

Joshi, M. C., et al. (2011). "Escherichia coli sister chromosome separation includes an abrupt global transition with concomitant release of late-splitting intersister snaps." Proceedings of the National Academy of Sciences of the United States of America **108**(7): 2765-2770.

Kempen, G. M. P. v., et al. (2014). DIP*lib* function reference. Netherlands, Delft University of Technology.

Kennedy, S. P., et al. (2008). "Delayed activation of Xer recombination at dif by FtsK during septum assembly in Escherichia coli." Molecular Microbiology **68**(4): 1018-1028.

Kenneth R, C., et al. (2008). Microscope Image Processing. Burlington, Academic Press.

Kerr, R. A., et al. (2006). "Division accuracy in a stochastic model of Min oscillations in Escherichia coli." Proceedings of the National Academy of Sciences of the United States of America **103**(2): 347-352.

Kruse, K. (2002). "A dynamic model for determining the middle of *Escherichia coli*." Biophysical Journal **82**(2): 618-627.

Kubitschek, H. E. (1990). "CELL-VOLUME INCREASE IN ESCHERICHIA-COLI AFTER SHIFTS TO RICHER MEDIA." Journal of Bacteriology **172**(1): 94-101.

Lee, P. S. and K. H. Lee (2003). "Escherichia coli - A model system that benefits from and contributes to the evolution of proteomics." Biotechnology and Bioengineering **84**(7): 801-814.

Liu, B., et al. (2015) Roles for both FtsA and the FtsBLQ subcomplex in FtsN-stimulated cell constriction in *Escherichia coli*. Molecular Microbiology DOI: doi:10.1111/mmi.12906

Loose, M., et al. (2008). "Spatial regulators for bacterial cell division self-organize into surface waves *in vitro*." Science **320**(5877): 789-792.

Loose, M. and T. J. Mitchison (2014). "The bacterial cell division proteins FtsA and FtsZ self-organize into dynamic cytoskeletal patterns." Nature Cell Biology **16**(1): 38-+.

Bacterial cytokinesis is commonly initiated by the Z-ring, a cytoskeletal structure that assembles at the site of division. Its primary component is FtsZ, a tubulin superfamily GTPase, which is recruited to the membrane by the actin-related protein FtsA. Both

proteins are required for the formation of the Z-ring, but if and how they influence each other's assembly dynamics is not known. Here, we reconstituted FtsA-dependent recruitment of FtsZ polymers to supported membranes, where both proteins self-organize into complex patterns, such as fast-moving filament bundles and chirally rotating rings. Using fluorescence microscopy and biochemical perturbations, we found that these large-scale rearrangements of FtsZ emerge from its polymerization dynamics and a dual, antagonistic role of FtsA: recruitment of FtsZ filaments to the membrane and negative regulation of FtsZ organization. Our findings provide a model for the initial steps of bacterial cell division and illustrate how dynamic polymers can self-organize into large-scale structures.

Low, H. H., et al. (2004). "The crystal structure of ZapA and its modulation of FtsZ polymerisation." Journal of Molecular Biology **341**(3): 839-852.

FtsZ is part of a mid-cell cytokinetic structure termed the Z-ring that recruits a hierarchy of fission related proteins early in the bacterial cell cycle. The widely conserved ZapA has been shown to interact with FtsZ, to drive its polymerisation and to promote FtsZ filament bundling thereby contributing to the spatio-temporal tuning of the Z-ring. Here, we show. the crystal structure of ZapA (11.6 kDa) from Pseudomonas aeruginosa at 2.8 Angstrom resolution. The electron density reveals two dimers associating via an extensive C-terminal coiled-coil protrusion to form an elongated antiparallel tetramer. In solution, ZapA exists in a dimer-tetramer equilibrium that is strongly correlated with concentration. An increase in concentration promotes formation of the higher oligomeric state. The dimer is postulated to be the predominant physiological species although the tetramer could become significant if, as FtsZ is integrated into the Z-ring and is cross-linked, the local concentration of the dimer becomes sufficiently high. We also show that ZapA binds FtsZ with an approximate 1 : 1 molar stoichiometry and that this interaction provokes dramatic FtsZ polymerisation and inter-filament association as well as yielding filaments, single or bundled, more stable and resistant to collapse. Whilst in vitro dynamics of FtsZ are well characterised, its in vivo arrangement within the ultra-structural architecture of the Z-ring is yet to be determined despite being fundamental to cell division. The ZapA dimer has single 2-fold symmetry whilst the bipolar tetramer displays triple 2-fold symmetry. Given the symmetry of these ZapA oligomers and the polar nature of FtsZ filaments, the structure of ZapA carries novel implications for the inherent architecture of the Z-ring in vivo. (C) 2004 Elsevier Ltd. All rights reserved.

Lutkenhaus, J. (2007). "Assembly dynamics of the bacterial MinCDE system and spatial regulation of the Z ring." Annual Review of Biochemistry **76**: 539-562.

Lutkenhaus, J. (2012). "The ParA/MinD family puts things in their place." Trends in Microbiology **20**(9): 411-418.

Lutkenhaus, J., et al. (2012). "Bacterial cytokinesis: From Z ring to divisome." Cytoskeleton **69**(10): 778-790.

Männik, J. and M. W. Bailey (2015). "Spatial coordination between chromosomes and cell division proteins in *Escherichia coli*." Frontiers in Microbiology **6**: 306.

Mannik, J., et al. (2016). "The role of MatP, ZapA and ZapB in chromosomal organization and dynamics in Escherichia coli." Nucleic Acids Research **44**(2).

Männik, J., et al. (2012). "Robustness and accuracy of cell division in *Escherichia coli* in diverse cell shapes." Proceedings of the National Academy of Sciences of the United States of America **109**: 6957-6962.

Margolin, W. (2005). "FtsZ and the division of prokaryotic cells and organelles." Nature Reviews Molecular Cell Biology **6**(11): 862-871.

Meinhardt, H. and P. A. J. de Boer (2001). "Pattern formation in *Escherichia coli*: A model for the pole-to-pole oscillations of Min proteins and the localization of the division site." Proceedings of the National Academy of Sciences of the United States of America **98**(25): 14202-14207.

Mercier, R., et al. (2008). "The MatP/matS site-specific system organizes the terminus region of the *E. coli* chromosome into a macrodomain." Cell **135**(3): 475-485.

Mojzsis, S. J., et al. (1997). "Evidence for life on Earth before 3,800 million years ago (vol 384, pg 55, 1996)." Nature **386**(6626): 738-738.

Monahan, L. G., et al. (2014). "Division site positioning in bacteria: one size does not fit all." Frontiers in Microbiology **5**.

Moriya, S., et al. (2010). "Influence of the nucleoid and the early stages of DNA replication on positioning the division site in *Bacillus subtilis*." Molecular Microbiology **76**(3): 634-647.

Moseley, J. B. and P. Nurse (2010). "Cell division intersects with cell geometry." Cell **142**(2): 189-193.

Mulder, E., et al. (1990). "The *Escherichia coli* MinB mutation resembles GyrB in defective nucleoid segregation and decreased negative supercoiling of plasmids." Molecular & General Genetics **221**(1): 87-93.

Mulder, E. and C. L. Woldringh (1989). "Actively replicating mucleoids influence positioning of division sites in *Escherichia coli* filaments forming cells lacking DNA." Journal of Bacteriology **171**(8): 4303-4314.

Niki, H., et al. (1991). "The new gene MukB codes for a 177 kD protein with coiled-coil domains involved in chromosome partitioning of *Escherchia coli*." EMBO Journal **10**(1): 183-193.

Niki, H., et al. (2000). "Dynamic organization of chromosomal DNA in Escherichia coli." Genes & Development **14**(2): 212-223.

Norris, V. (1995). "Hypothesis - chromosome separation in *Escherichia coli* involves autocatalytic gene expression, transertion and membrane-domain formation." Molecular Microbiology **16**(6): 1051-1057.

O'Malley, M. (2014). Philosophy of Microbiology, Cambridge University Press.

Odijk, T. (1998). "Osmotic compaction of supercoiled DNA into a bacterial nucleoid." Biophysical Chemistry **73**(1-2): 23-29.

Pazos, M., et al. (2014) FtsZ placement in nucleoid-free bacteria. Plos One **9**, DOI: 10.1371/journal.pone.0091984

Phillips, R., et al. (2012). Physical Biology of the Cell. New York, Garland Science, Taylor & Francis Group, LLC.

Pinho, M. G., et al. (2013). "How to get (a)round: mechanisms controlling growth and division of coccoid bacteria." Nature Reviews Microbiology **11**(9): 601-614.

Pogliano, J., et al. (1997). "Inactivation of FtsI inhibits constriction of the FtsZ cytokinetic ring and delays the assembly of FtsZ rings at potential division sites." Proceedings of the National Academy of Sciences of the United States of America **94**(2): 559-564.

Rabinovitch, A., et al. (2003). "DNA-membrane interactions can localize bacterial cell center." Journal of Theoretical Biology **225**(4): 493-496.

Raskin, D. M. and P. A. J. de Boer (1999). "Rapid pole-to-pole oscillation of a protein required for directing division to the middle of *Escherichia coli*." Proceedings of the National Academy of Sciences of the United States of America **96**(9): 4971-4976.

Reshes, G., et al. (2008). "Cell shape dynamics in Escherichia coli." Biophysical Journal **94**(1): 251-264.

> Bacteria are the simplest living organisms. In particular, Escherichia coli has been extensively studied and it has become one of the standard model systems in microbiology. However, optical microscopy studies of single E. coli have been limited by its small size, similar to 1 x 3 mu m, not much larger than the optical resolution, similar to 0.25 mu m. As a result, not enough quantitative dynamical information on the life cycle of single E. coli is presently available. We suggest that, by careful analysis of images from phase contrast and fluorescence time-lapse microscopy, this limitation can be bypassed. For example, we show that applying this approach to monitoring morphogenesis in individual E. coli leads to a simple, quantitative description of this process. First, we find the time when the formation of the septum starts, tau(c). It occurs much earlier than the time when the constriction can be directly observed by phase contrast. Second, we find that the growth law of single cells is more likely bilinear/trilinear than exponential. This is further supported

by the relations that hold between the corresponding growth rates. These methods could be further extended to study the dynamics of cell components, e.g., the nucleoid and the Z-ring.

Rodrigues, C. D. A. and E. J. Harry (2012). "The Min system and nucleoid occlusion are not required for identifying the division site in *Bacillus subtilis* but ensure its efficient utilization." Plos Genetics **8**(3): e1002561.

Schrum, J. P., et al. (2010). "The Origins of Cellular Life." Cold Spring Harbor Perspectives in Biology **2**(9).

Schweizer, J. C., et al. (2011). "Min-waves on confined artificial membranes." European Biophysics Journal with Biophysics Letters **40**: 85-85.

Shapiro, L., et al. (2009). "Why and how bacteria localize proteins." Science **326**(5957): 1225-1228.

Sherratt, D. J., et al. (2010). "The *Escherichia coli* DNA translocase FtsK." Biochemical Society Transactions **38**: 395-398.

Shlomovitz, R. and N. S. Gov (2009) Membrane-mediated interactions drive the condensation and coalescence of FtsZ rings. Physical Biology **6**, DOI: 10.1088/1478-3975/6/4/046017

The role of the coupling between the shape of membrane-bound filaments and the membrane is demonstrated for the dynamics of FtsZ rings on cylindrical membranes. Filaments with an arc-like spontaneous curvature, and a possible added active contractile force, are shown to spontaneously condense into tight rings, associated with a local inward deformation of the membrane. The long-range membrane-mediated interactions are attractive at short ring-ring separations, inducing further coarsening dynamics, whereby smaller rings merge to form larger and fewer rings that deform the membrane more strongly. At the same time, these interactions induce a potential barrier that can suppress further ring coalescence at a separation of about seven times the cylinder radius. These results of the model are in very good agreement with recent in-vitro experiments on the dynamics of FtsZ filaments in cylindrical liposomes. These results emphasize the important role of long-range membrane-mediated interactions in the organization of cytoskeletal elements at the membrane.

Singleton, P. (2004). Bacteria in biology, biotechnology and medicine.

Stouf, M., et al. (2013). "FtsK actively segregates sister chromosomes in *Escherichia coli*." Proceedings of the National Academy of Sciences of the United States of America **110**(27): 11157-11162.

Sun, Q. and W. Margolin (1998). "FtsZ dynamics during the division cycle of live *Escherichia coli* cells." Journal of Bacteriology **180**(8): 2050-2056.

Sun, Q., et al. (1998). "Assembly of the FtsZ ring at the central division site in the absence of the chromosome." Molecular Microbiology **29**(2): 491-503.

Thomason, L. C., et al. (2001). E. coli Genome Manipulation by P1 Transduction. Current Protocols in Molecular Biology, John Wiley & Sons, Inc.

Tonthat, N. K., et al. (2011). "Molecular mechanism by which the nucleoid occlusion factor, SlmA, keeps cytokinesis in check." EMBO Journal **30**(1): 154-164.

Tonthat, N. K., et al. (2013). "SlmA forms a higher-order structure on DNA that inhibits cytokinetic Z-ring formation over the nucleoid." Proceedings of the National Academy of Sciences of the United States of America **110**(26): 10586-10591.

Treuner-Lange, A., et al. (2013). "PomZ, a ParA-like protein, regulates Z-ring formation and cell division in *Myxococcus xanthus*." Molecular Microbiology **87**(2): 235-253.

Trueba, F. J. (1982). "On the precision and accuracy achieved by *Escherichia coli* cells at fission about their middle." Archives of Microbiology **131**(1): 55-59.

Turing, A. M. (1952). "The Chemical Basis of Morphogenesis." Phil. Transact. Royal Soc. B **237**(641): 37-72.

Valens, M., et al. (2004). "Macrodomain organization of the Escherichia coli chromosome." EMBO Journal **23**(21): 4330-4341.

Wang, P., et al. (2010). "Robust Growth of Escherichia coli." Current Biology **20**(12): 1099-1103.

Wang, W. Q., et al. (2011). "Chromosome Organization by a Nucleoid-Associated Protein in Live Bacteria." Science **333**(6048): 1445-1449.

Wang, X. D., et al. (2005). "Dancing around the divisome: asymmetric chromosome segregation in Escherichia coli." Genes & Development **19**(19): 2367-2377.

Whitman, W. B., et al. (1998). "Prokaryotes: The unseen majority." Proceedings of the National Academy of Sciences of the United States of America **95**(12): 6578-6583.

Willemse, J., et al. (2011). "Positive control of cell division: FtsZ is recruited by SsgB during sporulation of *Streptomyces*." Genes & Development **25**(1): 89-99.

Woldringh, C. L. (2002). "The role of co-transcriptional translation and protein translocation (transertion) in bacterial chromosome segregation." Molecular Microbiology **45**(1): 17-29.

Many recent reviews in the field of bacterial chromosome segregation propose that newly replicated DNA is actively separated by the functioning of specific proteins. This view is primarily based on an interpretation of the position of fluorescently labelled DNA regions and proteins in analogy to the active segregation mechanism in eukaryotic cells, i.e. to mitosis. So far, physical aspects of DNA organization such as the diffusional movement of DNA supercoil segments and their interaction with soluble proteins, leading to a phase separation between cytoplasm and nucleoid, have received relatively little attention. Here, a quite different view is described taking into account DNA-protein interactions, the large variation in the cellular position of fluorescent foci and the compaction and fusion of segregated nucleoids upon inhibition of RNA or protein synthesis. It is proposed that the random diffusion of DNA supercoil segments is transiently constrained by the process of co- transcriptional translation and translocation (transertion) of membrane proteins. After initiation of DNA replication, a bias in the positioning of transertion areas creates a bidirectionality in chromosome segre-gation that becomes self-enhanced when neigh-bouring genes on the same daughter chromosome are expressed. This transertion-mediated segregation model is applicable to multifork replication during rapid growth and to multiple chromosomes and plasmids that occur in many bacteria.

Woldringh, C. L., et al. (1990). "Role of the nucleoid in the toporegulation of division." Research in Microbiology **141**(1): 39-49.

Wu, L. J. and J. Errington (1994). "*Bacillus subtilis* SpoIIIE protein required for DNA segregation during asymmetric cell division." Science **264**(5158): 572-575.

Wu, L. J. and J. Errington (2004). "Coordination of cell division and chromosome segregation by a nucleoid occlusion protein in *Bacillus subtillis*." Cell **117**(7): 915-925.

Wu, L. J. and J. Errington (2011). "Nucleoid occlusion and bacterial cell division." Nature Reviews Microbiology **10**(1): 8-12.

Young, I. T., et al. (1998). Fundamentals of Image Processing. Netherlands, Delft PH Publications.

Yu, X. C. and W. Margolin (1999). "FtsZ ring clusters in min and partition mutants: role of both the Min system and the nucleoid in regulating FtsZ ring localization." Molecular Microbiology **32**(2): 315-326.

Zaritsky, A. and C. L. Woldringh (2003). "Localizing cell division in spherical *Escherichia coli* by nucleoid occlusion." Fems Microbiology Letters **226**(2): 209-214.

Appendix

Analytical evaluation of VENO as an FtsZ-filament positioning system in *E. coli*.

To properly treat each of the B_{i-j} terms, we would need to accurately assess the electrostatic repulsion between species i and j when immersed in an environment with uniform permittivity ϵ and concentration of salts n_s. Moreover, cytosolic proteins come in a variety of sizes, shapes, and net electric charge. In this approximation, we neglect the effects of electrostatic screening and consider all cytosolic proteins as if they were spherical in shape, and have radii of approximately 1-2nm. This radius applies only for relatively small proteins (10-30 kDa) (Erickson 2009). We treat FtsZ filaments, and DNA supercoils as cylinders, with physical dimensions taken from existing literature (Table 4, below). Consequently, these results provide only an order of magnitude approximation, and the results should be interpreted within this context.

Generally, the excluded volume between two cylinders of diameter D with length L oriented at an angle θ with respect to their long axes can be approximated as $B = 2 \cdot D \cdot L^2 \cdot \sin(\theta)$ which is the volume of a parallelopiped composed of the two cylinders (Phillips, Kondev et al. 2012). Taking the average of $\sin(\theta)$ over all available angles adds a factor of $\pi/4$ to the excluded volume leaving, $B = \frac{1}{2}\pi \cdot D \cdot L^2$. In the case $L \gg D$, this approximation is exact (Phillips, Kondev et al. 2012). When the two cylinders have differing dimensions, the excluded volume becomes $B_{i-j} = \frac{\pi}{4} \cdot (D_i + D_j) \cdot L_i \cdot L_j$. With reasonable estimations for the excluded volumes, we express the contribution to chemical potential from excluded volume interactions (Figure 46):

$$\mu_{FtsZ-DNA} = k_B T \cdot \frac{N_{Branch}}{V} \cdot B_{FtsZ-Branch} = k_B T \cdot \frac{N_{Branch}}{V} \cdot \frac{\pi \cdot (D_{FtsZ} + D_{Branch}) \cdot L_{FtsZ} \cdot L_{Branch}}{4}$$

$$\mu_{FtsZ-FtsZ} = k_B T \cdot \frac{B_{FtsZ-FtsZ}}{V} = k_B T \cdot \frac{\pi \cdot L_{FtsZ}^2 \cdot D_{FtsZ}}{2 \cdot V}$$

To treat the interaction between a cylindrical FtsZ filaments and globular (spherical) cytosolic proteins, we use the approximation from Odijk, which assumes a cylindrical excluded volume of

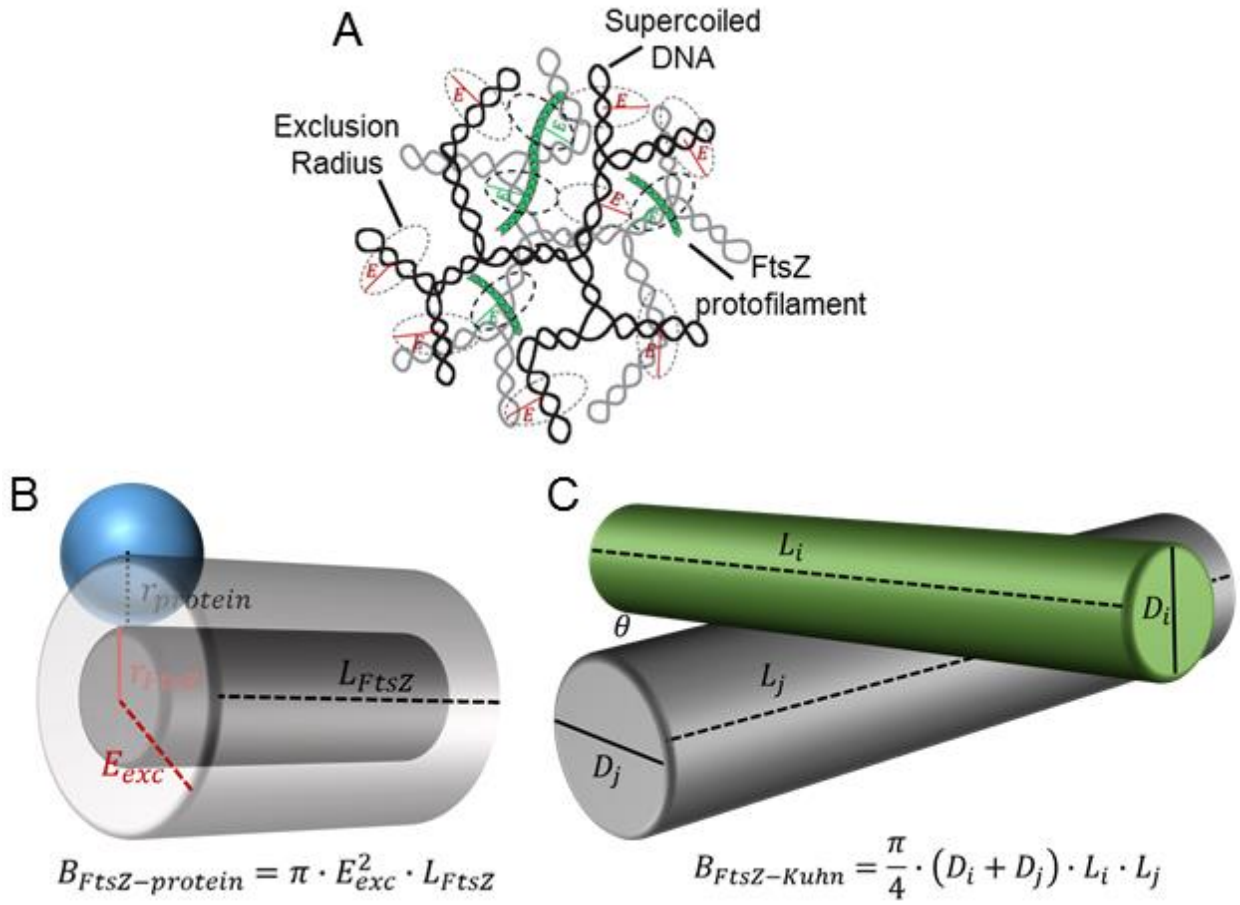

Figure 46. Estimating excluded volumes. (A) The bacterial chromosome is organized as a network of supercoiled branches, each of which is approximately 160nm long. The diameter of the supercoiled branches is approximately 10nm. Also shown are hypothetical FtsZ filaments, interacting with the supercoiled DNA branches. E represents the exclusion radius (not drawn to scale). Image adapted from (Woldringh 2002). (B) We approximate the excluded volume for the interaction between a spherical cytosolic protein and an FtsZ filament as the volume of a cylinder with exclusion radius equal to the sum of the protein radius and the FtsZ cylinder's radius. (C) The excluded volume for the interaction of FtsZ filaments and the supercoiled DNA branches is estimated as the area of a parallelepiped with dimensions $D_i + D_j$, L_i, and L_j.

the form $B_{FtsZ-protein} = \pi \cdot L_{FtsZ} \cdot E_{exc}^2$ (Figure 46). E_{exc} represents the exclusion radius of a cytosolic protein due to the FtsZ filament. We take E_{exc} to be 2.5 nm, which is slightly larger than the size of small, spherical proteins (Erickson 2009).

$$\mu_{FtsZ-protein} = k_B T \cdot \frac{N_p}{V} \cdot B_{FtsZ-protein} = k_B T \cdot \frac{N_p}{V} \cdot \pi \cdot L_{FtsZ} \cdot E_{exc}^2$$

Treating FtsZ filaments as a dilute solute immersed in a concentration of solvent molecules (water):

$$\mu_{FtsZ\ solute} = \mu_{\mathrm{ref}} + k_B T \cdot \ln(c_{FtsZ})$$

Where μ_{ref} represents the chemical potential at a convenient reference state, which is often taken when all molecular components are at a 1M concentration (Phillips, Kondev et al. 2012). This term also takes into consideration the solvation energy of the solvent molecules. Equating chemical potentials for FtsZ filaments within each part of the intercellular volume ($\mu_{FtsZ_{nucleoid}} = \mu_{FtsZ_{cytosol}}$) gives:

$$\mu_{\mathrm{ref}} + k_B T \cdot \ln\left(c_{FtsZ_n}\right) + \frac{N_p \cdot \pi \cdot L_{FtsZ} \cdot E_{exc}^2}{V_n} + \frac{\pi \cdot L_{FtsZ}^2 \cdot D_{FtsZ}}{2 \cdot V_n}$$

$$+ \frac{\pi \cdot L_{FtsZ} \cdot (D_{FtsZ} + D_{Branch}) \cdot L_{Branch} \cdot N_{Branch}}{4 \cdot V_n}$$

$$= \mu_{\mathrm{ref}} + k_B T \cdot \ln\left(c_{FtsZ_c}\right) + \frac{N_p \cdot \pi \cdot L_{FtsZ} \cdot E_{exc}^2}{V_c} + \frac{\pi \cdot L_{FtsZ}^2 \cdot D_{FtsZ}}{2 \cdot V_c}$$

The FtsZ filament-filament interactions contribute little to the total chemical potential, therefore we keep only leading order terms in L_{FtsZ}. After introducing the following short hand notations,

$$\epsilon_{exc}^2 \equiv \pi \cdot E_{exc}^2, \ \ \ell_{DNA}^2 \equiv \frac{\pi \cdot (D_{FtsZ} + D_{Branch}) \cdot L_{Branch} \cdot N_{Branch}}{4}$$

We can rewrite the equality in leading order of L_{FtsZ}:

$$\ln\left(c_{FtsZ_n}\right) + c_{p_n} \cdot L_{FtsZ} \cdot \epsilon_{exc}^2 + \frac{\ell_{DNA}^2 \cdot L_{FtsZ}}{V_n} = \ln\left(c_{FtsZ_c}\right) + c_{p_c} \cdot L_{FtsZ} \cdot \epsilon_{exc}^2$$

$$\ln\left(\frac{c_{FtsZ_n}}{c_{FtsZ_c}}\right) + L_{FtsZ} \cdot \left(c_{p_n} - c_{p_c}\right) \cdot \epsilon_{exc}^2 + L_{FtsZ} \cdot \left(\frac{\ell_{DNA}^2}{V_n}\right) = 0$$

$$\ln\left(\frac{c_{FtsZ_n}}{c_{FtsZ_c}}\right) = -L_{FtsZ} \cdot \left(\left(\frac{\ell_{DNA}^2}{V_n}\right) - \left(c_{p_c} - c_{p_n}\right) \cdot \epsilon_{exc}^2\right)$$

$$\frac{c_{FtsZ_n}}{c_{FtsZ_c}} = e^{-L_{FtsZ} \cdot \left(\left(\frac{\ell_{DNA}^2}{V_n}\right) - \left(c_{p_c} - c_{p_n}\right) \cdot \epsilon_{exc}^2\right)}$$

Defining $\frac{1}{\mathcal{L}_{FtsZ}} \equiv \left(\frac{\ell_{DNA}^2}{V_n}\right) - \left(c_{p_c} - c_{p_n}\right) \cdot \epsilon_{exc}^2$:

$$\frac{c_{FtsZ_n}}{c_{FtsZ_c}} = e^{-\frac{L_{FtsZ}}{\mathcal{L}_{FtsZ}}}$$

Table 4: Evaluation of decay constant for FtsZ filaments excluded from supercoiled DNA

Constant	Value	Source
E_{exc}	2.5 [nm]	(Erickson 2009)
V_n	0.1 [μm^3]	(Odijk 1998, Wang, Li et al. 2011)
N_{Branch}	4,000	(Woldringh 2002)
L_{Branch}	158 [nm]	(Cunha, Woldringh et al. 2001)
D_{Branch}	10 [nm]	(Cunha, Woldringh et al. 2001)
D_{FtsZ}	2.5 [nm]	(Erickson 2009)
ϕ_{p_c}	0.166	(Odijk 1998)
ϕ_{p_n}	0.06	(Odijk 1998)

Evaluation of derived terms:

$$\epsilon_{exc}^2 \equiv \pi \cdot E_{exc}^2 = 1.96 \cdot 10^{-5}\ [\mu m^2]$$

$$\ell_{DNA} \equiv \frac{\pi \cdot (0.0025\mu m + 0.01\mu m) \cdot 0.158[\mu m] \cdot 4 \cdot 10^3}{4} = 6.20[\mu m^2]$$

$$\phi \equiv \text{Volume Fraction} = c \cdot v_{exc}$$

$$c_{p_c} = \frac{\phi_{p_c}}{\frac{4}{3}\pi R_{exc}^3} = \frac{0.166}{\frac{4}{3}\pi(0.0025\mu m)^3} = \frac{0.166}{6.54 \cdot 10^{-8}}[\mu m]^{-3} = 2{,}538{,}226[\mu m]^{-3}$$

$$c_{p_n} = \frac{\phi_{p_c}}{\frac{4}{3}\pi R_{exc}^3} = \frac{0.06}{\frac{4}{3}\pi(0.0025\mu m)^3} = \frac{0.06}{6.54 \cdot 10^{-8}}[\mu m]^{-3} = 917{,}431[\mu m]^{-3}$$

$$\frac{1}{\mathcal{L}_{FtsZ}} \equiv \left(\frac{\ell_{DNA}}{V_n}\right) - \left(c_{p_c} - c_{p_n}\right) \cdot \epsilon_{exc}^2$$

$$= \frac{6.20[\mu m^2]}{0.1[\mu m^3]} - (2{,}538{,}226\ [\mu m]^{-3} - 917{,}431\ [\mu m]^{-3}) \cdot\ 1.96 \cdot 10^{-5}\ [\mu m^2]$$

$$\therefore \mathcal{L}_{FtsZ} = 0.0331\ [\mu m] \sim 33\ [nm]$$

Table 5. List of the strains and plasmids used in experiments.

Strain	Plasmid	Genotype	Source
BW25113	pKen1-GFPμ2 (2)	wild type	Keio collection parental strain (Baba, Ara et al. 2006)
JW5641-1	-	Δ*slmA*::*frt-kan-frt*	Keio collection knockout (Baba, Ara et al. 2006)
JW1165	-	Δ*minC*::*frt-kan-frt*	Keio collection knockout (Baba, Ara et al. 2006)
JW1165	pKen1-GFPμ2 (2)	Δ*minC*::*frt-kan-frt*	Keio collection knockout (Baba, Ara et al. 2006)
PB194	pKen1-GFPμ2 (2)	Δ*slmA*::*frt-kan-frt* Δ*minC*::*frt*	This work: kanamycin resistance cassette is evicted from Keio collection knockout JW1165 and resulting strain is P1 transduced with lysate from JW5641-1.
TB86(λCH151)	-	Δ*slmA*::*frt-kan-frt* Δ*minCDE*::*frt* P_{lac}-*zipA-gfp-amp*	Gift from P. A. J. de Boer (Case Western Reserve University) (Bernhardt and de Boer 2005)
TB86(λDR120)	-	Δ*slmA*::*frt-kan-frt* Δ*minCDE*::*frt* P_{lac}-*gfp-T7tag-ftsZ*	Gift from P. A. J. de Boer (Case Western Reserve University) (Bernhardt and de Boer 2005)
JMBW5	-	P_{lac}-*zipA-gfp-amp*	This work: Inducible ZipA-GFP was P1 transduced from TB86(λCH151) lysate to MG1655 strain.
WD1	-	Δ*slmA*::*frt* Δ*minCDE*::*frt* P_{lac}-*zipA-gfp-amp* *matP-mCherry-frt-kan-frt*	This work: kanamycin resistance cassette is evicted from TB86(λCH151). Resulting strain was P1 transduced with *matP-mCherry-frt-kan-frt* from PB232 (1).
WD2	-	P_{lac}-*zipA-gfp-amp* *matP-mCherry-frt-kan-frt*	This work: JMBW5 was P1 transduced with *matP-mCherry*
MB1	-	Δ*minCDE*::*frt* Δ*slmA*::*frt* P_{lac}-*zipA-gfp-amp* *hupA-mCherry-frt-kan-frt*	This work: *E. coli* TB86 was P1 transduced with lysate from strain PB384 (1) carrying *hupA-mCherry-frt-kan-frt*.
MB2	-	P_{lac}-*zipA-gfp-amp* *hupA-mCherry-frt-kan-frt*	This work: *E. coli* MG1655 was P1 transduced with lysate from TB86 to transfer inducible ZipA-GFP. The resulting strain was P1 transduced with lysate from strain PB384 (1) carrying *hupA-mCherry-frt-kan-frt.*

Table 5 continued.

MB4	-	Δ*slmA*::*frt* Δ*minC*::*frt* Δ*zapB*:: *frt-kan-frt* P_{lac}-*zipA-gfp-amp*	This work: kanamycin resistance cassette is evicted from PB194. The resulting strain is P1 transduced with *frt-kan-frt* lysate from Keio collection knockout JW3899-1
MB10	-	Δ*slmA*::*frt* Δ*minC*::*frt* Δ*matP*::*frt-kan-frt* P_{lac}-*zipA-gfp-amp*	This work: kanamycin resistance cassette is evicted from PB194. The resulting strain is P1 transduced with *frt-kan-frt* lysate from Keio collection knockout JW0939-1
MB11	-	Δ*slmA*::*frt* Δ*minC*::*frt* Δ*zapA*::*frt-kan-frt* P_{lac}-*zipA-gfp-amp*	This work: kanamycin resistance cassette is evicted from PB194. The resulting strain is P1 transduced with *frt-kan-frt* lysate from Keio collection knockout JW2878-1 to replace *zapA*.
MB14	-	Δ*minC*::*frt* Δ*slmA*::*frt* Δ*matP*::*frt* P_{lac}-*zipA-gfp-amp* *hupA-mCherry-frt-kan-frt*	This work: The kan cassette was evicted from MB10. The resulting strain was P1 transduced with lysate from strain PB384 (1) carrying *hupA-mCherry-frt-kan-frt.*
MB15	-	Δ*minC*::*frt* Δ*slmA*::*frt* Δ*zapA*::*frt* P_{lac}-*zipA-gfp-amp* *hupA-mCherry-frt-kan-frt*	This work: The kan cassette was evicted from MB11. The resulting strain was P1 transduced with lysate from strain PB384 (1) carrying *hupA-mCherry-frt-kan-frt.*
MB16	-	Δ*minC*::*frt* Δ*slmA*::*frt* Δ*zapB*::*frt* P_{lac}-*zipA-gfp-amp* *hupA-mCherry-frt-kan-frt*	This work: Keio collection BW25113 was sequentially P1 transduced with lysates from JW1165, JW5641-1, and JW3899-1 to delete *minC*, *slmA*, and *zapB*, respectively. The kanamycin cassette was evicted following each P1 transduction. The resulting strain was P1 transduced with a lysate from TB86 to transfer the inducible ZipA-GFP and the kan cassette evicted. The resulting strain was P1 transduced with lysate from strain PB384 (1) carrying *hupA-mCherry-frt-kan-frt.*
MB21	-	Δ*slmA*::*frt* P_{lac}-*zipA-gfp-amp*	This work: kanamycin resistance cassette is evicted from JW5641-1. The resulting strain is P1 transduced from TB86(λCH151) lysate to transfer inducible ZipA-GFP.

Table 5 continued.

MB22	-	Δ*minC*::*frt* P_{lac}-*zipA-gfp-amp*	This work: kanamycin resistance cassette is evicted from JW1165. The resulting strain is P1 transduced from TB86(λCH151) lysate to transfer inducible ZipA-GFP.
MB25	-	Δ*slmA*::*frt* P_{lac}-*zipA-gfp-amp* Δ*matP-mCherry-frt-kan-frt*	This work: MB21 was P1 transduced with *matP-mCherry-frt-kan-frt* from PB232 (1).
MB26	-	Δ*minC*::*frt* P_{lac}-*zipA-gfp-amp* Δ*matP-mCherry-frt-kan-frt*	This work: MB22 was P1 transduced with *matP-mCherry-frt-kan-frt* from PB232 (1).
MB27	-	Δ*minC*::*frt* Δ*slmA*::*frt* Δ*zapA*::*frt* P_{lac}-*zipA-gfp-amp* *matP-mCherry-frt-kan-frt*	This work: The kan cassette was evicted from MB11. The resulting strain was P1 transduced with *matP-mCherry-frt-kan-frt* PB232 (1).
MB38	-	Δ*minC*::*frt* Δ*slmA*::*frt* Δ*zapB*::*frt* Δ*ftsK::ftsK*$^{ATP-}$*cm* P_{lac}-*zipA-gfp-amp* *hupA-mCherry-frt-kan-frt*	This work: MB16 was P1 transduced with a lysate from FC1 (Kennedy, Chevalier et al. 2008) to transfer the K997A point mutation in FtsK.
MB39	-	Δ*ftsK::ftsK*$^{ATP-}$*cm* P_{lac}-*zipA-gfp-amp* *hupA-mCherry-frt-kan-frt*	This work: MB2 was P1 transduced with a lysate from FC1 to transfer the K997A point mutation in FtsK.
MB40	-	Δ*minC*::*frt* Δ*slmA*::*frt* Δ*zapA*::*frt* Δ*ftsK::ftsK*$^{ATP-}$*cm* P_{lac}-*zipA-gfp-amp* *hupA-mCherry-frt-kan-frt*	This work: MB15 was P1 transduced with a lysate from FC1 to transfer the K997A point mutation in FtsK.
PB299	-	Δ*slmA*::*frt-kan-frt* Δ*minC*::*frt* Δ*zapB*:: *frt-cm-frt*	This work: PB194 is P1 transduced with *frt-cm-frt* lysate from HY1-32 (Durand-Heredia, Yu et al. 2011).
PB300	-	Δ*slmA*::*frt-kan-frt* Δ*minC*::*frt* Δ*zapA*:: *frt-cm-frt*	This work: PB194 is P1 transduced with *frt-cm-frt* lysate from HY1-31.
PB301	-	Δ*slmA*::*frt-kan-frt* Δ*minC*::*frt* Δ*matP*:: *frt-cm-frt*	This work: PB194 is P1 transduced with *frt-cm-frt* lysate from (Mercier, Petit et al. 2008).

Table 5 continued.

RH14	pEG3a P_{BAD}::*zapB::gfp-Cm*^{R}	*matP-mCherry-frt-kan-frt*	MG1655 transduced with lysate from PB232 (1), to transfer *matP-mCherry*. Strain contains plasmid pEG3a carrying the ZapB-GFP (inducible with 0.2% arabinose (Ebersbach, Galli et al. 2008).

1. Strain is a generous gift from P. Bissichia and D. Sherratt from Oxford University.

Quantifying DNA translocation rate

To quantify the fraction of the nucleoid translocated across the septum in asymmetrically dividing daughter cells, we measure the total fluorescence intensity of the HupA-mCherry labeled-DNA on both sides of the Z-ring/division plane as function of time. In the main text Figures, we refer to the total intensity of the fluorescent signal from smaller daughter as I_1 and from the larger daughter as I_2. To measure I_1 and I_2 we segment the nucleoid(s) using the same edge detection algorithm described in the Quantitative Image Analysis of Chapter 2. If the nucleoids from daughters are sufficiently separated, the algorithm can distinguish each of the two separate nucleoids. In this case I_1 and I_2 can be directly determined using binary image masks created for each nucleoid by summing all intensities in the masked area after background subtraction. However, the program is not able to distinguish individual nucleoids in the early stages of cell division. In this case, we use the position of the Z-ring to divide the image mask of the mother cell nucleoid into two regions, which correspond to two daughters. If the Z-ring is not present (because the signal is too weak or the Z-ring has already dissociated) then we use the minimum in the nucleoid density distribution to divide the image mask. To find the position of the Z-ring, we fit the line profile of ZipA-GFP along the long axes of the cell to a Gaussian. Similarly, to find the minimum in the nucleoid density distribution we fit line profiles of HupA-mCherry to a Gaussian minimum. The maximum in ZipA-GFP intensity and minimum in HupA-mCherry intensity typically localize within a single pixel (107 nm). A perpendicular line crossing the longitudinal centerline of the cell at the position of the ZipA-GFP maximum (or HupA-mCherry minimum) then divides the

mask image to two regions from which intensities I_1 and I_2 are determined. Alternatively, instead of manipulating image masks, line profiles such as shown in Fig. 3*C* can be directly used to divide the cell into two regions and to find I_1 and I_2. This analysis yields very similar values to those described above but is less convenient to use once the cells have divided and moved away from each other.

Because of diffraction broadening, intensity from the larger sister nucleoid (I_2) extends into the region containing the translocating nucleoid (I_1), and vice versa. Our modelling shows that typically the intensities that extends from the smaller daughter to the larger daughter is approximately equal to the intensity that extends from the larger daughter to the smaller. However, in cases of very asymmetrically positioned division planes, the fluorescence from the larger daughter can contribute to I_1 more than the fluorescence from the smaller daughter contributes to I_2, therefore introducing error into the analysis. Moreover, the cell of interest usually grows within a colony where the position and fluorescence intensities of neighboring cells change. Fluorescence from the neighboring cells that reaches the cell of interest due to diffraction also introduces measurement errors. These errors can be largely circumvented by deconvolving the original HupA-mCherry image with the point spread function (PSF) of the microscope. To deconvolute the image, we experimentally determined the width of the microscope's PSF and then used this width to customize the PSF used in Matlab's deconvblind function. The final width from the deconvblind function which results from 10 iterations generally matches the original width to within about 25%. In situations where the two daughter nucleoids are well-separated from each other and from other cells, the analysis with and without deconvolution yield essentially identical results.

Total amount of DNA translocated during septum closure

From the experimentally determined I_1 and I_2 values, we determine the fraction of the chromosome, f, that resides in the compartment of the smaller daughter. The fraction as a function of time is defined as:

$$f(t) = \frac{I_1(t)}{I_1(t) + I_2(t)}$$

The fraction does not change when the cell grows conformally, i.e., the nucleoid length and the cell length increase in time proportionally to their original length. For conformally growing cells, any change in f results from translocation. In Fig. 3*F* we normalize this fraction by the fraction that is present at the end of division f_{final} and average it over the cell population $< f(t)/f_{final} >$. The normalized fraction curve allows us to determine what fraction of the chromosomal mass was translocated across the septum relative to the final amount of chromosomal mass in the smaller daughter immediately after cell division. This translocated fraction is equivalent to the total change in the normalized translocation curve of Fig. 3*F* (the difference in the final fraction and the initial fraction value). It is easier to see the validity of this statement when the change in overall fluorescence intensity of the HupA-mCherry nucleoid label and any DNA replication during the translocation process can be neglected. In this case, the translocated amount of nucleoid as function of time is proportional to intensity, I_{trans}, which is given as:

$$I_{trans(t)} = I_1(t) - I_{1,initial}$$

Where $I_{1,i}$ is intensity of the HupA-mCherry signal in the smaller daughter's compartment at the beginning of the translocation. The total intensity from the translocated portion of the chromosome is:

$$I_{trans,total} = I_{1,final} - I_{1,initial}$$

where $I_{1,final}$ is the intensity of the HupA-mCherry signal in the smaller daughter's compartment right after division. The latter can be written using the fraction f_{final} as:

$$I_{trans,total} = f_{final} \cdot I_{tot,final} - f_{initial} \cdot I_{tot,initial}$$

where $I_{tot} = I_1 + I_2$. Instead of using the intensity $I_{trans,total}$,which depends on imaging conditions, of more interest is the value $I_{trans,total}$ normalized by the intensity of HupA-mCherry at the end of translocation ($I_{trans,total}/I_{1,final}$). The normalized intensity corresponds to the fraction of the chromosome translocated during the division process. Assuming $I_{tot,initial} = I_{tot,final}$ and making use of the definition of f yields:

$$I_{trans,total}/I_{1,final} = 1 - f_{initial}/f_{final}$$

The right hand side of this equation is the difference between the start and end points of the normalized translocation curve plotted in Fig. 3*F*. Importantly, the same formula still applies even if the amounts of both HupA-mCherry and chromosomal DNA change during the translocation period. In this case, the translocated chromosomal amount, I_{trans}, is given by:

$$I_{trans}(t) = I_1(t) - I_{1,initial} \cdot G(t)$$

Here, the term $G(t)$ accounts for any changes in the amount of fluorescent HupA-mCherry present within the cell as a function of time. $G(t)$ can be directly measured as the increase in total fluorescence intensity from the cell from the beginning of the translocation $G(t) = I_{tot}(t)/I_{tot,initial}$.

The intensity I_1 in the smaller daughter's side can be written in terms of this fraction as:

$$I_1(t) = f(t) \cdot I_{tot}(t) = f(t) \cdot G(t) \cdot I_{tot,initial} = \frac{f(t)}{f_{initial}} \cdot G(t) \cdot I_{1,initial}$$

Substituting this equation into the formula for the intensity of the translocated chromosome gives:

$$I_{trans}(t) = I_{1,initial} \cdot G(t) \cdot \left(\frac{f(t)}{f_{initial}} - 1\right)$$

The normalized translocation intensity is therefore given by:

$$\frac{I_{trans}(t)}{I_{1,final}} = \frac{I_{1,initial}}{I_{1,final}} \cdot G(t) \cdot \left(\frac{f(t)}{f_{initial}} - 1\right)$$

The final intensity right after translocation in the smaller daughter compartment is:

$$I_{1,final} = I_1(t_{final}) = \frac{f_{final}}{f_{initial}} \cdot G(t_{final}) \cdot I_{1,initial}$$

Substituting this expression into the normalized translocation intensity gives:

$$\frac{I_{trans}(t)}{I_{1,final}} = \frac{f_{final}}{f_{initial}} \cdot \frac{G(t)}{G(t_{final})} \cdot \left(\frac{f(t)}{f_{initial}} - 1\right) = \frac{G(t)}{G(t_{final})} \cdot \left(\frac{f(t) - f_{initial}}{f_{final}}\right)$$

The total amount of chromosome translocated in units of the final amount within the smaller daughter's compartment is:

$$\frac{I_{trans,total}}{I_{1,final}} = \frac{G(t_{final})}{G(t_{final})} \cdot \left(\frac{f_{final} - f_{initial}}{f_{final}}\right) = \left(1 - \frac{f_{initial}}{f_{final}}\right)$$

As can be seen, the change in fluorescence intensity of HupA-mCherry cancels from the total translocated fraction and consequently the result is the same when a constant intensity was assumed. Again, the right hand side of the last equation can be found as the difference between the start and end points of the normalized translocation curve plotted in Figure 33G.

P1 transduction procedure for M9-grown cells

As part of this work, we contribute a P1 transduction procedure for cells that must be grown in nutrient poor M9 minimal medium, such as our double mutant Δ*slmA*, Δ*min* strains. The standard P1 transduction procedure can be used for cells that are grown in nutrient rich LB medium but not for M9 medium, since the CaCl used to activate the P1 phage precipitates with the phosphates in the M9 salts before the phage can activate. We found that a brief transfer of the cells to LB medium, just for a sufficient amount of time for the P1 phage to activate and infect its host did not lead to lysis of the M9-dependent strain. Once the bacteria had been transduced, they were promptly placed back in M9-medium where they could proliferate. Our procedure steps are as follows:

1. Grow an overnight of the recipient M9 strain.
2. Transfer pellet from the overnight M9 culture to equal amount of LB medium
3. Add 200uL of LB-transferred cells to four microfuge tubes.
4. Add 2uL of 1M $CaCl_2$ to each tube.
5. Add 50uL LB to one tube (= negative control). Add 1, 10, and 50uL P1 lysate to one of the remaining tubes (optimal volume may vary).
6. Incubate at 37C for 30 minutes (no shaking).
7. Add 100uL 1M Na-citrate (prevents superinfection) and 500 uL LB to each of the four tubes.
8. Incubate ~45 minutes (for transducing dominant antibiotic resistance).
9. Pellet cells: 8000RPM for 2 minutes.
10. Resuspend in 100uL M9 + 5mM citrate.
11. Plate on selective M9 medium. Additional negative control: plate P1 lysate alone.

Glossary

1. Anucleate – Refers to a cell that upon division fails to inherit a chromosome. A minicell is said to be anucleate.
2. Bi-lobed – As nucleoids segregate, the replicated portions begin to separate from each other into two lobes. The unreplicated region connects these two lobes. The resulting chromosomal distribution is said to be bi-lobed.
3. Cephalexin – An antibiotic that inhibits septal cell wall synthesis (FtsI). Cells treated with Cephalexin fail to divide but grow very long (50μm or longer).
4. Constriction – Cell constriction and inward septum closure refer to the same process, characterized by visible invagination of the cell envelope in microscope images. The septum and constriction can be used synonymously.
5. Cytokinesis – the same as Septation, is the event when one cell completes division into two daughter cells.
6. Dif site – The dif site is a 28 bp stretch of DNA located approximately at the center of the Ter macrodomain that is involved in separating chromosomes that occasionally link together during replication (called “dimerized” chromosomes.
7. Division Plane – The location of cell division, called the division plane, is established by where the divisome forms.
8. Divisome – Once the Z-ring has formed, the addition of the remaining 30 or so proteins to the Z-ring that allow the formation of the lateral cell wall, compose the macrostructure known as the divisome. A “mature” Z-ring is equivalent to the divisome.
9. DNA Translocation – The process of moving DNA material within the cell. In many bacteria, DNA is known to translocate via the DNA pump FtsK. It appears that another form of FtsK-independent translocation is coupled to cell constriction (septal cell wall synthesis).

10. Fluorescent Fusion Protein – Refers to the process of connecting two proteins, one which is under investigation, and another which fluoresces when exposed to incident light of a specific wavelength. Fluorescence is measured with a fluorescence microscope. We synonymously refer to fluorescent fusion proteins as “labeled proteins”. In this context, the fluorescent portion of the protein fusion is the label.
11. FtsK – A protein that localizes late to the divisome and helps coordinate late stages of cell division and chromosome segregation. FtsK is a DNA translocase that is known to affect approximately 400 kbp of terminus DNA, and plays an important role in resolving chromosome “dimers” (two complete chromosomes in one large circular piece).
12. FtsK-K997A – By mutating one amino acid, a lysine 997 to an alanine, FtsK can no longer bind ATP. Without the ability to bind ATP, FtsK cannot pump DNA. The FtsK-K997A mutation, therefore removes FtsK translocase activity.
13. FtsZ – a highly conserved, self-polymerizing protein that forms the macroscopic structure called the Z-ring that serves as a scaffold for approximately 30 additional proteins that are involved in building the lateral cell wall during cell division.
14. Gel Electrophoresis – a technique used to determine to length of a sequence of DNA, usually following PCR. Since DNA is charged, it moves when placed in a sufficiently strong electric field. By placing the DNA in small wells created in an agarose gel, the DNA migrates through the electric field without spreading in a single lane (the gel is said to be anticonvective). Ethidium Bromide is added to the gel, which binds to DNA and fluoresces under UV exposure. The migration of DNA sequences can be compared to the migration of DNA of known length (which is simultaneously ran through the gel in a different well, or lane).
15. Genome – typically used when speaking of a complete chromosome, where complete implies the chromosome has all the genes from the mother cell.

16. HupA – A protein that uniformly binds DNA and is capable of wrapping and stabilizing DNA like Histone in eukaryotic cells. For live cell imaging, we label HupA with a red fluorescent protein called mCherry.
17. Homologous Recombination – The process whereby nucleotide sequences are exchanged between two similar or identical sequences of DNA.
18. Immunofluorescence microscopy - A technique that uses special antibodies coupled to fluorescent dyes, which when conjugated to their target antigen allows visualization of the antibody distribution. In this technique, the distribution of the antibody-bound antigen forms the subcellular structure of interest. As an example, in *E. coli*, the antigen could be FtsZ.
19. *in vitro* – An experiment or process performed outside the living organism in a test tube, petri dish, etc.
20. *in vivo* – An experiment of process performed inside the living organism (which usually produces the most physiologically relevant results).
21. Kymograph – A plot that represents spatial position on the y-axis over time (the x-axis). In the kymographs presented here, the spatial axis represents fluorescence intensities along the long axis of a particular *E. coli* cell. Accordingly, we represent higher and lower intensities as a heat map. Higher intensities are red, lower intensities are blue. Black represents regions of no fluorescence intensity, and/or regions outside the cell.
22. Macrodomain - The *E. coli* chromosome is thought to be composed of six distinguishable regions. Four of the six regions are thought to be structured, and are referred to as macro-domains (Ori, Left, Right, and Ter) along two additional non-structured (NS) regions (NS-left and NS-right). Organization of the chromosome into these macrodomains is believed to impose restrictions on the permitted rearrangements to the linear-order sequence of the chromosome.

23. MatP – DNA binding protein that binds to 23 specific DNA sequences called *matS* sites that helps organize terminus DNA by binding with other DNA-bound MatP proteins and therefore forms bridges between *matS* sites.
24. Min System – An oscillatory system composed of proteins MinC, MinD, and MinE that prevent Z-ring formation at cell poles.
25. Minicell – Refers to a division event when the division plane is very asymmetrically placed so that one daughter is much smaller than the other, and the smaller daughter lacks a chromosome.
26. Nucleoid – The chromosome is referred to as a nucleoid when we are speaking in terms of the chromosomes physiological state. In bacteria, the chromosome is compacted by osmotic pressure from cytosolic proteins, supercoiling, and DNA binding proteins.
27. Nucleoid/chromosome Segregation – As cells grow, the chromosome must be replicated to pass on heredity to all daughter cells. Segregation refers to the process of separating the circular chromosome which is undergoing replication.
28. Nucleoid Occlusion – Describes a phenomenological observation that Z-rings tend to form away from nucleoids as opposed to overtop them.
29. Plasmid – Many bacteria, in addition to their chromosomal DNA, plasmid DNA. A plasmid is a small DNA molecule within the cell (much smaller than the chromosome), which can independently replicate. Plasmids contain genes which can be expressed in the same way as chromosomal DNA.
30. Polymerase Chain Reaction (PCR) – a molecular biology technique used to exponentially amplify a segment of linear or circular DNA, to create thousands or millions of identical DNA sequences. In our application, we wish to amplify a gene contained in either a plasmid or chromosomal DNA (called the template DNA). To amplify exclusively the gene of interest, short DNA sequences (~30bp) called primers are synthesized to contain a complementary sequence to each end of the target gene. The template DNA

and primers are combined in specific reaction buffer which also contains a DNA polymerase (an enzyme that synthesizes new DNA). The reaction mixtures in then heated until the DNA melts (double stranded DNA becomes single stranded DNA). The temperature is lowered until the primers can anneal to their complementary regions of the now single stranded DNA. The temperature is then lowered further until the DNA polymerase can bind to short double stranded segments and begin synthesizing new double stranded DNA. This heating and cooling cycle is performed between 30 – 34 times. The result is the amplification of the DNA sequence of interest 2^N times (N is the number of heating and cooling cycles).

31. Replication Terminus Macrodomain – Approximately diametric to the Ori macrodomain, the replication terminus region, known as the Ter, is the last region of the chromosome to undergo replication and makes up about 20% of the total chromosome.
32. Septation – the same as cytokinesis, is the event when one cell completes division into two daughter cells.
33. Septum – Once the division plane has been established, and the cell begins to divide. The inward growth, or invagination, is referred to as the Septum.
34. SlmA – A protein that binds to specific DNA sequences called *slmA* binding sites distributed throughout the chromosome except in the replication terminus region. SlmA prevents Z-rings from forming over nucleoids.
35. PALM/iPALM super resolution microscopy - PALM (2D) and iPALM (3D) is a form of microscopy that depends on image reconstruction of sparsely activated fluorescent molecules (either dyes or fluorescent fusion proteins/antibodies). Each fluorophore can be resolved only to the Abbe diffraction limit, however if each fluorophore is properly fitted, its centroid coordinate can be recorded. If properly stimulated, only a fraction of the fluorophores are excited, and in time either photo-bleach or reenter an “off” state. Repeating imaging acquisition for many cycles allows the centroids of a large number of

point emitting fluorophores to be recorded and a representation of the entire image can be subsequently reconstructed. Typical resolution of this technique is 10nm, but ultimately depends on the number of fluorophores recorded during acquisition.

36. Ter-linkage – A mechanism that promotes Z-ring positioning near the replication terminus DNA by way of a protein linkage involving ZapA, ZapB, and MatP proteins, though more proteins may be involved in the linkage than have been found at this point.
37. Transertion – A hypothetical process where concurrent DNA transcription and membrane protein translation and insertion leads to membrane crowding in the region where the membrane protein is being inserted.
38. Vegetative growth – The form of bacterial growth associated with favorable nutrients and environmental conditions, i.e., active growth and division. When favorable conditions are not met, many bacteria halt vegetative growth and enter a quiescent phase.
39. Wild-type – referring to a strain of bacteria that contains no gene deletions from its genome. Wild-type strains still can possess protein labels, however.
40. ZapA – A non-essential protein that localizes early to the Z-ring and is thought to help stabilize FtsZ filaments. ZapA is also a necessary part of the Ter linkage.
41. ZapB - A non-essential protein that also localizes early to the Z-ring and like ZapA is thought to help stabilize FtsZ filaments. ZapB is known to bind to itself and form an extended ring-like structure that sits inside the Z-ring. ZapB is a necessary part of the Ter linkage.
42. ZipA – an essential cell division protein that binds FtsZ monomers and filaments and serves as a cytoplasmic membrane anchor for the Z ring. We often use ZipA-GFP as a label for the Z-ring instead of FtsZ.
43. Z-ring – Once FtsZ polymerizes into longer filaments, the bundling of these filaments into a loose annulus-like structure at mid-cell is called the Z-ring. Te Z-ring is the scaffold for at least 30 other proteins, that once bind (either directly or indirectly) compose the

divisome. As mentioned already, the divisome is capable of carrying out cell division. The Z-ring, by itself, is not capable of carrying out cell division.

Vita

Matthew Wayne Bailey was born in Wise Virginia to Fredia and Wayne Bailey of southeastern Kentucky. Karen is his older sister, and Tekoa, Taylor, and Jackson are his wonderful nieces and nephew. His family has lived in the small town of Isom Kentucky as long as Matthew has been alive. He attended elementary school at Beckham Bates, and high school at Whitesburg High, graduating in 2005. He attended Berea College, in Berea Kentucky, where he graduated with a Bachelor's of Arts in Physics in 2009. While at Berea, he was involved in a Research Experience for Undergraduates at the University of Wisconsin, Madison where he studied stellar evolution in open clusters with Professor Bob Mathieu. Matthew also dabbled in a research project with his colleague Mohammed Yusuf at Berea College, which was led by Professor Amer Lahamer in the Mossbauer Spectroscopy of iron fortified breakfast cereals. After graduating, Matthew began graduate school at the University of Tennessee and joined Professor Jaan Mannik's Laboratory of Cellular Biophysics in the fall of 2011. There, he studied how nanometer-scale proteins localized so precisely within micron-scale *Escherichia coli*. Matthew has many interests, and would like to pursue a career where his broad scientific background can be used to serve others, whether by science education, science policy, medical or health physics, or disease related research.